UNIVERSITY OF ADELAIDE LIBRARY 19/3/07

A Wavelet Approach to Doppler-Robust Broadband Communication System Design

by

Limin Yu

B.Eng, M.Sc

Thesis submitted for the degree of

Doctor of Philosophy

in

School of Electrical and Electronic Engineering,
Faculty of Engineering,
Computer and Mathematical Sciences

University of Adelaide, Australia

2007

© Copyright 2007
Limin Yu
All Rights Reserved

Typeset in LaTeX 2_ε
Limin Yu

Contents

Statement of Originality

I declare that this thesis contains no material that has been accepted for the award of any other degree or diploma in any university or other tertiary institution and, to the best of my knowledge and belief, contains no material previously published or written by another person, except where due reference has been made in the text.

I give consent to this copy of the thesis, when deposited in the University Library, being available for loan and photocopying.

Signed ✓ Date 01/03/07

This page is blank

Acknowledgements

First and foremost, I AM DEEPLY INDEBTED to my supervisor Professor Lang White for his guidance, support and encouragement all the way through my PhD studies. His extensive knowledge in communications engineering and excellence in mathematics have been of great help in solving many technical problems I confronted. The work in this thesis would not have been carried out without his profound insight and advice at every stage of my thesis research.

I am sincerely grateful to my co-supervisor Assoc Professor Bruce Davis for sharing his wisdom in research and his kind advice on my technical writing and English grammar. It has been a great pleasure to talk with him over many aspects of the research work and family life.

I would like to thank Professor Lang White, Mr Stephen Guest, Assoc Professor Michael Liebelt, and the ACoRN organisation for the award of travel funds for my attendance at many conferences and training courses which have been an informative experience with timely impact on the ongoing research at that moment.

Special thanks go to my thesis examiners for their kindest encouragement and valuable comments, and great thanks to Mr Stephen Guest, Mr David Bowler, Mr Mark Innes, Mrs Rose-Marie Descalzi, Mrs Yadi Parrot, Mrs Colleen Greenwood, Dr Matthew Sorell, and Dr Sanjeevan Naguleswaran for their kind help during my PhD study.

I truly appreciate the warmest friendship of my friends and colleagues at the Centre for Internet Research, Dr Belinda Chiera, Mr Vo Dat, Ms Sarah Hickmott, Ms Angela Wong, Ms Siew-Lee Hew, Mr Ching-yong Chang, Ms Lakshmi Veerapandian, and Ms Melissa Liew. The time with them has always been pleasant and heart-warming.

Last but not least, I would like to thank my dearest parents and my beloved husband Fei Ma for their unconditional caring and support. Their precious love is the source of all the achievements I have ever reached. THIS THESIS IS DEDICATED TO THEM.

Limin Yu

Centre for Internet Research (CIR)
School of Electrical and Electronic Engineering
The University of Adelaide
SA 5005, Australia
Email: liminyu@eleceng.adelaide.edu.au

Abstract

This thesis addresses Doppler-robust broadband system design using a wavelet approach. Doppler dispersion arising from the relative motion of transceivers reduces the reliability of communication links and complicates receiver design, especially in a broadband wireless communications system. In this thesis, two extremely different methods - herein termed 'high-Doppler' and 'medium-Doppler' methods - are exploited to cope with the Doppler dispersion. The high-Doppler method is developed for systems with extremely significant Doppler, e.g. in underwater acoustic (UWA) communications. The proposed method aims to resolve the coexisting multiple Doppler scales, and takes advantage of the multipath and Doppler scaling as another dimension of diversity rather than an impediment to be eliminated. The medium-Doppler method deals with Doppler dispersions smaller than those in the high-Doppler method, but still sufficiently significant to impair the effectiveness of the conventional Doppler compensation methods. This scale of Doppler can be found in many systems of radio vehicular communications. The proposed medium-Doppler method targets at improving the inherent robustness of the signal format rather than any forms of Doppler estimation and compensation techniques. More specifically, the method is developed in the context of orthogonal frequency division multiplexing (OFDM)-based broadband wireless communications.

The above two methods addressing the Doppler are made possible by the development of a new family of wavelets, the complex rational orthogonal wavelets (CROWs), based on the rational multiresolution analysis (MRA) framework. Theorems for the construction of the CROWs and a detailed study of their properties are presented in the first part of the thesis. The good time-frequency localisation and orthogonality of the CROWs form the basis of a CROW-based OFDM scheme presented in the second part of the thesis.

The high- and medium-Doppler methods are then detailed in two applications of the CROWs - the application to UWA communications and the application to radio vehicular communications with OFDM-based mobile wireless local area network (WLAN) as a special case. In addition to the above two applications coping with the Doppler dispersion, another direct application of the proposed CROWs in broadband wireless communications is the design of ultra-wideband (UWB) pulses using wavelet basis of the CROWs. These three applications organised into three chapters of the thesis cover the characterisation of CROW's application in single carrier modulation with the first two applications and in multicarrier modulation with the third application.

Publications

The following papers have been written based on the materials presented in this thesis.

Book Chapter

1. Limin Yu and Langford B. White, "Part 3: Processing of Source Information - A new complex wavelet and its application in communications", In T. A. Wysocki, B. Honary, and B. J. Wysocki (Eds.), *Signal Processing and Networking for Future Multimedia Communications*, Springer, 2006

Journal Papers

1. Limin Yu and Langford B. White, "Complex rational orthogonal wavelet and its application in communications", *IEEE Signal Processing Letters*, vol. 13, No. 8, pp. 477-480, August 2006.

2. Limin Yu and Langford B. White, "Optimum receiver design for broadband Doppler compensation in multipath/Doppler channels with rational orthogonal wavelet signalling", *IEEE Transaction on Signal Processing*, accepted for publication.

3. Limin Yu and Langford B. White, "A Doppler-robust OFDM scheme for high mobility WLAN", *Submitted to Elsevier Journal of Digital Signal Processing.*

Conference Papers

1. Limin Yu and Langford B. White, "Broadband Doppler compensation for rational wavelet-based UWA communication systems", *Proc. Asia-Pacific Conferences on Communications (APCC'05)*, pp. 605-609, 2005.

2. Limin Yu and Langford B. White, "A new complex wavelet and its application in communications ", *Proc. 4th Workshop on the Internet, Telecommunications and Signal Processing (WITSP'2005)*, 2005.

3. Limin Yu and Langford B. White, "Design of complex wavelet pulses enabling PSK modulation for UWB impulse radio communications", *Proc. 1st IEEE International Conference on Wireless Broadband and Ultra Wideband Communications (AuS Wireless'2006)*, 2006.

4. Limin Yu and Langford B. White, "A new OFDM scheme based on complex rational orthogonal wavelets", *Proc. Defense Applications of Signal Processing Workshop (DASP'2006)*, 2006.

Journal Papers in Preparation

1. Limin Yu and Langford B. White, "Rational orthogonal wavelet-based broadband communications in practical multipath/Doppler channels", *Journal Paper in Preparation.*

2. Limin Yu and Langford B. White, "Design of Wavelet Based Orthogonal Pulse Sets for UWB communications", *Journal Paper in Preparation.*

Acronyms

4G The Fourth Generation

AWGN Additive White Gaussian Noise

BER Bit Error Rate

BPSK Binary Phase Shift Keying

CDMA Code Division Multiple Access

CIR Channel Impulse Response

CP Cyclic Prefix

CQF Conjugate Quadrature Filter

CROW Complex Rational Orthogonal Wavelet

CROW-OFDM CROW based OFDM

CWT Continuous Wavelet Transform

DC Direct Current

DFT Discrete Fourier Transform

DFT-OFDM DFT based OFDM

DS Direct Sequence

DSP Digital Signal Processor

DTWT Discrete Time Wavelet Transform

DWT Discrete Wavelet Transform

FB Filter Bank

FCC Federal Communications Commission

FFT Fast Fourier Transform

FIR Finite Impulse Response

FT Fourier Transform

FWT Fast Wavelet Transform

GI Guard Interval

ICI Inter-carrier Interference

IDFT Inverse Discrete Fourier Transform

IDWT Inverse Discrete Wavelet Transform

IFFT Inverse Fast Fourier Transform

IR Impulse Radio

ISI Inter-symbol Interference

MB Multi-band

MB-CROW-OFDM Multiband Complex Rational Orthogonal Wavelet Based Orthogonal Frequency Division Multiplexing

MB-UWB-OFDM Multiband Ultra Wideband Orthogonal Frequency Division Multiplexing

MC Multicarrier

MCM Multicarrier Modulation

ML Maximum Likelihood

MRA Multiresolution Analysis

MWPM Multi-wavelet Packet Modulation

NOL Non-overlapped

OFDM Orthogonal Frequency Division Multiplexing

OFDMA Orthogonal Frequency Division Multiple Access

OL Overlapped

OOK On Off Keying

PAM Pulse Amplitude Modulation

PLL Phase-locked Loop

PPM Pulse Position Modulation

PR Perfect Reconstruction

PSD Power Spectrum Density

PSK Phase Shift Keying

PTS Partial Transmit Sequence

QAM Quadrature Ampultude Modulation

QPSK Quadrature Phase Shift Keying

ROW Rational Orthogonal Wavelet

RROW Real Rational Orthogonal Wavelet

SI Shift-Invariance

SLM Selected Mapping

SNR Signal to Noise Ratio

TF Time-Frequency

TH Time-Hopping

UWA Underwater Acoustic

UWB Ultra Wideband

WLAN Wireless Local Area Network

WPDM Wavelet Packet Division Multiplexing

List of Figures

List of Tables

This page is blank

Chapter 1

Introduction

1.1 Motivation and Background

1.1.1 Doppler Effect in Broadband Communications

Doppler dispersion arising from the relative motion of transceivers plays a significant role in many communication systems. In the narrowband case where the carrier frequency is much greater than the transmission bandwidth, the received signal is only a frequency-translated version of the transmitted signal. Doppler estimation can then be simplified to the estimation of the Doppler frequency offset. For a broadband signal, constituent frequency components suffer from random phase and magnitude distortion. The received signal exhibits multirate temporal scaling rather than frequency translation only. Frequency translation and slope mismatch thus jointly contribute to severe degradation of the correlation performance in the receiver.

Combined with multipath channel geometry, the Doppler effect leads to the important characteristics of a multipath/Doppler channel as mentioned in [64]: for narrowband signal propagation, a multipath/Doppler channel exhibits 1) rapid changes in signal strength in a small interval, 2) random frequency modulation due to varying Doppler shifts on different multipath signals, and 3) time dispersion caused by multipath propagation delay (frequency-selective fading). In contrast, in the broadband case, the received signal will be distorted but the signal strength does not change rapidly in time. Moreover, the Doppler causes time scaling of the signal rather than a frequency shift as in the narrowband case.

The multipath/Doppler channel therefore exhibits random scaling due to varying Doppler scales on different multipath signals. Examples of the multipath/Doppler channel include the underwater acoustic (UWA) channel with mobile transceiver platforms and radio vehicular communications. In general, the frequency dependent Doppler factor defined as the Doppler shift to carrier frequency ratio [40] is on the order of 10^{-7} or less for cellular vehicular communications [40], but could reach the order of 10^{-2} for vehicular UWA communications [70].

In the context of UWA communications, many broadband Doppler compensation methods have been developed under a similar structure of time-scaling estimation followed by multirate resampling [93],[63],[17],[70],[42]. In these cases, Doppler estimation is obtained by transmitting a wideband probe at the start of the data packet. A Doppler pre-processor at the receiver estimates the delay and scale by calculating the ambiguity function of the known probe signal. The residual Doppler is then processed by a subsequent equalizer embedded with a phase-locked loop (PLL). However, for a multipath/Doppler channel, since multiple scales co-exist on different multipath signals, the scale estimation followed by resampling structure will inevitably suffer from the residual Doppler because an average Doppler scale estimation has to be made before the resampling process.

In radio communications, a dominant broadband technology is the orthogonal frequency division multiplexing (OFDM) and its varieties such as coded OFDM (COFDM), orthogonal frequency division multiple access (OFDMA) and multicarrier code division multiple access (MC-CDMA). Attractive features of an OFDM transmission system include fast modulation/demodulation algorithms based on fast Fourier transform (FFT), high spectral efficiency and the robustness over a multipath fading channel. However, it is well known that a pure OFDM scheme is very sensitive to Doppler which impairs the orthogonality of OFDM subcarriers and causes intercarrier interference (ICI). In comparison to a single frequency shift in the signal caused by the frequency offset between the local oscillators at the transmitter and receiver, the Doppler effect leads to a spread of frequency shifts of a wideband OFDM signal. As detailed in [69], various approaches to mitigate the frequency shifts proposed in the literature could be classified into two categories. One is based on the estimation and removal of the frequency offset [77], [54], [98]. The other is based on signal processing and/or coding techniques to reduce the sensitivity

of the OFDM system to the frequency offset, e.g., the wavelet-based OFDM [51], windowing/pulse shaping OFDM [59], polynomial coding based OFDM [100], correlative coding based OFDM [99] and forward error correction coding based OFDM [66].

In general, the approaches in the first category require high computational complexity because the correction procedure alone involves interpolation or multiplication of the received signal with an estimated sinusoidal signal [69]. The approaches in the second category have lower computational complexity than those in the first category and are more desirable for the mitigation of ICI caused by the Doppler dispersion. However, different approaches in the second category also vary in the computational complexity, the tolerance of ICI, and the degradation of spectrum efficiency, among which a tradeoff has to be made. With increased vehicle speed that causes more severe ICI, the existing ICI mitigation approaches become more computationally complex, less spectral-efficient or simply do not work.

As a strong candidate for broadband wireless communications, OFDM is adopted in many standards, e.g., IEEE 802.11 [5] and IEEE 802.16 [6] which are intended for stationary or low mobility users. To address high speed mobility, a draft of 802.20 specification [3] was balloted and approved on January 18th, 2006, and the IEEE 802.11p [4] is currently under development. The formal 802.11p standard is scheduled to be published in July 2008. As a key technique in high mobility OFDM based wireless standards, an OFDM scheme that could cope with high mobile velocities in radio vehicular communication environments is an active research topic and is considered a 4G technology [36], which requires further research effects.

1.1.2 Wavelet-based Signal Processing in Communications

As a versatile signal processing tool, the wavelet theory has found various applications in communications, including wavelet-based channel modelling [39], channel estimation [52], pulse design [61], signal detection [30], and wavelet-based multicarrier modulation (MCM) [44]. Among them, the wavelet-based MCM or wavelet-based OFDM, has drawn most of the attention and research effects. To distinguish the wavelet-based OFDM from the conventional OFDM, we classify the OFDM schemes into two categories according to the type of subcarrier pulse shaping filters: *the DFT-based OFDM* and *the wavelet-based OFDM*. A brief review of these two categories is as follows.

1) *The DFT-based OFDM*: The subcarriers are sinusoidal signals. The modulation and demodulation can be implemented by IDFT and DFT. The most traditional OFDM is the DFT-based OFDM with rectangular pulses. Cyclic prefix (CP) is added to suppress inter-symbol interference (ISI) which decreases the spectrum efficiency. The problem with this class of OFDM schemes is the large sidelobes of the subcarrier spectrum which may cause severe inter-carrier interference (ICI) because the frequency dispersion of the channel results in the loss of orthogonality among subcarriers. More efforts have been made to design smoother optimal shaping pulses with reduced sidelobes and improved orthogonality through frequency dispersive channels [78], [19].
2) *The Wavelet-based OFDM*: The subcarriers are the orthogonal wavelet bases of the wavelet subspaces. The modulation and demodulation can be implemented by inverse discrete wavelet transform (IDWT) and discrete wavelet transform (DWT). Due to better time-frequency localisation, the wavelet-based OFDM offers improved ISI cancellation without the need of CP, and better ICI mitigation performance in time-dispersive channels because of the reduced spectrum sidelobes.

A large variety of wavelet-based MCM schemes have been proposed such as fractal modulation [84], [12], dyadic wavelet-based OFDM [60], wavelet packet division multiplexing (WPDM) [51], [86], [97], [49], [31] and multi-wavelet packet modulation [88]. In these schemes, dyadic wavelets/wavelet packets are used because of the availability of fast transform algorithms based on the fundamental work of Mallat [55].

Wavelet-base pulse design also plays an important role in the wavelet-based communication applications. In particular, the wavelet-based ultra-wideband (UWB) pulse design has drawn more and more attention because of the potential of UWB technology in many wireless applications. A UWB impulse radio (IR) system features very short pulses of the order of nanoseconds as the transmission signal and operates at baseband without the involvement of carriers. Based on the Federal Communications Commission (FCC)'s regulation on the UWB spectrum from 3.1 to 10.6 GHz , a UWB pulse has to be carefully designed to conform to the FCC spectrum mask. Popular UWB pulses include the 2nd derivative of Gaussian, Rayleigh pulse and orthogonal Hermite pulses [7], [38]. Variant wavelet-based UWB pulses are also proposed in [8], [56], [61], [96], [25] based on B-spline wavelet, modulated Gaussian wavelet, Haar wavelet and wavelet packets.

With the development of the wavelet theory, numerous wavelets have been developed, to name a few, Daubechies wavelets [27], Symlet wavelets [27], Coiflet wavelets [27], Meyer wavelet [27], Morlet wavelet [27], complex Gaussian wavelets [2], complex Morlet wavelets [76] and complex frequency B-spline wavelets [76], each of which satisfies some but not all of the wavelet properties including the smoothness/order of zero moments, support in the time and frequency domains, symmetry, orthogonality/biorthogonality and the availability of a fast transform algorithm. It is worth noting that complex wavelets featuring both amplitude and phase information outperform real valued wavelets (featuring only the amplitude information) in many applications where local phase information of signals or images is needed. There are a number of ways to construct complex wavelets with variant properties. Complex Gaussian, complex Morlet and complex frequency B-spline wavelets are defined in the time domain with explicit expressions [76]. They are not orthogonal and compactly supported, therefore there are no discrete wavelet transforms (DWT) or FIR analysis/synthesis filters. Complex wavelets were also constructed by designing complex conjugate quadrature filters (CQFs) which lead to the associated complex wavelets [48]. Further efforts have been focused on the design of pairs of wavelet filters to achieve desired orthogonality and symmetry properties of complex wavelet transforms [46], [68], [75].

While the existing wavelets find more applications in communications, emerging communication techniques call for the construction of new wavelets with desired properties that suit specific communication applications, and further drive the development of wavelet theory.

1.2 Outline of the thesis

The thesis addresses Doppler-robust system design in broadband wireless communications using a wavelet approach. For different scales of Doppler dispersions, two different methods - herein termed 'high-Doppler' and 'medium-Doppler' methods - are exploited. The high-Doppler method is developed for systems with extremely significant Doppler, e.g. in UWA communications. The proposed method takes advantage of the multipath and Doppler scaling as another dimension of diversity rather than an impediment to be eliminated. The medium-Doppler method deals with Doppler dispersions smaller than

those in the high-Doppler method, but still significant to impair the effectiveness of the conventional Doppler compensation methods. This scale of Doppler can be found in many systems of radio vehicular communications. The proposed medium-Doppler method targets at improving the inherent robustness of the signal format rather than any forms of Doppler estimation and compensation techniques.

The above two methods addressing the Doppler are made possible by the development of a new family of wavelets, the complex rational orthogonal wavelets (CROWs), based on the rational multiresolution analysis (MRA) framework. Theorems for the construction of the CROWs and a detailed study of their properties are presented in chapter 2.

Given the fact that OFDM is a dominant technology in broadband wireless communications, the medium-Doppler method is developed in the context of OFDM-based broadband wireless communications. Utilising the wavelets proposed in chapter 2, the construction of a new OFDM scheme - the CROW-based OFDM is presented in chapter 3.

Three applications of the CROWs are then detailed in the following three chapters. Chapter 4 presents the high-Doppler method for UWA communications using wavelet pulse signalling in the transmitter. A transmultiplexer system model is presented to characterise the multiscale nature of the channel and the recovery of scale-compensated signal based on perfect reconstruction (PR) wavelet filter banks (FBs).

The medium-Doppler method is presented in the context of radio vehicular communications with OFDM-based mobile wireless local area network (WLAN) as a special case. The application of the CROWs in this broadband communication scenario is presented in chapter 6, where a multiband (MB) CROW-based OFDM scheme is proposed particularly for high mobility WLAN applications.

In addition to the two applications of CROWs to cope with the Doppler dispersion, another direct application of the proposed CROWs in broadband communications is the design of UWB pulses based on the wavelet basis of the CROWs. It is worth noting that due to the carrier-less nature of the UWB impulse radio (IR) communication, M-ary PSK modulation schemes are not yet considered for UWB single-band system because it is a modulation method that is closely related to the phase of sinusoidal carriers. Therefore, current UWB pulses are based on real signals. In chapter 5, we demonstrate that PSK

modulation is possible for UWB IR by introducing complex UWB pulses. Two design examples of complex UWB pulses are presented in chapter 5.

Considering that the applications of the CROWs in UWA and UWB communications have the same nature of single carrier modulation while the WLAN application involves multicarrier modulation, the application of CROWs to UWB IR is arranged as a chapter right after chapter 4. Therefore, the three applications cover the characterisation of CROW's application in single carrier modulation with the first two applications (chapter 4 and 5) and in multicarrier modulation with the third application (chapter 6).

The summary of main contributions of the thesis and the reflections on future work are presented in chapter 7.

This page is blank

Chapter 2

Real and Complex Rational Orthogonal Wavelets

2.1 Introduction

This chapter presents the wavelet theory that forms the basis of the work in subsequent chapters where the wavelet theory is applied to broadband communications. In this chapter, a generalised method is proposed to construct real rational orthogonal wavelets (RROWs) and complex rational orthogonal wavelets (CROWs) under the framework of rational multiresolution analysis, MRA(M), where M is a rational number. Based on the fundamental work on RROWs by Auscher [14] and Baussard in [16], we derive explicit formulae for a class of RROWs with rational dilation factor of $a = \frac{q+1}{q}$, which is a special case of more general definition of RROWs proposed in [16]. A new family of wavelets, the CROWs, is then constructed based on the rational MRA structure of the RROWs.

It has been pointed out that we can always take the Hilbert transform of one wavelet to form another wavelet [68]. We give a theoretical verification of this argument and prove that complex wavelets with nice properties can be derived based on the two related wavelets. Theorems and examples are given for the construction of CROWs with the rational orthogonal property and whose real and imaginary parts form an exact Hilbert transform pair. Since the classical Mallat's MRA is a special case of the rational MRA(M) with $M = 2$, these theorems also hold for the construction of complex dyadic wavelets. Based on two real rational MRA(a) or a complex rational MRA(a) with $a = \frac{q+1}{q}$, a new

class of CROWs is constructed. Besides the benefit it achieves by capturing the phase information which the real valued wavelets lack, it has the unique rational orthogonal property which is suited for specific application scenarios where binary orthogonality achieved by dyadic wavelets is not sufficient for the scale resolution.

The properties of RROWs and CROWs are investigated including the scale orthogonality, shift orthogonality, time-frequency localisation property and fast wavelet transform (FWT) algorithm. The connection of the FWT structure with the rational sampling filterbank (FB) design is also discussed.

The chapter is organised as follows. In section 2.2, theorems for the construction of the RROWs are presented. Examples of the constructed RROWs are given. Section 2.3 examines the time-frequency localisation property of RROWs. The theorems for the construction of the CROWs are presented in section 2.4. Section 2.5 presents the FWT algorithms for RROWs and CROWs. The connection of the FWT structure with the rational sampling FBs is discussed in section 2.6. The computational complexity of the FWT algorithm is examined in section 2.7. Section 2.8 presents the conclusions of this chapter.

2.2 Real Rational Orthogonal Wavelets (RROW)

Real rational orthogonal wavelets were derived under the framework of a rational MRA proposed by P. Auscher in [14], who proved that given any rational number $M > 1$, there exists a finite set, ψ_1, ψ_2, ..., ψ_ℓ, of functions in $L^2(\mathbb{R})$ such that the family $M^{j/2}\psi_n(M^j x - k)$, $j, k \in \mathbb{Z}$, $1 \leq n \leq \ell$, is an orthonormal basis for $L^2(\mathbb{R})$. An MRA with rational dilation factor M was defined by:

Definition 1: *An orthonormal MRA for $L^2(\mathbb{R})$ with dilation factor M (denoted by MRA(M)) consists of a collection V_j, $j \in \mathbb{Z}$, of subspaces such that*
i) $V_j \subset V_{j+1}$, $\forall j \in \mathbb{Z}$;
ii) $\bigcap_{j\in\mathbb{Z}} V_j = \{0\}$ and $\bigcup_{j\in\mathbb{Z}} V_j$ is dense in $L^2(\mathbb{R})$;
iii) $f(x) \in V_j$ if and only if $f(Mx) \in V_{j+1}$;
iv) there exists a function $\phi(x) \in V_0$ such that $\{\phi(x-k),\ k \in \mathbb{Z}\}$, forms an orthonormal basis for V_0.

Let W_j be the orthogonal complement of V_j in V_{j+1}. The following theorem for the wavelet basis related to an MRA(M) is borrowed from [14]:

Theorem 1: *With the Definition 1 and assuming $M = \frac{p}{q}$, p and q being relatively prime integers with $p > q > 1$, there exists a set of $p-q$ wavelet functions $\psi_1, \psi_2, \cdots, \psi_{p-q}$ in W_0 such that the collection of functions $(\frac{p}{q})^{\frac{j}{2}}\psi_n((\frac{p}{q})^j x - kq)$, $k, j \in \mathbb{Z}$, $1 \leq n \leq p-q$, forms an orthonormal wavelet basis for $L^2(\mathbb{R})$.*

It was further pointed out that the number of wavelets in W_0 does not depend on the choice of the ψ_i's and the choice of the ψ_i's is not unique. Associated examples of scaling/wavelet basis functions with analytic expressions in frequency domain were presented. By permitting more general types of roll-off in the transition bands of the frequency spectrum, this class of wavelets were generalised by Baussard in [16]. The definition of the RROWs was given as follows.

Let $\chi(\omega)$ be an even and $\mathcal{C}_\infty(\mathbb{R})$ function defined by

$$\chi(\omega) = \begin{cases} 0, & \omega \in [0, a] \\ \frac{\pi}{4} + \beta(\omega - q\pi), & \omega \in [a, b] \\ \frac{\pi}{2}, & \omega \in [b, Ma] \\ \frac{\pi}{4} - \beta(\frac{\omega}{M} - q\pi), & \omega \in [Ma, Mb] \\ 0, & \omega \in [Mb, +\infty), \end{cases} \tag{2.1}$$

where $M = p/q$, $p = q+1$, $a = (q-\varepsilon)\pi$, $b = (q+\varepsilon)\pi$, $\varepsilon \in [0, (1+M)^{-1}]$ and β being an odd and $\mathcal{C}_\infty(\mathbb{R})$ function such as

$$\forall \omega \in [\varepsilon\pi, +\infty], \ \beta(\omega) = \frac{\pi}{4}, \tag{2.2}$$

and ω is in radians. Then the scaling function $\phi(t)$ is defined as

$$\Phi(\omega) = \begin{cases} \cos(\chi(\omega)), & |\omega| \leq (q-\varepsilon)\pi \\ 0, & elsewhere \end{cases} \tag{2.3}$$

where $\Phi(\omega)$ is the Fourier transform (FT) of $\phi(t)$, defined as

$$\Phi(\omega) = \int_{-\infty}^{\infty} \phi(t) e^{-j\omega t} dt. \tag{2.4}$$

The wavelet $\psi(t)$ is also defined by its FT as

$$\Psi(\omega) = \mathrm{sgn}^{(q+1)}(\omega) \sin(\chi(\omega)) e^{-j\frac{\omega}{2}}, \tag{2.5}$$

where sgn(.) is the sign function defined by

$$\mathrm{sgn}(x) = \begin{cases} 1, & x > 0 \\ 0, & x = 0 \\ -1, & x < 0. \end{cases} \tag{2.6}$$

To construct $\chi(\omega)$ within the interval $[a, b]$ and $[Ma, Mb]$, a few construction functions were proposed in [16]:

$$y = \frac{1 + \cos(x)}{2}, \tag{2.7}$$

$$y = 3x^2 - 2x^3, \tag{2.8}$$

$$y = 10x^3 - 15x^4 + 6x^5, \tag{2.9}$$

$$y = 35x^4 - 84x^5 + 70x^6 - 20x^7, \tag{2.10}$$

which lead to different number of derivatives at end points (while $x = 0, 1$) and the corresponding fast decay property of the wavelet. A filter bank interpretation of Auscher's rational MRA and fast synthesis/analysis algorithms implemented in frequency domain were proposed in [16].

Note that the parameter ε controls the length of the constant passband ($[b, Ma]$) between two transition bands ($[a, b]$ and $[Ma, Mb]$). An illustration of the spectra of rational wavelets with $q = 2$ and with different ε values is shown in Fig. 2.1.

Similarly, this thesis is restricted to a study of the wavelet cases where $M = 1 + \frac{1}{q}$ and therefore a single $\psi(t)$ can be chosen with the desired regularity and decay properties. In the sequel, we will denote scaling factors of this form by a. We derive explicit formulae [90] for a special case of rational wavelets defined in (2.5) with rational dilation factors of $a = \frac{q+1}{q} = 1 + \frac{1}{q}$ and with the constraint that its spectrum has no constant passband between two transition bands ($\varepsilon = \frac{1}{1+a}$). The corresponding definition of the rational scaling function $\phi(t)$ in the frequency domain can be derived as

$$\Phi(\omega) = \begin{cases} (2\pi)^{-\frac{1}{2}}, & |\omega| \le \omega_1 \\ (2\pi)^{-\frac{1}{2}} \cos(\frac{\pi}{2}\beta(\frac{q}{\omega_1}|\omega| - q)), & \omega_1 \le |\omega| \le \omega_2 \\ 0, & |\omega| > \omega_2, \end{cases} \tag{2.11}$$

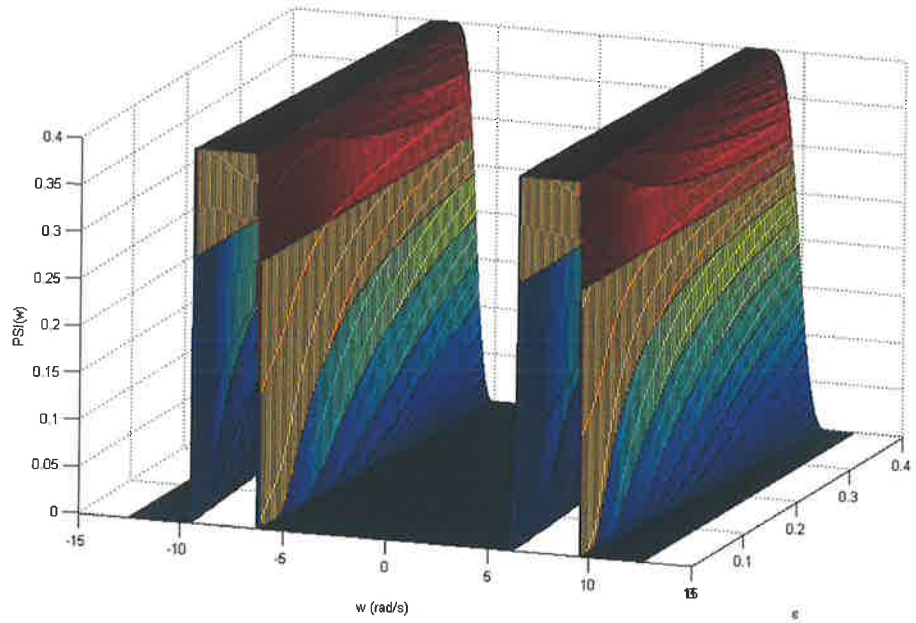

(a) Spectra of RROW with q = 2, and $\varepsilon = 0$ shown in the front

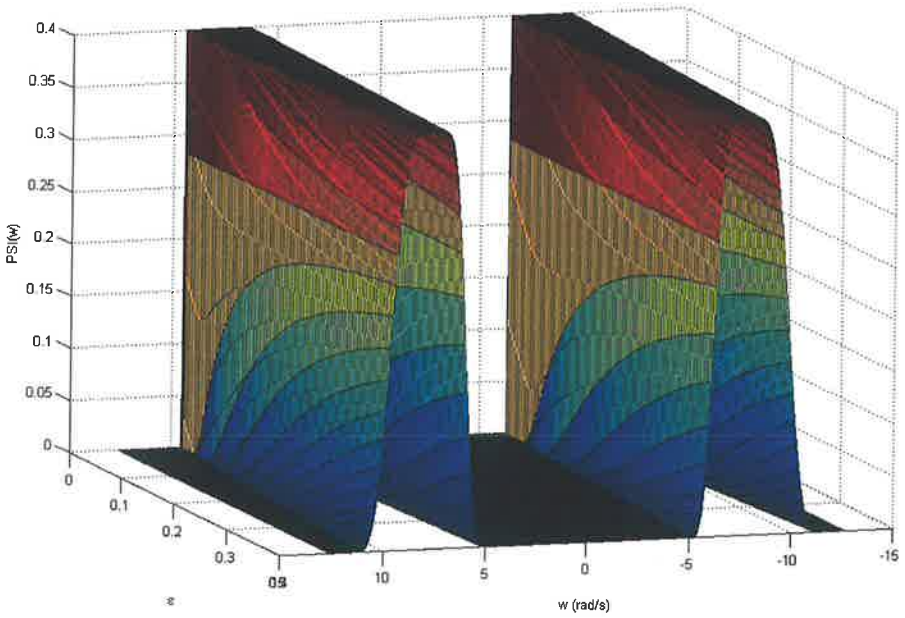

(b) Spectra of RROW with q = 2, and $\varepsilon = \frac{1}{1+a} = \frac{2}{5}$ shown in the front

Figure 2.1. Spectra of RROW with q = 2 and with different ε values

and the definition of the rational wavelet function $\psi(t)$ as

$$\Psi(\omega) = \begin{cases} (2\pi)^{-\frac{1}{2}} e^{j\frac{w}{2}} \sin(\frac{\pi}{2}\beta(\frac{q}{\omega_1}|\omega| - q)), & \omega_1 \leq |\omega| \leq \omega_2 \\ (2\pi)^{-\frac{1}{2}} e^{j\frac{w}{2}} \cos(\frac{\pi}{2}\beta(\frac{q}{\omega_2}|\omega| - q)), & \omega_2 \leq |\omega| \leq \omega_3 \\ 0, & |\omega| \notin [\omega_1, \omega_3], \end{cases} \tag{2.12}$$

where

$$\begin{aligned} \omega_1 &= (q - \frac{q}{2q+1})\pi \\ \omega_2 &= a\omega_1 \\ \omega_3 &= a\omega_2 = a^2\omega_1. \end{aligned} \tag{2.13}$$

The construction function $\beta(t)$ is selected to be the form of equation (2.10). The well-known Meyer wavelet is actually one typical case of this class of wavelets by letting $q = 1$ and thus $a = 2/1$.

Defining $\psi_{kn}(t) = a^{-k/2}\psi(a^k t - nq)$, where $k, n \in \mathbb{Z}$, $a = \frac{q+1}{q}$, $q \in \mathbb{Z}^+$, the wavelet basis function $\psi(t)$ has the orthogonality property that

$$\int \psi_{kn}(t)\psi_{lm}(t)dt = \delta_{k-l}\delta_{m-n}, \ k, l, m, n \in \mathbb{Z}, \tag{2.14}$$

where $\delta_n, n \in \mathbb{Z}$ is the Kronecker Delta function. The collection of functions $\{a^{k/2}\psi(a^k t - nq), \ k, n \in \mathbb{Z}\}$ forms an orthonormal basis for $L^2(\mathbb{R})$.

The waveforms of the defined wavelets with $q = 1, 2$, and 3, are shown in Fig. 2.2.

2.3 Time-Frequency Localisation Property of RROW

In this section, the time-frequency localisation property of the RROW is examined. A good time-frequency localisation of a wavelet is a desirable property in many applications, e.g., the multicarrier modulation using wavelet basis functions as the orthogonal subcarriers [35]. In a multicarrier modulation system, a good time-frequency localisation property will reduce the intersymbol interference (ISI) and intercarrier interference (ICI) caused by the loss of orthogonality between subcarriers in a time-frequency dispersive channel [35].

With the definition of the RROW wavelet in the frequency domain, its time-frequency dispersion product, $\Delta W \Delta T$, can be calculated analytically based on the definition of

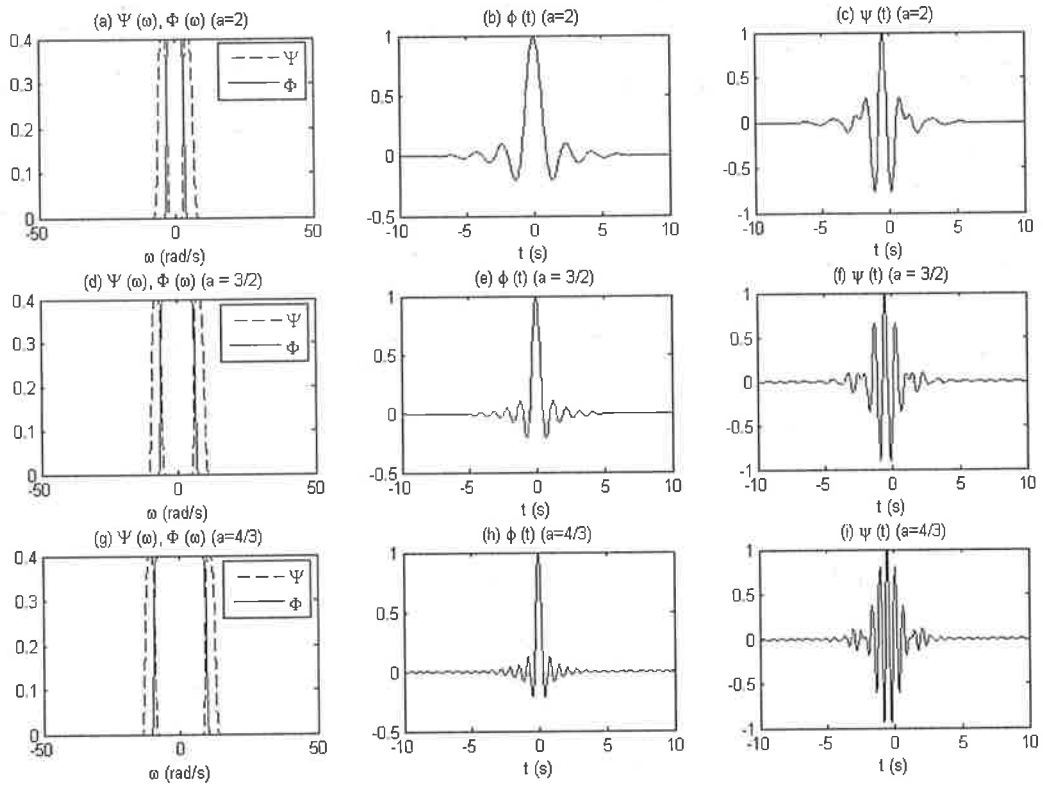

Figure 2.2. Real rational orthogonal wavelets with q = 1, 2 and 3.

$\Delta W \Delta T$ [35]. For a given waveform $g(t)$ centered around $(0, 0)$, the dispersion product of frequency dispersion ΔW and time dispersion ΔT are defined by

$$\begin{aligned} (\Delta T)^2 &= \int_{-\infty}^{\infty} t^2 |g(t)|^2 dt \\ (\Delta W)^2 &= \int_{-\infty}^{\infty} f^2 |G(f)|^2 df, \end{aligned} \tag{2.15}$$

where $G(f)$ is the frequency spectrum of $g(t)$ and f is in Hz. The calculated dispersion products for the RROW wavelets vary slightly with different q values and are listed in Table 2.1.

Comparing to the Heisenberg uncertainty lower bound achieved by a Gaussian pulse, $\Delta W \Delta T = 0.0796$, the dispersive products of the RROW wavelets have an excess of about 25%. This time-frequency localisation property is close to that of the Nyquist filter with spectrum cosine roll-off factor $\alpha_r = 0.85$ [35].

Table 2.1. Time-frequency dispersion products of RROW wavelets

q	$\Delta W \Delta T$
1	*0.1058*
2	*0.1013*
3	*0.1002*
4	*0.0997*
5	*0.0995*
6	*0.0994*
8	*0.0992*
20	*0.0991*
40	*0.0990*
100	*0.0990*

The time-frequency localisation property of the RROW wavelet with $q = 2$ is examined by plotting its ambiguity function and comparing with the optimal Gaussian pulse and rectangular pulse as shown in Fig. 2.3, Fig. 2.5 and Fig. 2.6. Because the RROW wavelet is a passband signal, the ambiguity function of its envelope function is plotted in Fig. 2.4 in order to illustrate its localsation property more clearly. We see that the RROW wavelet has good localisation in both the time and the frequency domain, while the rectangular pulse has strong sidelobes in the frequency domain.

2.4 Complex Rational Orthogonal Wavelets (CROW)

In this section we propose a new family of complex wavelets - the complex rational orthogonal wavelets (CROWs) based on the RROWs. Assume there is an MRA(a), where $a = 1 + \frac{1}{q}$ and $\phi(t)$ and $\psi(t)$ are the related scaling function and wavelet function respectively. We claim that:

1) The collection of $\hat{V}_j$, $j \in \mathbb{Z}$, where $\hat{V}_j = \{\sum_k b_k \hat{\phi}(a^j t - k),\ \{b_k\} \in \ell_2\}$, forms another MRA(a) where $\hat{\phi}(t)$ is the Hilbert transform of $\phi(t)$.
2) Let $\hat{W}_j$ be the orthogonal complement of $\hat{V}_j$ in $\hat{V}_{j+1}$, there exists a wavelet function

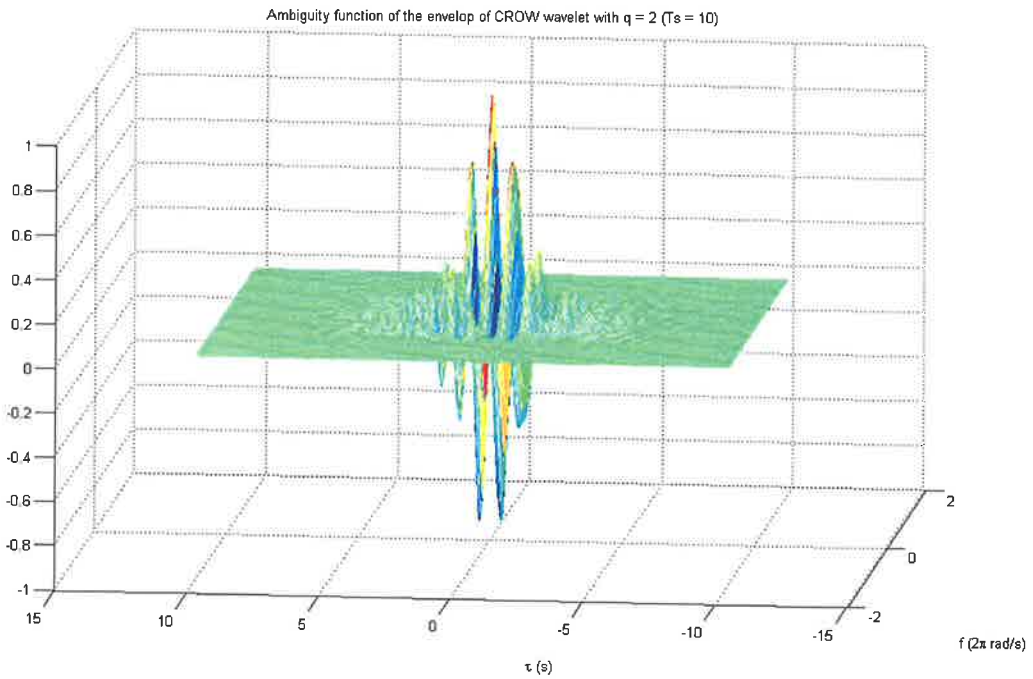

Figure 2.3. Ambiguity function of RROW with q = 2

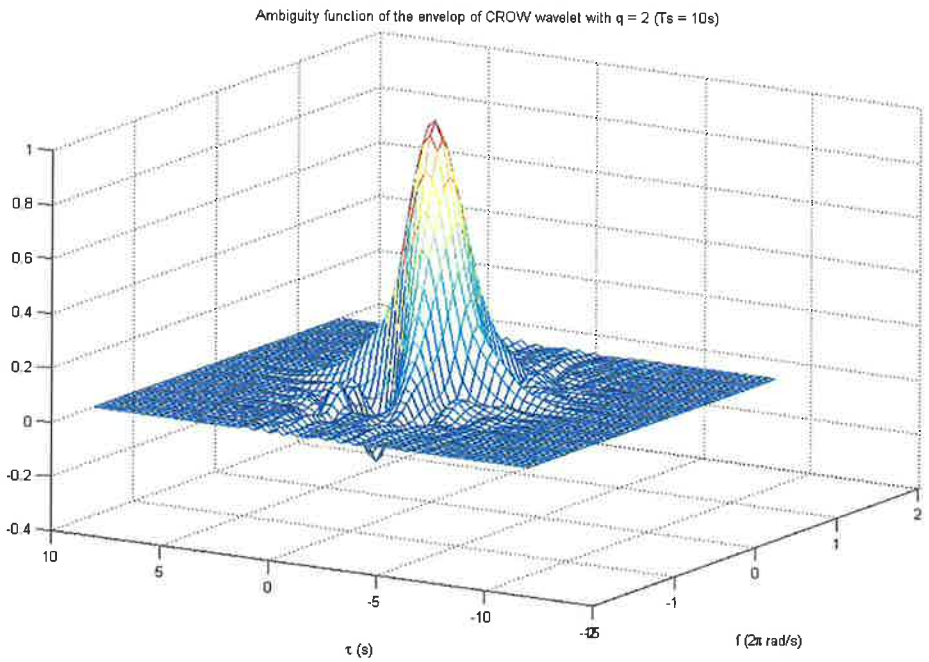

Figure 2.4. Ambiguity function of the envelope of RROW with q = 2

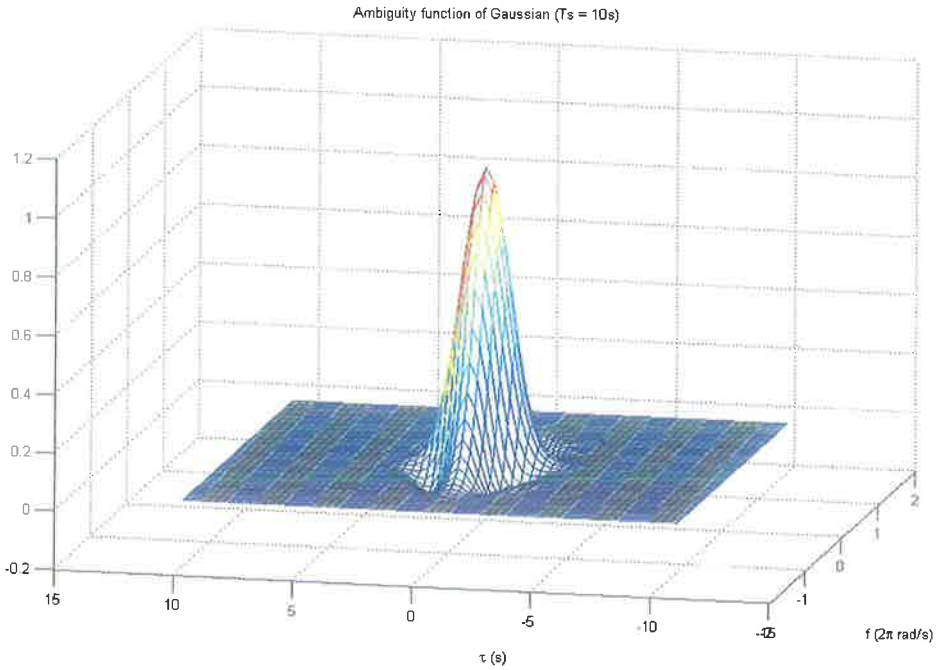

Figure 2.5. Ambiguity function of a Gaussian pulse

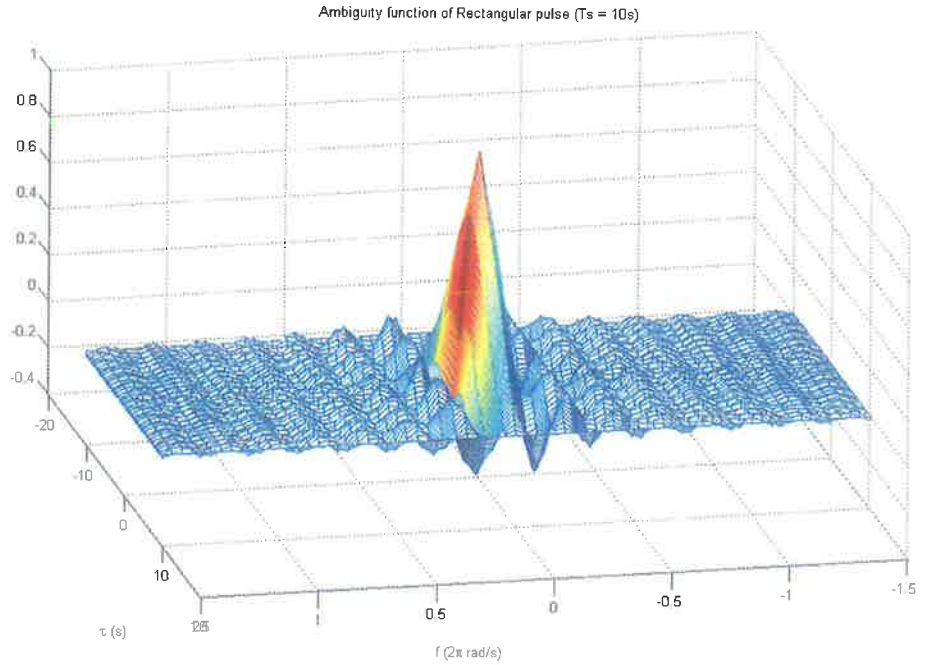

Figure 2.6. Ambiguity function of a Rectangular pulse

$\hat{\psi}(t)$ in $\hat{W}_0$ such that the collection of functions $\{\hat{\psi}_{k,n}(t) := a^{-\frac{j}{2}}\hat{\psi}(a^j t - kq),\ j,k \in \mathbb{Z}\}$ forms an orthonormal wavelet basis for $L^2(\mathbb{R})$ where $\hat{\psi}(t)$ is the Hilbert transform of $\psi(t)$.

The above claims can be further summarised by the following theorem.

Theorem 2: *If there are a scaling function $\phi(t)$ and a wavelet basis function $\psi(t)$ associated with an MRA(a) defined in Definition 1 and $a = 1 + \frac{1}{q}$, $q \in \mathbb{Z}^+$, the Hilbert transform of $\psi(t)$, $\hat{\psi}(t)$ is also a wavelet basis function associated with another MRA(a) with the orthogonality, $\int \hat{\psi}_{kn}(t)\hat{\psi}_{\ell m}(t)dt = \delta_{k-\ell}\delta_{m-n}$, $k,\ell,m,n \in \mathbb{Z}$, such that the collection of functions $\{\hat{\psi}_{k,n}(t) := a^{-k/2}\hat{\psi}(a^k t - nq),\ k,n \in \mathbb{Z}\}$ is an orthonormal basis of $L^2(\mathbb{R})$. There exists the corresponding scaling function $\hat{\phi}(t)$ which is the Hilbert transform of $\phi(t)$.*

The proof of Theorem 2 is given in Appendix A. Define complex functions, $\phi_+(t) = \phi(t) + i\hat{\phi}(t)$, and $\psi_+(t) = \psi(t) + i\hat{\psi}(t)$. Under the condition that

$$< \psi_{k,n}(t), \hat{\psi}_{l,m}(t) > = \ 0,\ k,n,l,m \in \mathbb{Z}, \tag{2.16}$$

we have the following theorem.

Theorem 3: *If there exist a scaling function $\phi(t)$ and a wavelet basis function $\psi(t)$ associated with an MRA(a), $a = 1 + \frac{1}{q}$, $q \in \mathbb{Z}^+$, the complex function $\psi_+(t)$ satisfying the condition (2.16), is a complex wavelet basis function associated with a complex MRA(a) for a complex functional space $L^2(\mathbb{R})$ with the orthogonality, $\int \psi_{+,kn}(t)\psi^*_{+,lm}(t)dt = \delta_{k-l}\delta_{m-n}$, $k,l,m,n \in \mathbb{Z}$, such that the collection of complex functions $\{\psi_{+,kn}(t) := \frac{\sqrt{2}}{2}a^{-k/2}\psi_+(a^k t - nq),\ k,n \in \mathbb{Z}\}$ is an orthonormal basis of the complex valued $L^2(\mathbb{R})$. The complex function $\phi_+(t)$ is the corresponding complex scaling function.*

The proof of Theorem 3 is verified immediately based on the two real MRA(a)s and the orthogonality between the two sets of real wavelet subspaces. Notice that the condition (2.16) imposes a constraint on the spectrum of $\psi(t)$ that

$$\Im\left[\int_0^\infty \Psi(a^k\omega)\Psi^*(\omega)e^{-i\omega q(a^k n - m)}d\omega\right] = 0,\ k,n,m \in \mathbb{Z}, \tag{2.17}$$

where $\Im[\cdot]$ returns the imaginary part of a complex signal. It can be easily proved that the Littlewood-Paley wavelet [16] satisfies orthogonality for the complex MRA exactly. We will also give examples that satisfy this condition approximately, while finding other appropriate wavelets with the exact constraint is still an ongoing question.

It is worth noting that the Hilbert transform cancels the mean value of the signal, therefore the spectrum of $\hat{\phi}(t)$ has a discontinuity at zero frequency, $\hat{\Phi}(0) = 0$. This discontinuity can be neglected if we use signals of zero mean or with the mean value (the direct current (DC) component) removed before processing which is the case for most of the signal processing problems. For the spectrum equality $|\hat{\Phi}(\omega)| = |\Phi(\omega)|$ and $\{\hat{\phi}_j(t-k), k, j \in \mathbb{Z}\}$ being the Riesz basis[1] of $\hat{V}_j$ and $\bigcup_{j\in\mathbb{Z}} \hat{V}_j = L^2(\mathbb{R})$ to be exact, we may define $\hat{\Phi}(0)$ additionally by $|\hat{\Phi}(0)| = |\hat{\Phi}(0^+)|$ or $|\hat{\Phi}(0^-)|$ in order to relax the constraint on the spaces $\{\hat{V}_j,\ j \in \mathbb{Z}\}$ spanned by functions with zero mean. The wavelet subspaces $\hat{W}_j$ are not affected by this property of Hilbert transform because of the bandpass property of $\psi(t)$.

Notice that with the method proposed in this thesis, the two MRA(a)s related to $\{\phi(t), \psi(t)\}$ and $\{\hat{\phi}(t), \hat{\psi}(t)\}$ have the same two-scale relations between the neighboring subspaces. For the dyadic case ($a = 2$), Selecnick [68] proposed another way that leads to a pair of wavelets forming the Hilbert transform pair by designing two sets of lowpass and highpass filters that converge to the corresponding scaling functions and wavelets. One of the scaling functions is the time-shifted version of the other by $\frac{1}{2}$. It is different from the Hilbert transform relation of the scaling functions in this thesis because the two MRA(2)s in [68] are based on two different sets of two-scale relations. This observation infers that for the same Hilbert transform pair of wavelets, the relation between the two scaling functions is not unique depending on the two-scale relations between the neighboring subspaces of the two MRA(a)s.

Based on the example of RROW wavelets defined in the last section, we could develop a family of CROWs forming the complex MRA approximately. Based on the definition in equation (2.12), we define the complex wavelet function as

$$\psi_+(t) = \psi(t) + j\hat{\psi}(t), \tag{2.18}$$

where $\psi(t)$ has the frequency spectrum defined in (2.12), and $\hat{\psi}(t)$ is the Hilbert transform of $\psi(t)$ and is defined in the frequency domain by

$$\hat{\Psi}(\omega) = -j\,\mathrm{sgn}(\omega)\Psi(\omega), \tag{2.19}$$

[1]See Appendix A.2 for a definition of Riesz basis.

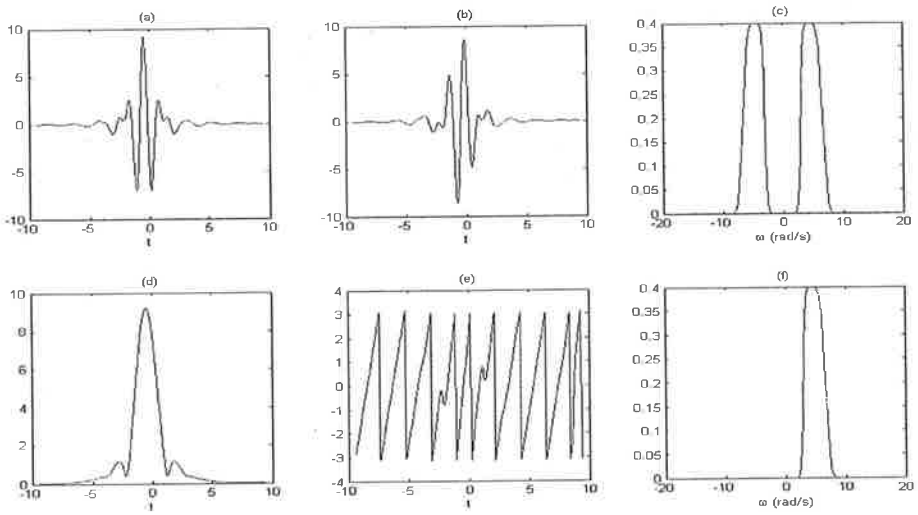

Figure 2.7. Complex Meyer wavelet with dilation factor of 2. (a) Real part of $\psi_+^{(2)}(t)$. (b) Imaginary part of $\psi_+^{(2)}(t)$. (c) Spectrum amplitude of both real and imaginary parts. (d) Modulus of $\psi_+^{(2)}(t)$. (e) Angle of $\psi_+^{(2)}(t)$. (f) Spectrum amplitude of $\psi_+^{(2)}(t)$.

where sgn(.) is the sign function defined by

$$\text{sgn}(x) = \begin{cases} 1, & x > 0 \\ 0, & x = 0 \\ -1, & x < 0. \end{cases} \tag{2.20}$$

The real part and imaginary part of the complex wavelet form a Hilbert transform pair. $\psi_+(t)$ is actually the analytic form of the RROW $\psi(t)$.

We see that three wavelets are obtained based on the definitions in (2.12), (2.19) and (2.18) respectively. The first two, $\psi(t)$ and $\hat{\psi}(t)$ are real wavelets and the third one $\psi_+(t)$ is a complex wavelet. $\psi(t)$ and $\psi_+(t)$ are symmetric and $\hat{\psi}(t)$ is anti-symmetric. The frequency spectrum of the complex wavelet, $\Psi_+(\omega)$ is supported on $\omega \geq 0$. Three examples of designed complex wavelets are shown in Fig. 2.7, Fig. 2.8 and Fig. 2.9.

To examine the validity of the orthogonality condition on the wavelet spectrum as shown in equation (2.17), we calculate the cross correlation of the scaled and shifted wavelet basis functions, $R_{k,n} =< \psi(a^k t), \hat{\psi}(t - nq) >$. The correlation parameters for two wavelets with $q = 1, 2, 3$ are plotted in Fig. 2.10. Although the spectrum constraint in (2.17) does not hold exactly for all CROWs when k = 0,1, the orthogonality condition

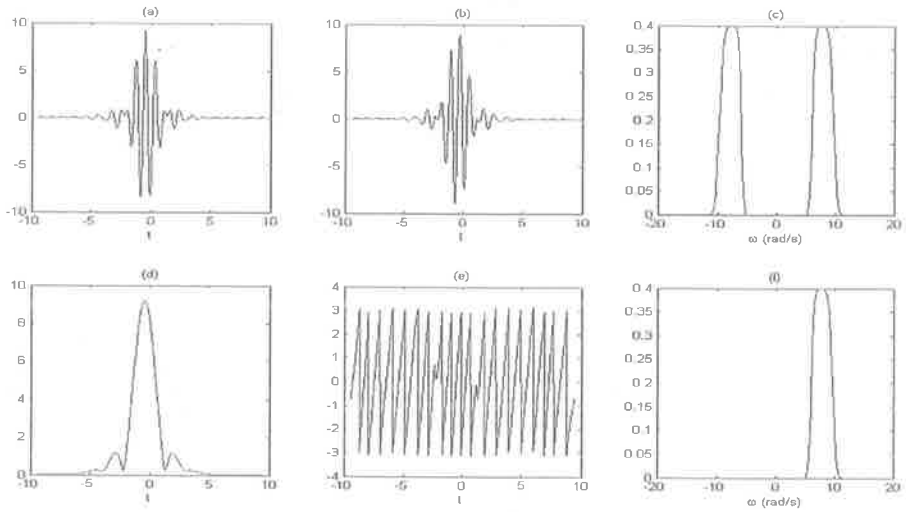

Figure 2.8. Complex rational orthogonal wavelet with dilation factor of 3/2. (a)~(f) show the corresponding figures for $\psi_{+}^{(\frac{3}{2})}(t)$ as specified in Fig. 2.7.

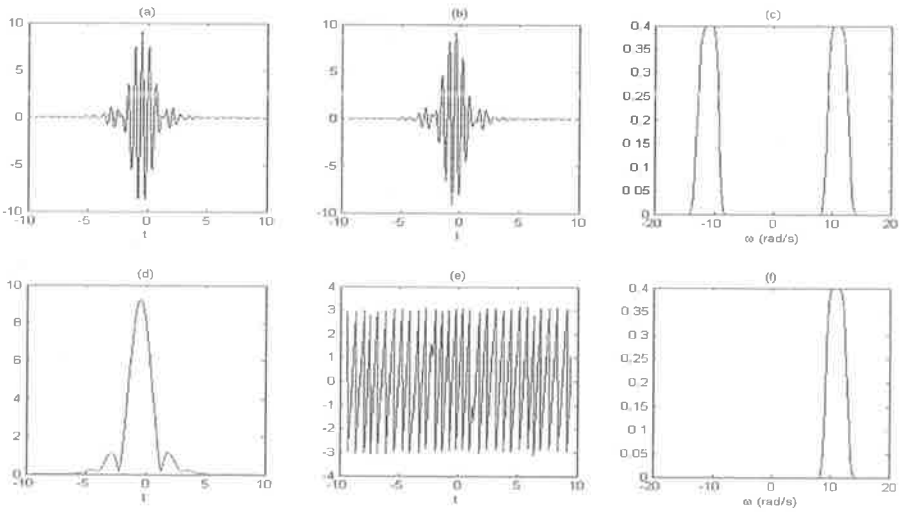

Figure 2.9. Complex rational orthogonal wavelet with dilation factor of 4/3. (a)~(f) show the corresponding figures for $\psi_{+}^{(\frac{4}{3})}(t)$ as specified in Fig. 2.7.

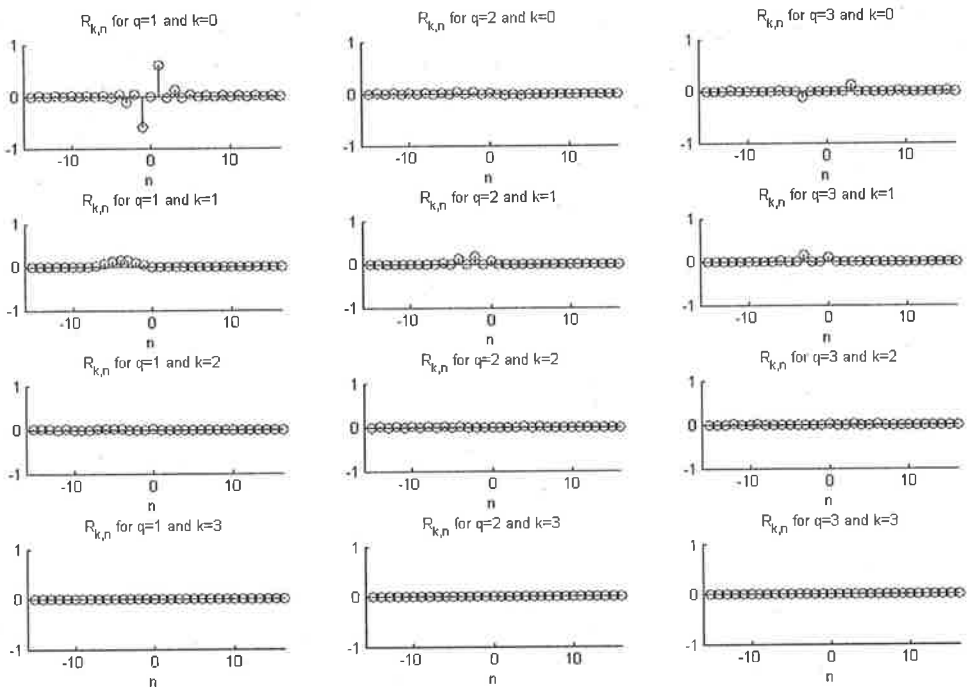

Figure 2.10. Cross correlation of the scaled and shifted wavelet basis functions.

holds with high fidelity except for the complex Meyer wavelet ($q = 1$). It has relatively large correlation at $n = 1$ within one scale ($k = 0$), which indicates that the complex Meyer wavelet retains good scale and shift orthogonality except for the shift orthogonality of integer 1. Notice the difference that the real Meyer wavelet (RROW with $q = 1$) has this shift orthogonality of integer 1. Although strictly not accurate, we still refer to the complex Meyer wavelet as one of the CROWs based on its scale orthogonality and shift orthogonality of integer $n > 1$, and study its properties together with the other CROWs.

Another interesting finding about the shift orthogonality of the CROWs is that, in addition to the theoretical integer q shift orthogonality for the CROW with scale factor of $a = 1 + 1/q$ which is proved under the rational MRA framework, all CROWs retain a shift orthogonality of integer 2. This orthogonality does not hold exactly but with high fidelity. A proof of this shift-2 orthogonality is detailed in Appendix A.4.

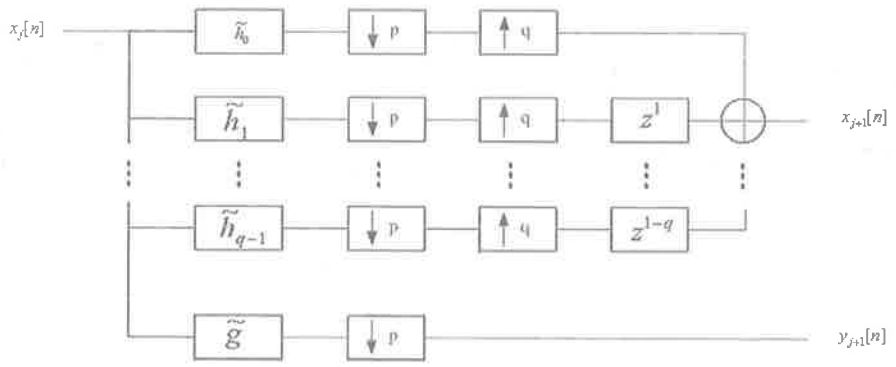

Figure 2.11. Analysis filter bank of real rational orthogonal wavelet (p = q+1)

2.5 Fast Wavelet Transform Algorithms

2.5.1 Time-domain Real FWT Algorithm for RROWs

In Baussard's paper [16], the fast algorithm for RROWs was given and implemented in the frequency domain. The corresponding pyramid analysis and synthesis algorithms for real ROW with $a = \frac{q+1}{q}$ are shown in Fig. 2.11 and Fig. 2.12.

The lowpass filters are computed by

$$H_n(\omega) = \sqrt{a}\frac{\Phi(a\omega)}{\Phi(\omega)}e^{-ina\omega}, \tag{2.21}$$

where $n = 0, \cdots, q-1$. The highpass filter is given by

$$G(\omega) = \sqrt{a}\frac{\Psi(a\omega)}{\Phi(\omega)}. \tag{2.22}$$

For simplicity, the notations $H_n(\omega)$ and $G(\omega)$ are used which are also known as $H_n(e^{j\omega})$ and $G(e^{j\omega})$ for discrete filters. The filters are of infinite length in the time domain, therefore the pyramid algorithm in [16] was implemented in the frequency domain in order to take advantage of the definition of filters in the frequency domain. However, the time domain FB algorithm might be preferable to the block-by-block algorithm in the frequency domain, especially for communications applications. We therefore propose an FIR approximation of the fast analysis and synthesis algorithms not restricted to the perfect reconstruction property but with a fidelity that suits communications applications.

Following the FB construction for the dyadic Meyer wavelet as shown in [80], we give the example of FB construction for the CROW wavelet with $q = 2$ and $a = \frac{q+1}{q} = \frac{3}{2}$.

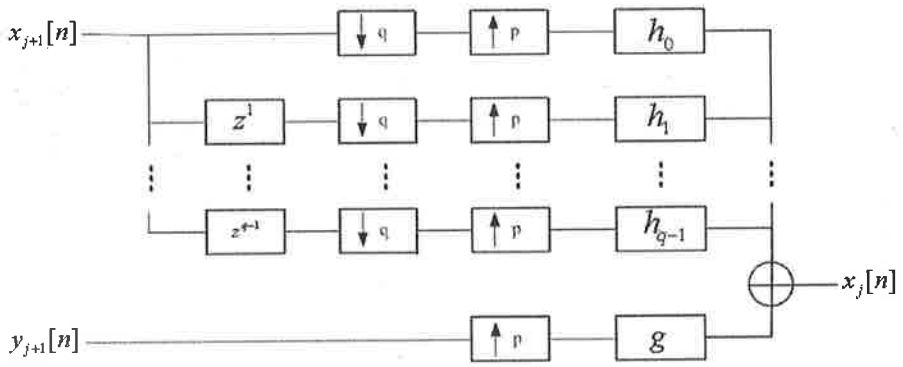

Figure 2.12. Synthesis filter bank of real rational orthogonal wavelet (p = q+1)

The filters $h_n[n]$ and $g[n]$ are constructed by synchronous sampling of the continuous filters $h_n(t)$ and $g(t)$ which are numerically constructed based on their definitions in the frequency domain by (2.21) and (2.22). The lowpass and highpass synthesis filters $h_0[n]$, $h_1[n]$ and $g[n]$ are shown in the Fig. 2.13. Note that to conform to the spectrum of the continuous filters $h_n(t)$ and $g(t)$, the sampling rate f_s is selected to be greater than or equal to the Nyquist rate $f_s^{Nyquist} = q + \frac{q}{2q+1}$ instead of 1. In Fig. 2.13, the sampling rate is $f_s = q + 1/2 = 2.5$. Accordingly, the analysis FB for time-frequency analysis applications would require over-sampled input signals (2.5 times the Nyquist sampling rate). Notice that the constructed filters $h_0[n]$, $h_1[n]$ and $g[n]$ are therefore related to a redundant MRA structure of a frame $\{\psi^{(a)}_{b0;j,k}(t) := a^{\frac{j}{2}}\psi(a^j t - kb_0),\ a = \frac{3}{2},\ b_0 = f_s\}$, rather than an R-wavelet $\{\psi^{(a)}_{1;j,k}(t),\ a = \frac{3}{2}\}$ (refer to Appendix A.2 for the definitions of frame and R-wavelet). This redundancy leads to the shift-invariance property of the FB which is closely related to the issue of synchronisation for communication applications. A proof of the shift-invariance property is presented in section 2.6.

As a verification of the equality of the direct WT and the tree-structured FWT algorithms, we examine the convergence of the iteration of the synthesis filters. Based on the two-scale relation of the rational MRA as shown in equations (2.21) and (2.22), there are

$$\Phi(a\omega) = a^{-\frac{1}{2}} H_n(\omega) e^{jna\omega} \Phi(\omega) \tag{2.23}$$

$$\Psi(a\omega) = a^{-\frac{1}{2}} G(\omega) \Phi(\omega). \tag{2.24}$$

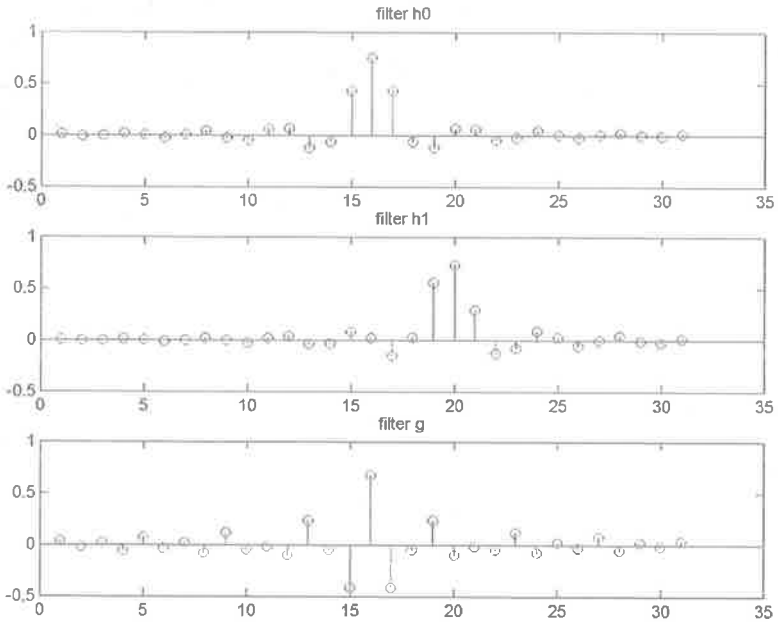

Figure 2.13. Synthesis filters h0, h1, g for real rational orthogonal wavelet (a = 3/2)

Therefore, the wavelet function can be generated by

$$\Psi(\omega) = a^{-\frac{1}{2}} G(a^{-1}\omega)\Phi(a^{-1}\omega) \tag{2.25}$$

$$= a^{-\frac{1}{2}} G(a^{-1}\omega) \prod_{k=2}^{\infty} \{a^{-\frac{1}{2}} H_n(a^{-k}\omega) e^{jna^{-(k-1)}\omega}\}\Phi(0), \tag{2.26}$$

where $\Phi(0) = 1$. Based on the filters shown in Fig. 2.13, the wavelet function $\psi^{(\frac{3}{2})}(t)$ can be generated by the iteration of g and $h0$ ($n = 0$), or g and $h1$ ($n = 1$). Fig. 2.14 shows the comparison of the real ROW wavelet $\psi^{(\frac{3}{2})}(t)$ and the output of 2, 4 and 6 iterations of the constructed synthesis filters. The resemblance of the wavelet function and iteration outputs demonstrates good convergence of the tree-structured FWT.

2.5.2 Time-domain FWT Algorithm for CROWs

The IWT/WT FB for RROWs facilitates pulse amplitude modulation (PAM) for RROW-based signalling [90]. In comparison, the CROWs form complex signalling pulses and facilitate the transmission of complex symbols for phase-shift keying (PSK) modulation or

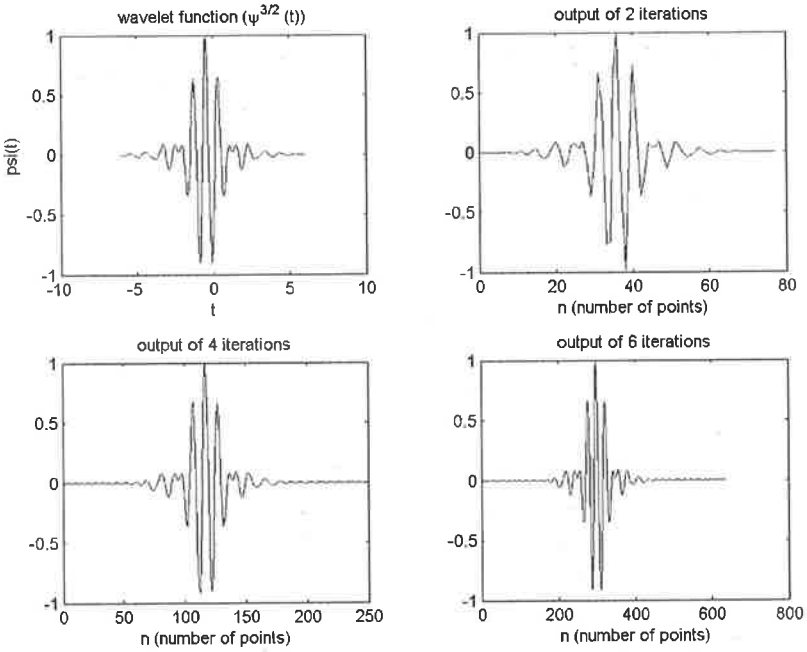

Figure 2.14. Convergence of iterated FB to the wavelet function

quadrature amplitude modulation (QAM). As shown in section 2.5.1, the tree-structured IWT/WT FB for RROWs is based on the real MRA structure and the related real scaling and wavelet filters. For CROWs, a complex MRA is involved. As discussed in [92], for a complex wavelet $\psi_+(t)$ whose real and imaginary parts ($\psi(t)$ and $\hat{\psi}(t)$) form a Hilbert transform pair, the way it related to a complex MRA structure is not unique. It depends on the two-scale relations between the neighboring subspaces of the two real MRA(a)s related to real wavelets $\psi(t)$ and $\hat{\psi}(t)$ respectively.

Based on a known real MRA denoted by its wavelet and scaling function $\{\psi(t), \phi(t)\}$, we seek the construction of another real MRA whose wavelet function is $\hat{\psi}(t)$, and the construction of a complex MRA whose wavelet function is $\psi_+(t) = \psi(t) + j\hat{\psi}(t)$. One solution could be found in [67] for dyadic wavelets. Based on the known real MRA $\{\psi(t), \phi(t)\}$, the corresponding scaling function for $\hat{\psi}(t)$ is the 1/2 shift of the scaling function for $\psi(t)$. Two sets of scaling and wavelet filters are constructed for the two real MRA structures. The two scaling filters are offset to each other by a half sample and the two wavelet filters form a Hilbert transform pair. The two scaling filters and two wavelet filters then form the real and imaginary parts of the complex scaling filter and

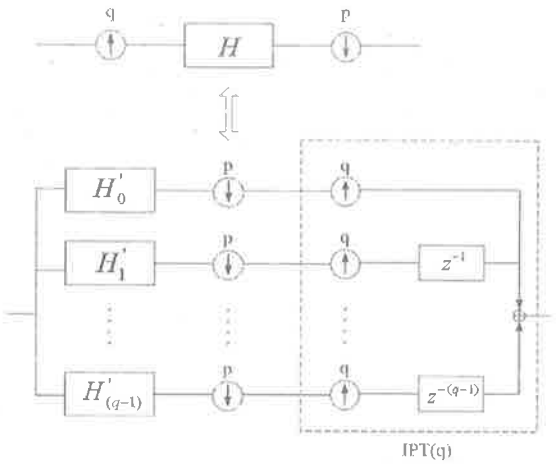

Figure 2.15. Direct design of rational sampling FB

complex wavelet filter respectively to construct the complex MRA. Another solution is based on the Theorem 3 proposed in section 2.4. The corresponding scaling function for $\hat{\psi}(t)$ is $\hat{\phi}(t)$, the Hilbert transform of the scaling function for $\psi(t)$, which leads to the complex scaling function of $\phi_+(t) = \phi(t) + j\hat{\phi}(t)$. The two real MRA(a)s $\{\phi(t), \psi(t)\}$ and $\{\hat{\phi}(t), \hat{\psi}(t)\}$ have the same two-scale relations (or scaling and wavelet filters) between the neighboring subspaces. In other words, the complex MRA $\{\phi_+(t), \psi_+(t)\}$ involves only real scaling and wavelet filters the same as those for the two real MRAs as shown in section 2.5.1.

2.6 The Connection with Rational Sampling Filter Banks

The synthesis/analysis FBs shown in Fig. 2.11 and Fig. 2.12 can be further simplified into 2-branch FBs based on the observation of the strong resemblance of Baussard's FB and Kovacevic and Vetterli's rational sampling PR FB of the direct design method [47]. The connection between the two FBs provides a method to simplify Baussard's FB by replacing the parallel lowpass FB with a single branch. On the other hand, the knowledge of Baussard's FB gives a solution to the design of rational sampling FB based on the rational orthogonal wavelet.

The direct design method in [47] is based on the equivalent FB structures shown in Fig. 2.15. The proposed direct design method transforms a single branch with upsampling

by q and downsampling by p to a q-channel analysis bank with downsampling by p and an inverse polyphase transform of size q, assuming q and p are coprime and $q > 1$. The filters in the q-channel analysis bank are defined by

$$H_i'(z) = z^{d_i} H_{t_i}^{(v)}(z), \tag{2.27}$$

where $d_i = \lfloor p \cdot i/q \rfloor$ ($\lfloor x \rfloor$ denotes the largest integer not greater than x), $t_i = p \cdot i \bmod q$ and $H_0^{(v)}$, ..., $H_{q-1}^{(v)}$ are the polyphase components of H with respect to q. The rational sampling FB design problem is reduced to finding a perfect reconstruction structure for a q-channel filter bank, with design constraints imposed on filters $H_0^{(v)}, ..., H_{q-1}^{(v)}$.

The above relations between the single branch rational sampling filter H and the parallel FB H_i' can be utilised directly to simplify Baussard's FB by replacing the parallel lowpass filters h_n, $n = 0, \cdots, q-1$ in Fig. 2.11 with a single branch filter with rational sampling factor p/q as shown in Fig. 2.15. The equivalent filter H is derived as

$$\begin{aligned} H(z) &= H_0(z^q) + z^{-(1+p+q)} H_0(z^q) + \cdots + z^{-(q-1)(1+p+q)} H_0(z^q) && (2.28)\\ &= (1 + z^{-(1+p+q)} + \cdots + z^{-(q-1)(1+p+q)}) H_0(z^q) && (2.29)\\ &= A(z^{(1+p+q)}) H_0(z^q), && (2.30) \end{aligned}$$

where $A(z) = 1 + z^{-1} + z^{-2} + \cdots + z^{-(q-1)}$. $H_0(z)$ is given by equation 2.21 with $n = 0$. The derivation is presented in Appendix A.4.

The connection between the two FBs shown in Fig. 2.11 and Fig. 2.15 also gives a solution to the design of rational sampling FB with sampling factor of p/q, $p = q + 1$, based on the rational orthogonal wavelet with scale factor of $a = p/q = 1 + 1/q$. The nature of the continuous WT/IWT FBs forms the basis of perfect reconstruction (PR) and shift-invariance (SI) properties of the designed rational sampling FB. The PR property is verified immediately based on the essence of the wavelet transform pair. The shift-invariant property of the iterated FB can be examined by evaluating the two-scale relation of the wavelet lowpass filters $\tilde{h}_i$ and the highpass filter g proposed in [16]:

$$a_{j,sq+i} = \sum_r \tilde{h}_i[ps - r] a_{j-1,r}, \tag{2.31}$$

$$d_{j,n} = \sum_r \tilde{g}[pn - r] a_{j-1,r}, \tag{2.32}$$

where $a_{j,n}$ and $d_{j,n}$ are the approximation and detail coefficients at the wavelet subspace W_j with shift integer of n, and $s, r, i, j, n \in \mathbb{Z}$. A shift of the approximation and detail coefficients by 1 leads to the relations that

$$a_{j,(s-1)q+i} = \sum_r \tilde{h}_i[ps - r]a_{j-1,r-p}, \tag{2.33}$$

$$d_{j,(n-1)} = \sum_r \tilde{g}[pn - r]a_{j-1,r-p}, \tag{2.34}$$

which infers that a delay of 1 at stage j means a delay of p^j for the input signal. Therefore, the FBs shown in Fig. 2.11 and Fig. 2.12 have the SI property. Notice that the FIR approximation of the wavelet analysis/synthesis filters prevents the WT/IWT, and thus the PR and SI properties to be exact. However both properties hold with high fidelity based on the good convergence of the FIR approximation to the continuous wavelet transform as shown in section 2.5.1.

2.7 Computational Complexity of FWT

It is well known that given N input samples, the computational complexity of FWT for dyadic wavelets is $O(N + N/2 + N/4 + \cdots + N2^{-(J-1)}) = O(N)$, where J is the number of tree levels. The number of data samples is halved after the filtering of each tree node.

Based on the FWT algorithm proposed in section 2.5, the computational complexity of FWT for RROW/CROW can be evaluated in a similar manner. The computational complexity has the order of $O(N + Na^{-1} + Na^{-2} + \cdots + Na^{-(J-1)}) = O(N)$, where a is the scale factor.

2.8 Conclusions

The main contributions of this chapter are summarised in the following together with some remarks.

1) Explicit formulae are derived for the definition of a special class of RROWs with a good time-frequency localisation property desirable for communication applications.

Based on the general definition of RROWs in Baussard's paper [16], this chapter develops explicit formulae (2.11), (2.12) to define a family of RROWs as a special case. It has no constant band between the two transition bands defined by a selected construction function, which leads to a good decay property in the time domain.

2) The time-frequency localisation property of the RROWs is analysed.

An analytic evaluation of the time-frequency dispersion products of the RROWs reveals a good time-frequency localisation property which is about 25% excess of the Heisenberg uncertainty lower bound achieved by a Gaussian pulse and close to that of the Nyquist filter with spectrum cosine roll-off factor $\alpha_r = 0.85$.

3) A theoretical proof is given for the argument that the Hilbert transform of one wavelet forms another wavelet from the MRA point of view.

It has been pointed out that we can always take the Hilbert transform of one wavelet to form another wavelet [68]. A theoretical verification of this argument is given by proving the Theorem 2 proposed in section 2.4.

4) A generalised method is proposed to construct complex wavelets under the framework of rational MRA(M), where M is a rational number.

A generalised method to construct complex wavelets is proposed as Theorem 3 in section 2.4. The orthogonality condition and the corresponding constraint on the spectrum of the wavelet basis function are derived to form complex orthogonal wavelets related to a complex rational MRA structure.

5) A new family of complex wavelets - CROWs is proposed which forms a complex MRA approximately.

Based on the special class of RROWs with good time-frequency localisation property and the generalised method to construct complex wavelets, a new family of complex wavelets - CROWs is proposed which meets the complex orthogonality condition (2.16) approximately. The CROWs have many desirable properties including

- explicit expression in the frequency domain,

- rational scale orthogonality,
- shift orthogonality,
- compact support in the frequency domain by $2\pi(rad/s)$,
- effective support in the time domain by [-8, 8],
- symmetry - symmetry for the real part and anti-symmetry for the imaginary part,
- quadrature between real and imaginary parts,
- good time-frequency localisation - a time-frequency dispersion product of 25% in excess of the Heisenberg uncertainty lower bound,
- availability of a fast wavelet transform (FWT) with computational complexity of $O(N)$.

With the unique rational orthogonality, this family of wavelets is a promising signal processing tool for many application fields in image processing and communications. In particular, CROW's scale/shift orthogonality and good time-frequency properties form the basis of CROW-based multicarrier modulation (MCM)/OFDM schemes for broadband communications, which is detailed in chapter 3. Its explicit expression in the frequency domain, good time-frequency localisation, and shift orthogonality also makes it a good candidate of optimum shaping pulse in single carrier modulation schemes. CROW's application in three specific communication scenarios based on both single wavelet pulse signalling and CROW-based OFDM are detailed in chapter 4, chapter 5, and chapter 6 respectively.

6) Time-domain FWT algorithms are derived for RROWs and CROWs.

Since the CROW wavelet is infinite in the time domain, there is no FIR solution of the analysis/synthesis filters for the fast wavelet transform (FWT). The FWT that is available is implemented in the frequency domain as shown in [16], or by a FIR-based approximation similar to the derivation of the discrete Meyer (dMeyer) wavelet from the Meyer wavelet as derived in section 2.5.

The availability of the time-domain FWT algorithm facilitates CROW's practical applications in real-time communication systems. In addition, the connection between the

FWT FB and the rational sampling FB provides a method to simplify the FWT FB and further reduce the computational complexity.

7) A generalised solution is proposed for the design of rational sampling FB with good PR and SI properties based on the tree-structured FWT FB.

The connection between the FWT FB and the rational sampling FB also gives a generalised solution to the design of rational sampling FB with sampling factor of p/q, p = q+1, based on the knowledge of the rational wavelet FB with scale factor of a = p/q = 1+1/q. The nature of the continuous WT/IWT FBs forms the basis of perfect reconstruction (PR) and shift-invariance (SI) properties of the designed rational sampling FB. Although the FIR approximation of the wavelet analysis/synthesis filters prevents the WT/IWT, and thus the PR and SI properties to be exact, the PR and SI properties hold with high fidelity based on the good convergence of the FIR approximation.

This page is blank

Chapter 3

CROW-based Orthogonal Frequency Division Multiplexing

3.1 Introdution

Based on the complex rational orthogonal wavelet (CROW) with a fractional dilation factor $a = 1 + \frac{1}{q}$, $q \in \mathbb{Z}^+$ proposed in chapter 2, a new OFDM scheme is proposed in this chapter. As mentioned in chapter 1, the existing OFDM schemes could be classified into two categories according to the type of subcarrier pulse shaping filters - the *DFT-based OFDM* [81], [23], [21] and the *wavelet-based OFDM* [60], [51], [31]. A DFT-based OFDM scheme achieves good ISI suppression by adding a cyclic prefix (CP) but is very sensitive to frequency dispersion due to the large sidelobes of the subcarrier spectrum that cause severe inter-carrier interference (ICI) because of the loss of orthogonality among subcarriers. In contrast, the orthogonality and time-frequency localisation properties of CROWs form the basis of the CROW-based OFDM scheme with good inter-symbol interference (ISI)/inter-channel interference (ICI) mitigation through time-frequency dispersive channels. Compared with the existing wavelet-based OFDM schemes which are all based on dyadic wavelet or dyadic wavelet packets with a scale factor of 2, the CROW-based OFDM scheme has an improved bandwidth efficiency based on a fractionally dilated and overlapped tiling of the T-F plane.

The power spectral density (PSD) and bandwidth efficiency of the CROW-based OFDM signal are analysed. More specifically, it is revealed that for a special case of

CROW-OFDM with $q = 1$, significant improvement on bandwidth efficiency is achieved which reaches 1.5 times the 'maximum' value 1 symbol/Hz/s achieved by DFT-based OFDM without CP. The CROW-OFDM transceiver design is presented based on the CROW synthesis/analysis FBs proposed in chapter 2.

The chapter is organised as follows. In section 3.2, we present the construction of the CROW-OFDM signal. Its ISI/ICI cancellation properties are discussed in section 3.3. Section 3.4 and section 3.5 examine the PSD and bandwidth efficiency of the CROW-OFDM signal respectively. The CROW-OFDM transceiver design is detailed in 3.6. Section 3.7 presents the conclusions of this chapter.

3.2 CROW-OFDM Signal Construction

For comparison, we show both the DFT- and CROW-based OFDM signal construction. The traditional DFT-based OFDM signal can be expressed as a sum of single carrier modulated signals:

$$x(t) = \sqrt{\frac{E_s}{N}} \sum_k \sum_{n=0}^{N-1} c_{n,k} e^{2j\pi(f_0+n\Delta f)t} g(t - kT_s), \tag{3.1}$$

where N is the number of subcarriers, $g(t)$ is the pulse function, Δf is the frequency offset between carriers, E_s is the power of the signal, $T_s = T_u + T_g$ is the time of the complete OFDM signal where T_u is the useful time, T_g is the guard time, $c_{n,k}$ is the complex symbol sequence, and f_0 is the frequency component for carrier modulation that moves the baseband OFDM signal to the desired frequency band.

The CROW-based OFDM signal can be expressed as

$$x(t) = \sqrt{\frac{E_s}{N}} \sum_k \sum_{n=0}^{N-1} c_{n,k} \psi_+(a^{(n_0+n)}t - kT_s), \tag{3.2}$$

where $\psi_+(t)$ is the wavelet basis function, a is the wavelet dilation factor, and n_0 is the initial scale factor that controls the bandwidth of the OFDM signal.

One special feature of the CROW-based OFDM (similar to the dyadic wavelet-based OFDM) is that each subchannel has a different symbol period valued at $a^{-(n_0+n)}T_s$ for the n-th channel. At the receiver, the symbol sequence $c_{n,k}$ is recovered by the perfect reconstruction (PR) wavelet analysis filter bank followed by multirate sampling. The

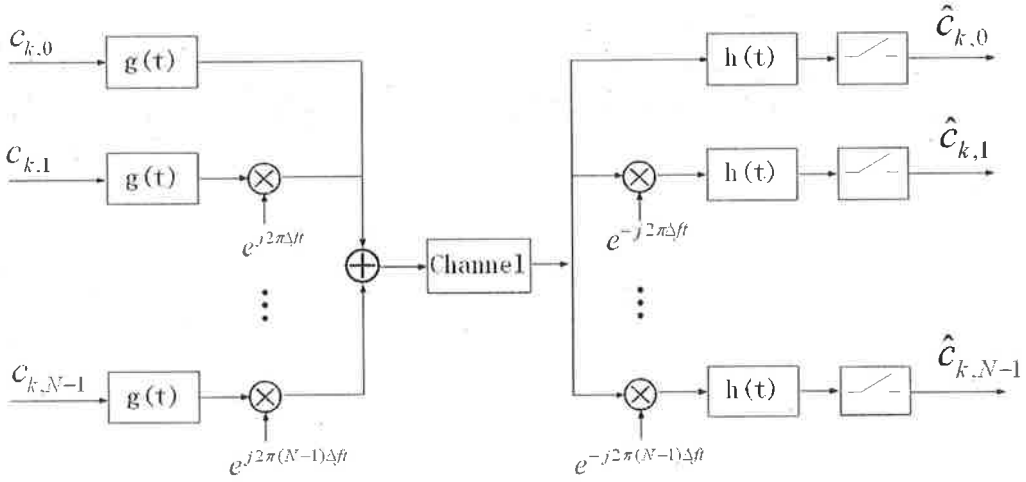

Figure 3.1. Block diagram of DFT-OFDM

block diagrams of the modulation/demodulation process for the DFT- and CROW-based OFDM systems are shown in Fig. 3.1 and Fig. 3.2 respectively. The function $h(t)$ in Fig. 3.1 is a filter matched to the pulse function $g(t)$ and $h(t) = g^*(-t)$.

3.3 ISI and ICI Cancellation Property of CROW-OFDM Signal

As discussed in chapter 2, the CROW wavelets have rational orthogonality controlled by the parameter q. The orthogonal wavelet subspaces have the dilation factor of $a = 1 + \frac{1}{q}$. We define $\psi_{kn}(t) = a^{-k/2}\psi(a^k x - nq)$, where $k, n \in \mathbb{Z}$, $a = 1 + \frac{1}{q}$, $q \in \mathbb{Z}^+$. The function $\psi_{+,kn}(t)$ is defined as the analytic form of $\psi_{kn}(t)$. The wavelet basis function $\psi_+(t)$ has the orthogonality

$$\int \psi_{+,kn}(t)\psi^*_{+,lm}(t)dt = 2\delta_{k-l}\delta_{m-n}, \quad k, l, m, n \in \mathbb{Z}, \tag{3.3}$$

such that the collection of functions $\{\frac{\sqrt{2}}{2}a^{-k/2}\psi(a^k x - nq),\ a = 1 + \frac{1}{q},\ k, n \in \mathbb{Z}\}$ is an orthonormal basis for the complex valued $L^2(\mathbb{R})$. This orthogonality of the CROW bases makes it qualify as a candidate of the orthogonal OFDM subcarrier pulse shaping filters.

For multicarrier modulations, the time-frequency localisation property of the carriers is important for the transmission over a dispersive channel. A good time-frequency

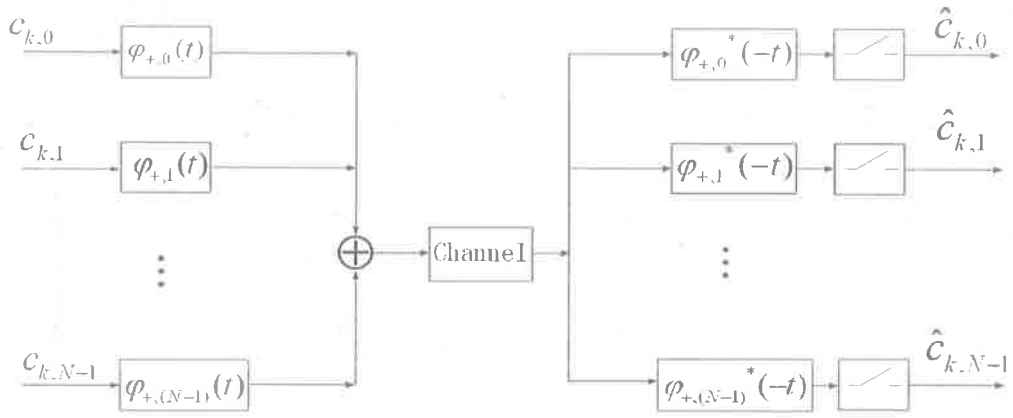

Figure 3.2. Block diagram of CROW-OFDM

localisation property will reduce the ISI and ICI caused by the loss of orthogonality between subcarriers [35]. An investigation on the time-frequency localisation property of the CROWs is presented in chapter 2, section 2.3. The time-frequency dispersive products of the CROW wavelets are calculated, which have an excess of about 25% compared to the Heisenberg uncertainty lower bound and are close to that of the Nyquist filter with spectrum cosine roll-off factor $\alpha_r = 0.85$ [35]. An illustration of the ambiguity functions of the CROW wavelet basis function with $q = 2$ and a rectangular pulse in Fig. 2.4 and Fig. 2.6 shows that the CROW wavelet has good localisation in both the time and the frequency domain, while the rectangular pulse for DFT-OFDM has strong sidelobes in the frequency domain. The good time-frequency localisation property of the CROW basis leads to improved ISI and ICI mitigation performance in time-dispersive channels because of reduced spectrum sidelobes compared to the conventional rectangular pulse based DFT-OFDM. This ISI and ICI cancellation property of the CROW-OFDM is further demonstrated by supporting simulations through time and frequency dispersive channels detailed in chapter 6.

3.4 Power Spectral Density of CROW-OFDM Signal

As detailed in chapter 2, the CROWs are derived from a rational MRA. The wavelet subspaces are generated by the span of wavelet bases

$$W_{+,k} = \overline{\text{Span}\{\frac{\sqrt{2}}{2}a^{-k/2}\psi_+(a^k t - nq)\}},\ k,n \in \mathbb{Z}. \tag{3.4}$$

Define the space

$$V_{+,k} = \overline{\text{Span}\{\frac{\sqrt{2}}{2}a^{-k/2}\phi_+(a^k t - n)\}},\ k,n \in \mathbb{Z}. \tag{3.5}$$

There is

$$\begin{aligned} V_{+,(k+1)} &= V_{+,k} \oplus W_{+,k} \\ &= \overline{\oplus_{j\in(-\infty,k]} W_{+,j}}; \end{aligned} \tag{3.6}$$

Therefore, the CROW-based OFDM signal $x(t)$ defined in (3.2) lies in the finite sum of subspaces $\overline{\oplus_{j\in[n_0,n_0+(N-1)]}W_{+,j}} \subset V_{+,(n_0+N)}$. The power spectral density (PSD) of the CROW-based OFDM can then be derived as

$$S_{CROW}(\omega) = E_s|\Phi_{+,(n_0+N)}(\omega T_s)|^2, \tag{3.7}$$

where E_s is the signal energy, $\Phi_{+,(n_0+N)}(\omega)$ is the frequency spectrum of $\phi_{+,(n_0+N)}(t) = \phi_+(a^{(n_0+N)}t)$. This result indicates that similar to the dyadic wavelet based OFDM [51], the CROW-OFDM signal has a bandwidth requirement equivalent to a QAM signal with $\phi_{+,(n_0+N)}(t)$ as the signalling pulse, and could be used on channels currently supporting QAM modulation [51].

3.5 Bandwidth Efficiency of CROW-OFDM Signal

Following Lindsey's derivation of bandwidth efficiency for dyadic wavelet/wavelet packet-based OFDM in [51], the bandwidth efficiency of the CROW-based OFDM signal can be derived as

$$\begin{aligned} \rho_{CROW} &= \frac{B}{1+\beta}\frac{2\pi}{a^2\omega_1}(1+\sum_{i=1}^{J} a^{l_i}) \\ &= \frac{B}{1+\beta}(1+a^{-1}), \end{aligned} \tag{3.8}$$

where B is the number of bits per symbol. β is the percent excess bandwidth required beyond the Nyquist signalling bandwidth and is defined by $\beta = \Delta f_\psi Ts - 1 = \eta_l^{-1} - 1$, where η_l is the density of the discrete lattice of the transmit points formed by $\psi(t)$ in phase space [35], Δf_ψ is the frequency bandwidth of the wavelet basis function $\psi(t)$ and T_s is the symbol period equivalent to the truncation length of $\psi(t)$, T_ψ, with non-overlapped signalling. The scale l_i's come from the rational overlapped partition of the interval $[0, 1)$ with dilation factor of a and $\sum_{i=1}^{J} a^{l_i} = q$. The factor $\frac{2\pi}{a^2\omega_1}$ is introduced for normalisation purposes because the spectrum of the wavelet basis is localised between ω_1 and $a^2\omega_1$ as defined in section 2.2. For comparison, as derived in [51], the bandwidth efficiency of the dyadic wavelet and wavelet packet-based OFDM signals with dyadic partition of the interval $[0, 1)$ and the spectrum of the wavelet basis function localised between π and 2π, are given as $\rho_{DWM} = \rho_{WPM} = \frac{B}{1+\beta}$. The bandwidth efficiency ρ_{CROW} has a gain of $(1 + a^{-1})$ over ρ_{DWM} and ρ_{WPM} for similar β values. The improved bandwidth efficiency can be illustrated by the tiling of the T-F plane with the 4/3 wavelet as shown in Fig. 3.3. The spectrum of the wavelet basis function $\psi_+^{(\frac{4}{3})}(t)$ is localised between $\frac{18\pi}{7}$ and $\frac{32\pi}{7}$ with a bandwidth of 2π (rad/s).

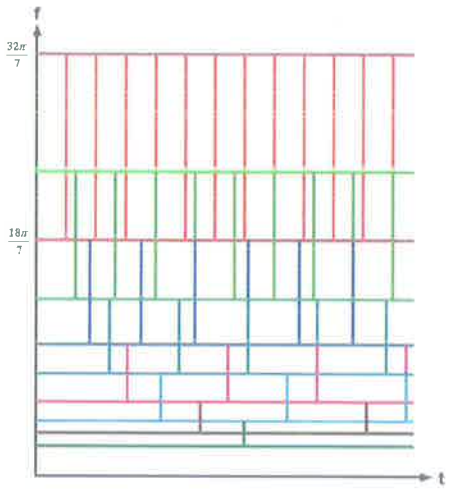

Figure 3.3. T-F tiling of the 4/3 wavelet

An interesting feature of the CROW-based OFDM is that the overlapped (OL) signalling can be adopted to improve the bandwidth efficiency based on the shift-orthogonal property of the wavelets. Assuming a truncation length $T_\psi = 10$ (s), the density of non-overlapped signalling $\eta_l^{NOL} = \frac{1}{\Delta f_\psi T_s} = 0.1$, where $T_s = T_\psi$ and $\Delta f_\psi = 1$ (Hz). With OL

signalling, we have $\eta_l^{OL} = \frac{T_\psi}{q}\eta_l^{NOL} = \frac{1}{q}$. The possible q has to be less than T_ψ for the overlapping scheme to make sense. An illustration of the achieved bandwidth efficiency for different q values with both non-overlapped (NOL) and OL signalling is shown in Fig. 3.4. Notice that a significant improvement on bandwidth efficiency is achieved for $q = 1$ with a bandwidth efficiency of $1.5B$ (bits/s/Hz) [2]. It is even greater than that of DFT-OFDM without CP, $1B$ (bits/s/Hz), which is known as having the "maximum" bandwidth efficiency based on Nyquist rate sampling. This improvement is made possible by two important features of the CROW-OFDM subcarriers: the shift-orthogonality and overlapped partition of the frequency plane. The high bandwidth efficiency of the CROW-OFDM signal is further verified by simulations presented in chapter 6 where CROW-OFDM's application to wireless local area network (WLAN) is examined.

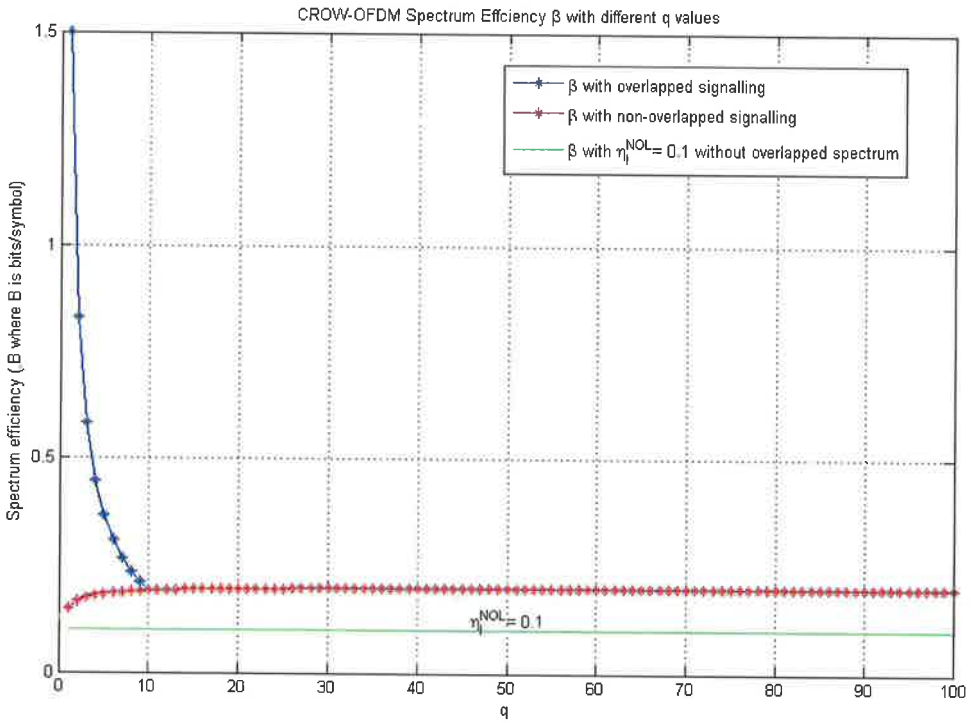

Figure 3.4. Bandwidth efficiency of CROW-OFDM with different q values

[2]Notice that the corresponding wavelet is the RROW with $q = 1$ for PAM modulation, because CROW with $q = 1$ is not shift orthogonal by integer 1.

3.6 CROW-OFDM Transceiver Design

3.6.1 Parallel-FB-structured Transceiver

The modulation and demodulation of the CROW-OFDM signal could also be directly implemented by parallel FBs as shown in Fig 3.2. The filters in the subchannels are scaled versions of one prototype filter constructed by sampling the wavelet function $\psi(t)$. At the reasonable cost of increased computational complexity compared to the tree-structured FBs, this parallel structure has the benefit of improved robustness against synchronisation error based on a novel demodulator design [91] and could be implemented efficiently via advanced DSP technology using parallel calculation. For very long filters (for wavelets with large q values), more efficient implementation is available via FFT-based fast convolution algorithms [65], [18].

3.6.2 Tree-structured Transceiver

Based on the tree-structured FWT synthesis and analysis FBs proposed in chapter 2, section 2.5, a general tree-structured modulator and demodulator structure for CROW-OFDM can be constructed as shown in Fig. 3.5 and Fig. 3.6. They are equivalent to the block diagram of CROW-OFDM transceiver based on parallel synthesis and analysis FBs as shown in Fig. 3.2 with $N = 4$. The input signals $\{c_{k,i},\ i = 0, \cdots, 3\}$ are complex input symbols. The function $\phi_+(t)$ serves as a complex lowpass filter and also represents the reconstruction of a signal from its wavelet coefficients. The transmitted signal $x(t)$ has to be a real signal and requires the $\Re[.]$ operation which gets the real part of a complex signal. The two FB solutions proposed in section 2.5.2 lead to different single-level synthesis and analysis FBs. The first solution requires complex scaling and wavelet filters while the second solution requires real filters and has exactly the same single-level synthesis/analysis FBs as shown in Fig. 2.11 and Fig. 2.12. Therefore the second solution has almost half of the computation complexity of the first solution, and is thus adopted in the transceiver design in simulations detailed in chapter 6.

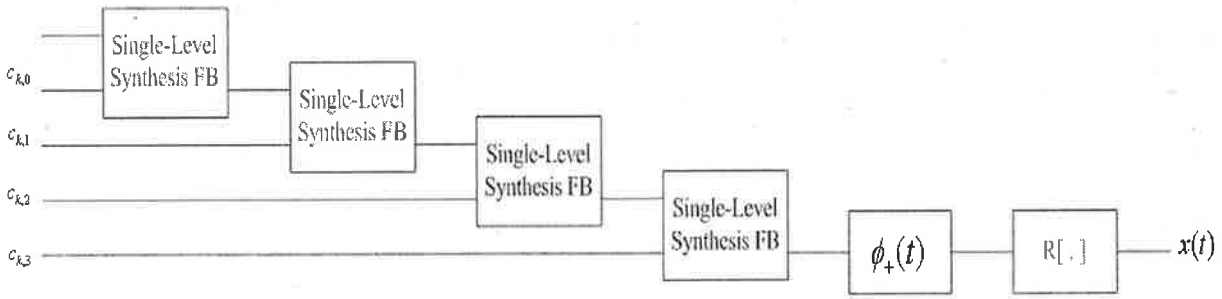

Figure 3.5. CROW-OFDM transmitter structure

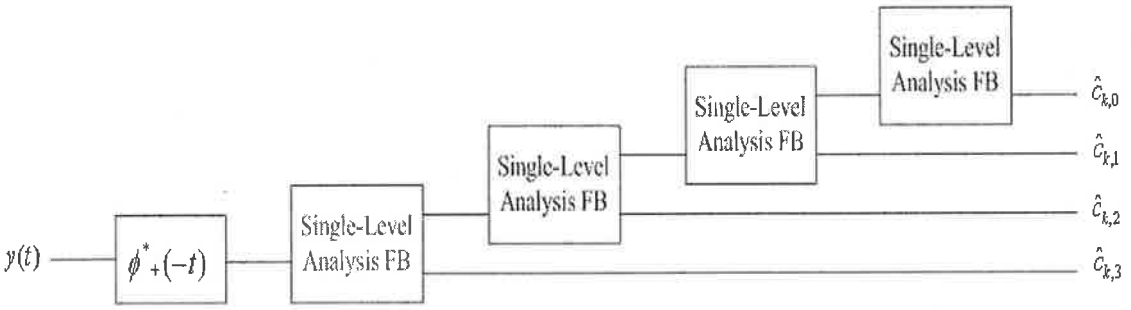

Figure 3.6. CROW-OFDM receiver structure

3.7 Conclusions

The main contributions of this chapter are summarised in the following together with some remarks.

1) A new OFDM scheme is proposed based on the CROWs proposed in chapter 2.

The orthogonality and good time-frequency localisation properties of the CROWs form the basis of the proposed CROW-OFDM scheme that is suitable for the application in time and frequency dispersive channels. For rectangular pulse based DFT-OFDM without CP, it has the maximum bandwidth efficiency of 1 symbol/Hz/s, but is very sensitive to frequency dispersion because of the strong sidelobes in the frequency domain. It is known that the introduction of a guard interval will improve the robustness against time dispersion, but has no effect against the frequency dispersion. In this case, the CROW-OFDM would definitely perform better with reduced ICI through frequency dispersive

channels due to its considerably lower frequency sidelobes.

2) The PSD and bandwidth efficiency of the CROW-OFDM scheme are analysed.

Formulae (3.7), (3.8) to calculate the PSD of the CROW-OFDM and the bandwidth efficiency of both non-overlapped and overlapped CROW-OFDM signals are derived. As a special case of CROW-OFDM with $q = 1$, significant improvement on bandwidth efficiency is achieved which reaches 1.5 times the 'maximum' value 1 symbol/Hz/s achieved by discrete Fourier transform (DFT) based OFDM without cyclic prefix (CP).

3) The CROW-OFDM transceiver is designed based on the tree-structured FWT FB proposed in chapter 2.

In addition to the CROW-OFDM transceiver based on the direct design with a parallel wavelet FB, a more computationally efficient transceiver structure is proposed based on the tree-structured FWT FB proposed in section 2.5, chapter 2.

A specific application scenario that could benefit from the Doppler robustness of the CROW-OFDM is the radio vehicular communication where the motion of communication platforms leads to the Doppler dispersion of the signal transmission. The performance of the CROW-OFDM in radio vehicular communication channels is further investigated in chapter 6 with mobile WLAN as a specific application scenario.

Chapter 4

CROW's Application to Underwater Acoustic Communications

4.1 Introduction

This chapter addresses the issue of Doppler dispersion in broadband UWA communications. A broadband Doppler compensation structure is proposed. The proposed structure avoids the explicit estimation of accumulated/instant Doppler scale, that is, the averaging process, by capturing the information carried by signals of all (or dominant) existing Doppler scales. The scale-compensated signal is then reconstructed via diversity combination. Based on wavelet pulse signalling in the transmitter, a transmultiplexer system model is presented to characterise the multiscale nature of the channel and the recovery of scale-compensated signal based on perfect reconstruction (PR) wavelet filter banks (FBs). The effective implementation of this structure generates new designs of wavelet shaping pulses with very fine scale resolution, which is the motivation of the work in chapter 2. The special class of wavelets, rational orthogonal wavelets with a scale dilation factor of $a^j : j \in \mathbb{Z}, 1 < a < 2$ as detailed in chapter 2, are adopted for this application. The design and performance characteristics of optimum receivers for this class of wavelet-based communication system are investigated. To be more specific, the presentation of the theory and properties is focused on for a general class of idealised multipath/Doppler channels.

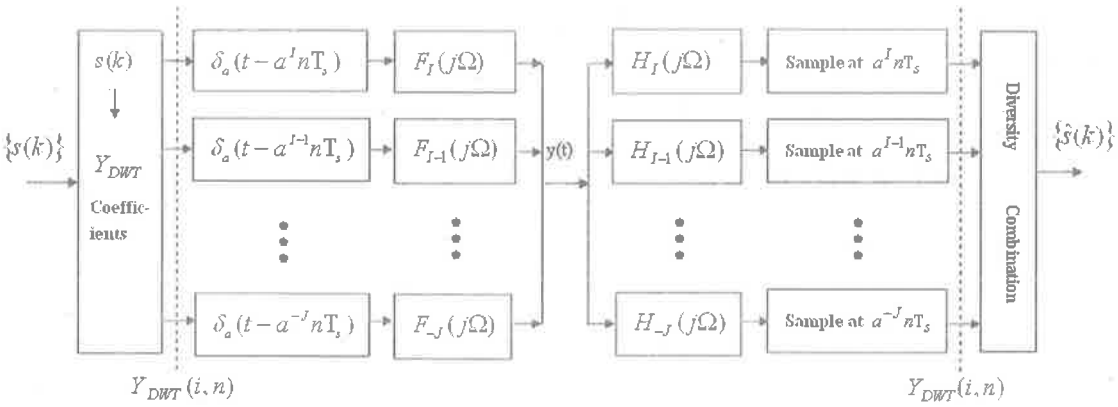

Figure 4.1. Transmultiplexer system model

The chapter is organised as follows. In section 4.2, we present the wavelet-based Doppler compensation structure. The design of optimum receivers is detailed in section 4.3. Section 4.4 presents the simulations that examine the system performance. Conclusions are made in section 4.5.

4.2 Rational Wavelet-based Transmultiplexer System Model for Doppler Compensation

In this section, we present the broadband Doppler compensation structure with rational wavelet pulse signalling using wavelets proposed in chapter 2.

The multipath/Doppler channel is modelled as [93]

$$y(t) = \sum_{\ell=1}^{L} \int_{-\infty}^{\infty} x(\eta_\ell t - \tau) h_\ell(\tau - \tau_\ell) d\tau + \xi(t), \tag{4.1}$$

where L is the number of dominant paths, η_ℓ and τ_ℓ are the Doppler scale and delay for the path indexed by ℓ, $h_\ell(t)$ is the impulse response of the channel for path ℓ which is defined to be independent of delay and Doppler effects, $x(t)$ and $y(t)$ are the input and output signals respectively, and $\xi(t)$ is the additive white Gaussian noise (AWGN). We assume that no significant ISI is present on each path, i.e., $h_\ell(t) = \rho_\ell \delta(t)$, where ρ_ℓ is the constant complex attenuation coefficient of path ℓ and $\delta(t)$, $t \in \mathbb{R}$ is the Dirac Delta

function. Notice that because of the scaling effect by η_ℓ, the time delay of each path observed in the receiver is $\frac{\tau_\ell}{\eta_\ell}$. We take account of this effect and to make the notation simple, τ_ℓ is used to denote the delay factor relative to the receiver and is redefined in subsequent equations as $\tau_\ell = \frac{\tau'_\ell}{\eta_\ell}$, where τ'_ℓ is the τ_ℓ in (4.1). The broadband channel model is then simplified to

$$y(t) = \sum_{\ell=1}^{L} \rho_\ell x(\eta_\ell(t - \tau_\ell)) + \xi(t). \tag{4.2}$$

With wavelet pulse signalling, the transmitted signal is expressed as

$$x(t) = \sum_{k} s(k)\ \psi(t - kT), \tag{4.3}$$

where $\psi(t)$ is the wavelet basis function as the shaping pulse and $\{s(k)\}, k \in \mathbb{Z}$ is the symbol sequence mapped as the amplitude of the shaping pulses. In this thesis, we assume $s(k) \in \{s_m;\ s_m \geq 0,\ m = 1, 2, \cdots, M\}$, where $\{s_m\}$ denotes the set of M real equally spaced amplitudes in accordance with the M-ary-PAM signalling scheme, and T is the symbol period. With the channel model in (4.2), the received signal can be expressed as

$$y(t) = \sum_{\ell=1}^{L} \rho_\ell \sum_{k} s(k)\ \psi(\eta_\ell(t - \tau_\ell) - kT) + \xi(t). \tag{4.4}$$

We assume[3] that the Doppler scales $\{\eta_\ell, 1 \leq \ell \leq L\}$ can be sufficiently approximated by the set $\{a^{-\alpha_\ell} : a^{-\alpha_\ell} = \eta_\ell, \alpha_\ell \in \mathbb{Z}, 1 \leq \ell \leq L\}$, where a is chosen as $1 < a < 2, a \in \mathbb{R}$, for a fine partition of the continuous scale coordinate. We also suppose $y(t)$ is to be sampled with a period of T_s in the receiver and the delay τ_ℓ can be uniquely decomposed into two parts, $\tau_\ell = a^{\alpha_\ell}\tau_\ell^{(1)}T_s + \tau_\ell^{(2)}T_s$, where $\tau_\ell^{(1)}$ and $\tau_\ell^{(2)}$ are integers, and $\tau_\ell^{(2)}T_s < a^{\alpha_\ell}T_s$. Equation (4.4) can then be rewritten as

$$\begin{aligned} y(t) &= \sum_{\ell=1}^{L} \rho_\ell \sum_{n} \sum_{k} s(k)\ \delta_{n-\tau_\ell^{(1)}-kT_n}\ \psi(a^{\alpha_\ell}t - nT_s) \\ &* \ \delta(t - \tau_\ell^{(2)}T_s) + \xi(t),\ n \in \mathbb{Z}, \end{aligned} \tag{4.5}$$

where $\delta_n, n \in \mathbb{Z}$ is the Kronecker Delta function, and $T_n = \left\lfloor \frac{T}{T_s} \right\rceil$ is the number of samples per symbol where the operation $\lfloor \cdot \rceil$ rounds $\frac{T}{T_s}$ to the nearest integer less than or equal to

[3]Note that the Doppler scale η_l can be defined by $\eta_l = 1 + \vartheta_l$, where ϑ is the Doppler shift to carrier frequency ratio [40]. ϑ is on the order of 10^{-7} or less for cellular communications [40], and could reach the order of 10^{-2} for vehicular UWA communications [70]. This general assumption holds mathematically since η_l can always be approximated by the power of a, if a is selected to be close enough to unity.

its value. The symbol $*$ represents the convolution operation. $\tau_\ell^{(2)}$ can be recognised as the synchronization error. The term of $\delta(t-\tau_\ell^{(2)}T_s)$ in (4.5) can therefore be removed to the receiver part and be mitigated via proper tracking techniques at the receiver. Letting $\psi_{kn}(t) = a^{-k/2}\,\psi(a^{-k}t - nT_s)$ and using the same notations as in [79], we can then write $y(t)$ as an inverse discrete wavelet transform (IDWT),

$$y(t) = \sum_{\ell=1}^{L}\sum_{n} Y_{DWT}(\alpha_\ell, n)\psi_{\alpha_\ell n}(t) + \xi(t), \tag{4.6}$$

where

$$Y_{DWT}(\alpha_\ell, n) = a^{\alpha_\ell/2}\rho_\ell \sum_{k} s(k)\delta_{n-\tau_\ell^{(1)}-kT_n)}, \tag{4.7}$$

which is a delayed, attenuated and periodically zero inserted version of the symbol sequence $\{s(k)\}$. The time delay $\tau_\ell^{(1)}$ is resolved together with the wavelet coefficients $Y_{DWT}(\alpha_\ell, n)$ by DWT.

The whole system can then be modelled as a transmultiplexer FB followed by diversity combination as shown in Fig. 4.1, where $F_k(j\Omega)$ and $H_k(j\Omega)$ are transfer functions of wavelet synthesis and analysis filters $f_k(t)$ and $h_k(t)$ respectively [79]. The filters $f_k(t)$ and $h_k(t)$ construct a PR wavelet FB and have the relation with the wavelet function $\psi(t)$ as

$$f(t) = \psi(t), \tag{4.8}$$
$$f_k(t) = a^{-k/2}f(a^{-k}t) = \psi_k(t), \tag{4.9}$$

and

$$f(t) = h^*(-t), \tag{4.10}$$
$$f_k(t) = h_k^*(-t). \tag{4.11}$$

The wavelet signalling and channel transmission are modelled as a wavelet synthesis process. The Doppler dispersion is resolved by wavelet analysis in the receiver with output wavelet coefficients as the multiple versions of the symbol sequence as derived in (4.7). Notice that this equivalent system model as shown in Fig. 4.1, resembles a wavelet-based modulation scheme known as fractal modulation [84], [13]. In other words, the transmission through the multipath/Doppler channel converts a simple PAM signal into a class

of rational-homogeneous signals [4] as in fractal modulation. Therefore, the receiver part resembles the demodulator of fractal modulation for an ideal AWGN channel. With a knowledge of maximum speed of moving transceivers (either approaching or departing from each other), we can always estimate the maximum Doppler spread and set the reference scales - maximum compression scale a^J and maximum dilation scale a^{-I} with $-J \leq \alpha_\ell \leq I,\ 1 < \ell < L,\ I, J \in \mathbb{Z}^+$. Therefore, a maximum of $(I + J + 1)$ channels is needed as shown in Fig. 4.1. The channel information-carried multiple symbol sequences can be recovered with perfect reconstruction transmultiplexer FBs.

For simplicity we discuss a PAM signalling scheme, therefore only the RROWs are involved. The extension to PSK signalling with the CROWs is straightforward. According to the definition in chapter 2, the RROWs are compactly supported in the frequency domain and therefore have infinite support in the time domain. However, by carefully defining the frequency spectrum they could have a sufficient decay in the time domain. This ensures their application as a shaping pulse. With respect to the desired properties of the pulse shaping wavelets for the Doppler compensation structure, there may be other wavelet candidates for this application. The exploration of more wavelet candidates can be treated as another issue which is beyond the scope of this thesis. It should also be noted at this point, that scale factors in practical UWA channels are typically quite close to unity, and as such the values of q used in this thesis are somewhat unrealistically small, however they permit the design process to be presented in a much simpler manner.

4.3 Optimum Receiver Design

In this section, we design the optimum receivers based on the PR wavelet analysis FBs and discuss the characteristics of the receivers that are optimal under the ML decision rule.

[4] The concept of rational-homogeneous signals is defined in the sense that they satisfy the rational similarity property with rational scale factor of $1 < a < 2$, in contrast to the dy-homogeneous [84] signals with dyadic self-similarity property.

4.3.1 Equivalence of the Doppler Compensation Structure with An L-th Order Diversity Communication System

As shown in equations (4.6) and (4.7) in section 4.2, with rational orthogonal wavelet pulse signalling, the received signal through the multipath/Doppler channel is a synthesised signal with input wavelet coefficients in certain wavelet subspaces as the delayed, attenuated and periodically zero inserted versions of the symbol sequence $\{s(k)\}$. Equivalently, the receiver is provided with the independently fading replicas of the same information-bearing signal. This coincides with the concept of diversity. Comparing with the existing diversity techniques, such as frequency diversity, time diversity and space diversity, the diversity provided by the multiscale nature of the multipath/Doppler channel and rational orthogonal wavelet signalling could be termed "scale diversity" in the sense that the same information is carried by multiple signals that are orthogonal in scale.

Assume there are L dominant paths. The frequency-selective fading multipath/Doppler channel is resolved into L flat fading channels with independent modulation of the same information for each channel. The signals transmitted over the multiple channels are given by

$$\begin{aligned} x_{\alpha_\ell}(t) &= \sum_k s(k)\ \psi(a^{-\alpha_\ell}t - kT) \\ &= a^{\alpha_\ell/2} \sum_k s(k)\ \psi_{\alpha_\ell}(t - a^{\alpha_\ell}kT). \end{aligned} \tag{4.12}$$

Notice that the same symbol sequence $\{s(k)\}$ is transmitted at different rates $a^{-\alpha_\ell}T$ over multiple channels.

In light of this further insight of the transmultiplexer system model, we see that the addressed wavelet-based Doppler compensation system is identical to an L-th order diversity communication system. Therefore the optimum receiver design and the performance characterisation are also identical to those of an L-th order diversity system.

4.3.2 Optimum Receiver Construction

We consider optimum receivers for a symbol-by-symbol detection based on the ML criterion. We first recall some facts on the optimum receiver design for a diversity system. Readers are referred to books on communication theory, e.g. [62] for more details. The

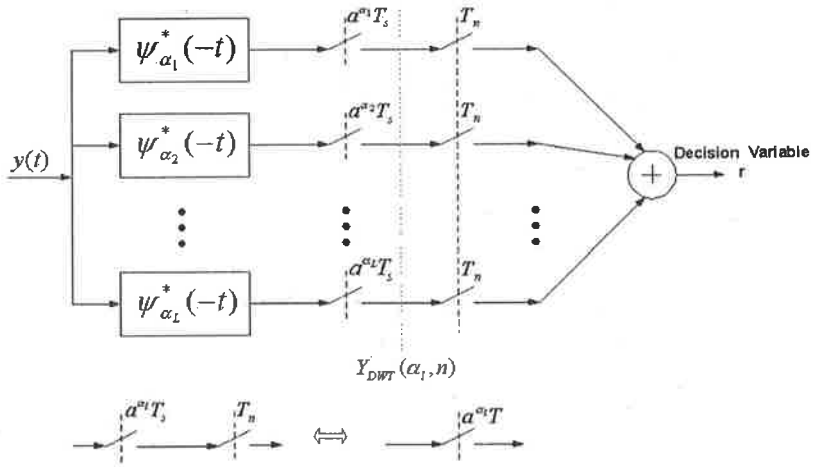

Figure 4.2. Type 1 receiver for M-PAM signal

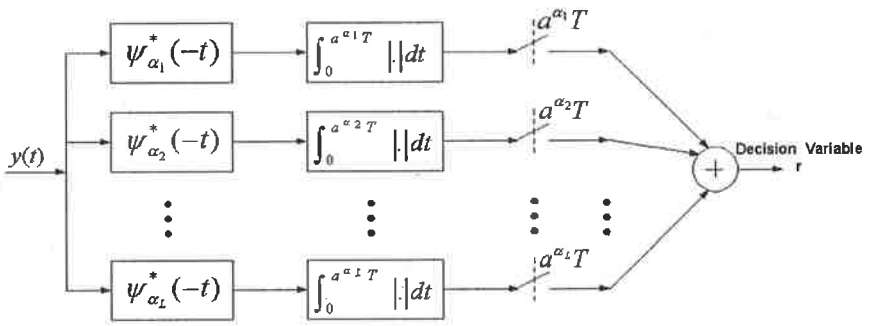

Figure 4.3. Type 2 receiver for M-PAM signal

notations in [62] are adopted in this section. We use a ML decision rule that is based on the maximisation of the likelihood function $P(\mathbf{r}|\mathbf{s}_m)$, $m = 1, 2, \cdots, M$, where $\mathbf{r}$ is the output observation vector of a correlation or matched filter demodulator and $\mathbf{s}_m$ are the M-ary signal points. It is equivalent to finding the signal $\mathbf{s}_m$ that maximises the correlation metrics:

$$\begin{aligned} C(\mathbf{r}, \mathbf{s}_m) &= 2 < \mathbf{r}, \mathbf{s}_m > - \|\mathbf{s}_m\|^2, \\ &= 2 \int_0^T r(t) s_m(t) dt - \varepsilon_m, \ m = 1, 2, \cdots, M \end{aligned} \tag{4.13}$$

where $r(t)$ is the received signal, $s_m(t)$ is the M-ary signal waveform and ε_m is the energy of the signal $s_m(t)$. For an L-th order diversity system, the optimum decision is made by

maximising the combined correlation metrics

$$CM_m = \sum_{n=1}^{L} C(\mathbf{r}^{(n)}, \mathbf{s}_m), \tag{4.14}$$

where $\mathbf{r}^{(n)}$ is the output observation vector of the n-th subchannel. Based on the correlation metrics $C(\mathbf{r}, \mathbf{s}_m)$, the optimum receiver can be realised by a correlation or matched filter demodulator followed by symbol detection via selecting the signal corresponding to the largest $C(\mathbf{r}, \mathbf{s}_m)$. Note that the vector $\mathbf{r}$ is reduced to a scalar r for PAM signalling [62].

Returning to the wavelet-based transmultiplexer system model, we see that the PR wavelet analysis FB actually plays the role of an optimum multichannel matched filter demodulator (also called a Rake receiver) for the transmitted signals $x_{\alpha_\ell}(t) = a^{\alpha_\ell/2} \sum_k s(k)\ \psi_{\alpha_\ell}(t - a^{\alpha_\ell} k T_a)$. The receiver can be regarded as a Rake-type receiver working not only in the time domain in the sense of resolving the multipath, but also in the scale domain in the sense of resolving the Doppler scales. The matched filters $h_k(t)$ are related to the wavelet basis functions $\psi(t)$ as

$$h_k(t) = \psi_k^*(-t). \tag{4.15}$$

Since the wavelet function $\psi(t)$ is real and symmetric as shown in section 2.2, we have $\psi^*(-t) = \psi(t)$ which is used to simplify the derivation of related formulae.

We then consider the construction of optimum receivers for M-ary PAM wavelet signalling. We see that the multipath/Doppler communication system is identical to an L-th order diversity system with independent M-ary PAM on the waveforms of $\{\psi_{\alpha_\ell}(t), 1 \leq \ell \leq L\}$ over L subchannels. With the PR property of the orthogonal wavelet FB, the optimum receiver can be constructed as shown in Fig. 4.2. The wavelet coefficients are recovered by a downsampler operating at the rate $a^{-k} n T_s$. The symbol sequence is then obtained by further downsampling with a sampling factor of T_n. The combined downsampling factor is $a^{-k} T$ as shown in Fig. 4.2. Although we use a maximum of $(I + J + 1)$ channels to capture the information of all possible Doppler scales, we only show the channels corresponding to the existing Doppler scales $\{a^{-\alpha_\ell}, 1 \leq \ell \leq L\}$ in the receiver.

Note that Fig. 4.1 illustrates the computation of DWT, not the discrete-time wavelet transform (DTWT) [79], thus the continuous-time sampling factor $a^{-k} n T_s$ is allowed for the implementation. For a discrete-time implementation of the receiver, we actually

use the truncated discrete-time approximation of the continuous-time wavelet analysis filters and apply a sampling factor according to the length of each analysis filter. For mathematical convenience, we continue to use the continuous-time wavelet filters in our formulae.

For M-ary PAM signalling, a single decision variable suffices and for the proposed optimum receiver shown in Fig. 4.2 the decision variable can be derived as

$$r = \sum_{\ell=1}^{L} (a^{\alpha_\ell/2} \rho_\ell s_m \gamma_0 + \xi_\ell), \tag{4.16}$$

where

$$\begin{aligned} \xi_\ell &= \int_0^{a^{-\alpha_\ell} T} \xi(\tau) \psi_{\alpha_\ell}^*(a^{-\alpha_\ell} T - \tau) d\tau \\ &= \xi_\ell(t)|_{t=a^{-\alpha_\ell} T} \\ &= \xi_\ell(a^{-\alpha_\ell} T), \end{aligned} \tag{4.17}$$

and

$$\begin{aligned} \gamma_0 &= \int_{-\infty}^{\infty} \psi_{\alpha_\ell}(\tau) \psi_{\alpha_\ell}(a^{-\alpha_\ell} T - \tau) d\tau \\ &= \int_{-\infty}^{\infty} \psi_{\alpha_\ell}^2(t) dt \\ &= \varepsilon_{\psi_{\alpha_\ell}}. \end{aligned} \tag{4.18}$$

The item $\varepsilon_{\psi_{\alpha_\ell}}$ is the energy of the wavelet basis ψ_{α_ℓ} and $\varepsilon_{\psi_{\alpha_\ell}} = 1$ for normalised wavelet basis functions. $\xi(t)$ is the AWGN and $\xi_\ell(t)$ is its projection onto the wavelet subspace spanned by $\{\psi_{\alpha_\ell n}(t), n \in \mathbb{Z}\}$.

One problem with this detection algorithm is that it works only with nearly perfect time synchronization. Although the delay factor $\tau_\ell^{(1)}$ is easily resolved from the shift of the output wavelet coefficients, the proposed receiver structure is very sensitive to the estimation of $\tau_\ell^{(2)}$ because of the time-variance of DWT. Furthermore, performance degradation is even worse when the signalling wavelet is a rational wavelet which is a passband signal and the outputs of the wavelet analysis FB (actually the autocorrelation function of $\psi_k(t)$) have severe fluctuations.

Another receiver structure with more robustness against the time synchronization error is shown in Fig. 4.3. It is based on the optimum envelope detection for signals with

random phases [62]. The output decision variable is given by

$$r = \sum_{\ell=1}^{L} (a^{\alpha_\ell/2} \, |\rho_\ell| \, |s_m| \, \mu_{\alpha_\ell} + \xi_\ell), \tag{4.19}$$

where

$$\begin{aligned} \xi_\ell &= \int_0^{a^{-\alpha_\ell}T} \left| \int_{-\infty}^{\infty} \xi(\tau) \psi_{\alpha_\ell}^*(t-\tau) d\tau \right| \, dt \\ &= \int_0^{a^{-\alpha_\ell}T} |\xi_\ell(t)| \, dt, \end{aligned} \tag{4.20}$$

and

$$\begin{aligned} \mu_{\alpha_\ell} &= \int_0^{a^{-\alpha_\ell}T} \left| \int_{-\infty}^{\infty} \psi_{\alpha_\ell}(\tau) \psi_{\alpha_\ell}(t-\tau) d\tau \right| \, dt \\ &= \int_0^{a^{-\alpha_\ell}T} \left| \phi_{\psi_{\alpha_\ell}\psi_{\alpha_\ell}}(t) \right| \, dt \\ &= a^{\alpha_\ell} \mu_0. \end{aligned} \tag{4.21}$$

The item $\phi_{\psi_{\alpha_\ell}\psi_{\alpha_\ell}}(t)$ is the autocorrelation function of $\psi_{\alpha_\ell}(t)$ and μ_0 is a constant related to the signalling wavelet $\psi(t)$ by

$$\mu_0 = \int_0^{a^{-\alpha_\ell}T} |\phi_{\psi\psi}(t)| \, dt. \tag{4.22}$$

We see that, compared with the type 1 receiver, the type 2 receiver is suboptimum in regard to the penalty on the output signal-to-noise ratio (SNR) as illustrated in the next section. The advantage achieved by this detection algorithm is that the requirement on time synchronization is much relaxed. We show in section 4.4 the performance of the above two receivers denoted as type 1 and type 2 receivers respectively, by Monte Carlo simulations. The theoretical derivation of probability of error and diversity gain is given in section 4.3.3.

4.3.3 Evaluation of Probability of Error and Diversity Gain

To simplify the expression of the signal components out of the FBs, we multiply by a factor of $a^{-\alpha_\ell/2}$ for the filter channel of the type 1 receiver which has the scale of α_ℓ, and by a factor of $a^{-3\alpha_\ell/2}$ for the certain channel of the type 2 receiver in order to cancel the parameters induced by the different energy of signal waveforms with different scales as

shown in (4.16) and (4.19). For simplicity, this multiplication is not shown in the receiver block diagrams. The signal points s_m, $m = 1, 2, \cdots, M$ are defined by

$$s_m = A_m \sqrt{\varepsilon_g}, \tag{4.23}$$

for both receivers, where ε_g is the energy of the basic signal pulse $g(t) = \sqrt{\varepsilon_g}\psi(t)$, $A_m = 2md$, $m = 1, 2, \cdots, M$ and $2d$ is the distance between adjacent signal amplitudes[5] .

For the type 1 receiver, the probability of error can be derived as (see Appendix B.1)

$$P_M = \frac{2(M-1)}{M} Q\left(\sqrt{\frac{2d^2\varepsilon_g(\sum_{\ell=1}^{L}\rho_\ell)^2}{N_0\sum_{\ell=1}^{L}a^{-\alpha_\ell}}}\right), \tag{4.24}$$

where the $Q(.)$ function is defined by

$$Q(x) = \frac{1}{\sqrt{2\pi}}\int_x^\infty e^{-t^2/2}dt, \; x \leq 0 \tag{4.25}$$

This error can be expressed in a simpler form in terms of the average received SNR or output SNR. Assuming $\alpha_1 < \alpha_2 < \cdots < \alpha_L$, the total symbol rate is equal to the lowest symbol rate through the subchannel with Doppler scaling factor of $a^{-\alpha_L}$ and filter length N_L. Based on this lowest symbol rate, we define the average symbol energy of the multipath signal without noise as ε_{av} [62] and

$$\begin{aligned}
\varepsilon_{av} &= \frac{1}{M}\sum_{m=1}^{M}\varepsilon_m \\
&= \frac{d^2\varepsilon_g a^{\alpha_L}\sum_{\ell=1}^{L}\rho_\ell^2}{M}\sum_{m=1}^{M}(2m)^2 \\
&= \frac{2}{3}(2M^2+3M+1)d^2\varepsilon_g a^{\alpha_L}\sum_{\ell=1}^{L}\rho_\ell^2.
\end{aligned} \tag{4.26}$$

From equation (4.26), we note that

$$d^2\varepsilon_g = \frac{3\varepsilon_{av}}{2(2M^2+3M+1)a^{\alpha_L}\sum_{\ell=1}^{L}\rho_\ell^2}. \tag{4.27}$$

[5]Notice that the type 2 receiver requires positive PAM signalling because of the $|.|$ operation involved in the formula of decision variable (4.19). Although the type 1 receiver allows standard PAM scheme with $A_m = (2m-1-M)d$, $m = 1, 2, \cdots, M$, positive PAM is adopted for both receivers in the derivation of formulae for a comparison of the system performance. Under the same M and d values, the standard PAM signal has lower average symbol energy, which leads to improved power efficiency, comparing to the positive PAM signal. The probability of error for the type 1 receiver with standard PAM can be obtained conveniently by modifying the formula of average symbol energy in (4.26).

By substituting (4.27) for the $d^2\varepsilon_g$ in (B.9), the average probability of a symbol error in terms of the average power is given as

$$P_M = \frac{2(M-1)}{M} Q\left(\sqrt{\frac{3\gamma_s \lambda}{(2M^2+3M+1)}}\right), \tag{4.28}$$

where $\gamma_s = \varepsilon_{av}/N_0$ is defined as the average received SNR per symbol and λ is a parameter decided by the multipath attenuation factors and the resolved Doppler scales,

$$\lambda = \frac{(\sum_{\ell=1}^{L} \rho_\ell)^2}{a^{\alpha_L} \sum_{\ell=1}^{L} \rho_\ell^2 \sum_{\ell=1}^{L} a^{-\alpha_\ell}}. \tag{4.29}$$

The output SNR obtained by the designed receiver, $\gamma_{s,o}$ is

$$\gamma_{s,o} = \frac{4(2M^2+3M+1)d^2\varepsilon_g(\sum_{\ell=1}^{L} \rho_\ell)^2}{3N_0 \sum_{\ell=1}^{L} a^{-\alpha_\ell}}. \tag{4.30}$$

The probability of error can be expressed by $\gamma_{s,o}$ as

$$P_M = \frac{2(M-1)}{M} Q\left(\sqrt{\frac{3\gamma_{s,o}}{2(2M^2+3M+1)}}\right). \tag{4.31}$$

The diversity gain obtained with non-coherent combining can be expressed as

$$DG = 10\log \frac{a^{-\alpha_\ell}(\sum_{\ell=1}^{L} \rho_\ell)^2}{\rho_\ell^2 \sum_{\ell=1}^{L} a^{-\alpha_\ell}} \tag{4.32}$$

For the type 2 receiver, the probability of error is derived as (see Appendix B.1)

$$P_M = \frac{2(M-1)}{M} Q\left(\sqrt{\frac{2d^2\varepsilon_g(\sum_{\ell=1}^{L} |\rho_\ell|)^2\mu_0^2}{N_0 \sum_{\ell=1}^{L} a^{-3\alpha_\ell} N_\ell}}\right). \tag{4.33}$$

The derivation of P_M in terms of the γ_s and $\gamma_{s,o}$ is similar to the one of the type 1 receiver and is omitted here. There is a performance loss for the type 2 receiver arising from the summation of noise samples which is evaluated by

$$P_{loss} = 10\log_{10}\left(\frac{(\sum_{\ell=1}^{L} \rho_\ell)^2 \sum_{\ell=1}^{L} a^{-3\alpha_\ell} N_\ell}{\mu_0^2(\sum_{\ell=1}^{L} |\rho_\ell|)^2 \sum_{\ell=1}^{L} a^{-\alpha_\ell}}\right) \ (dB). \tag{4.34}$$

Given the inequality that $(\sum_{\ell=1}^{L} \rho_\ell)^2 \leq (\sum_{\ell=1}^{L} |\rho_\ell|)^2$, the P_{loss} can be bounded by

$$P_{loss} \leq 10\log_{10}\left(\frac{\sum_{\ell=1}^{L} a^{-3\alpha_\ell} N_\ell}{\mu_0^2 \sum_{\ell=1}^{L} a^{-\alpha_\ell}}\right) \ (dB), \tag{4.35}$$

which is independent of the channel attenuation factors.

For comparison, the theoretical probability of error for type 1 and type 2 receivers is calculated using the parameter setting in the simulation and is plotted in Fig. 4.12 and Fig. 4.13 together with the simulation results.

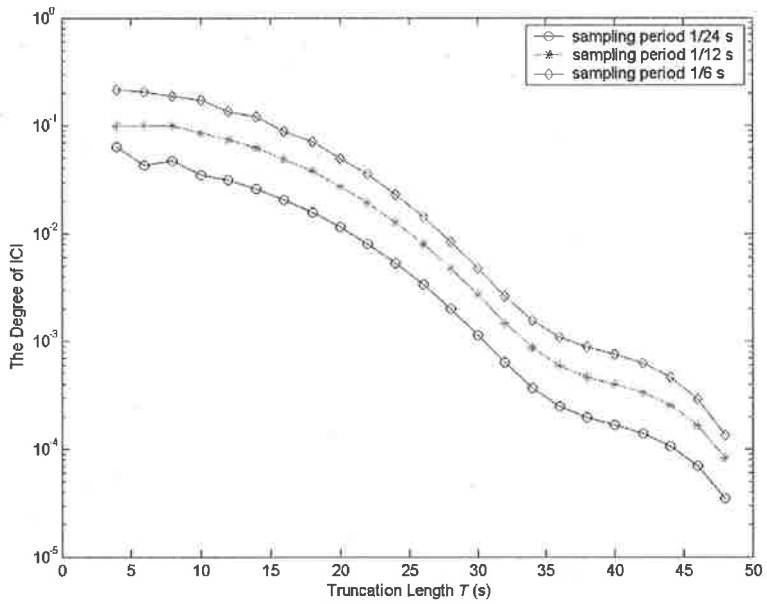

Figure 4.4. The degree of ICI versus truncation length T for 3-channel model

4.4 Simulation Results

In this section, we present the simulation results addressing the following issues:

- System discretization
- Selection of wavelet scale factors
- System sensitivity to the time synchronisation error
- BER performance versus SNR

4.4.1 System Discretisation

For a discrete-time implementation of the receiver, we use a discrete-time approximation of the wavelet basis functions as the analysis filters. In addition, since the rational orthogonal wavelets have infinite support in the time domain, the signalling wavelet has to

be truncated. There is a tradeoff among the symbol rate, system complexity and approximation error in accordance with the sampling rate and the truncation length. For two systems with the same sampling rate and non-overlapped signalling, the one with a longer truncation length has a better system performance since the frequency spectrum of the wavelet basis functions is better retained, although it has a longer filter length and slower symbol rate compared to the one with a shorter truncation length. The computation complexity is reduced with a shorter truncation length by applying shorter filters in the receiver, however more frequency sidelobes are thus induced and result in an increase in the ICI.

Explicit formulae can be derived to show the relations between these relevant factors. Suppose the signalling pulse is a rational orthogonal wavelet $\psi(t)$ with dilation factor of $a = \frac{q+1}{q}$ which is truncated at $[t_0, t_1]$ with $t_1 - t_0 = T$. With non-overlapped signalling, the symbol rate is $f_I = \frac{1}{T}$. From the definition of the rational orthogonal wavelet, we know that the bandwidth of the wavelet basis function is $BW_{\psi(t)} = [\omega_1, \omega_3] = 2\pi$ where $\omega_1 = (q - \frac{q}{2q+1})\pi$ and $\omega_3 = a^2\omega_1$ as shown in (2.13). Assume the maximum Doppler compression scale is $\hat{a}^J$, where $\hat{a}$ is the estimated Doppler dilation factor. It is worth noting that although we assume $a = \hat{a}$ in the derivation of the transmultiplexer structure in section 4.2, we can actually select a wavelet with dilation factor a smaller than the Doppler dilation factor, $a < \hat{a}$, for a finer resolution. More details about the selection of wavelet dilation factors are given in section 4.4.2.

According to the Nyquist sampling principle, to avoid spectrum distortion, the sample period T_s for the signalling pulse has to satisfy

$$T_s = 1/f_s \leq \frac{\pi}{\hat{a}^J a^2 \omega_1}. \tag{4.36}$$

The matched filter in the receiver for the scale factor of $\hat{a}^{\alpha_\ell}$ will have length N_ℓ that

$$N_\ell = \left\lfloor \hat{a}^{\alpha_\ell} \frac{T}{T_s} \right\rfloor. \tag{4.37}$$

By substituting T_s of (4.37) with (4.36), we have

$$N_\ell \geq \left\lfloor \frac{1}{\pi} \hat{a}^{(\alpha_\ell + J)} T a^2 \omega_1 \right\rfloor. \tag{4.38}$$

If we keep the same truncated pulse shape and change the symbol rate by letting $f_I' = C f_I$ where $C \in \mathbb{R}$ is a constant, the signalling pulse is actually the dilated wavelet $\psi(Ct)$ with

a spectrum bandwidth of $BW_{\psi(Ct)} = [C\omega_1, C\omega_3] = 2\pi C$. The sample period T_s' has to satisfy

$$T_s' \leq \frac{\pi}{C\hat{a}^J a^2 \omega_1}. \tag{4.39}$$

Suppose we have a 4-PAM signalling system with Doppler scales valued at $(\frac{3}{2})^{-1}$, $(\frac{3}{2})^{-2}$ and $(\frac{3}{2})^{-3}$. For simplicity, the attenuation and delay factors are set to be equal for the subchannels in the simulations through the whole section. The signalling wavelet is the 3/2 wavelet. Therefore, we have $\alpha_1 = 1$, $\alpha_2 = 2$, $\alpha_3 = 3$, $a = \hat{a} = \frac{3}{2}$ and $a^2\omega_1 = \frac{8}{5}\pi$. For this simulation case, since we know that the Doppler scales are all dilation scales ($\alpha_l > 0$), we can pick the smallest dilation scale $(\frac{3}{2})^{-1}$ to substitute for the parameter $\hat{a}^J$ in (4.36). The sampling period T_s can then be selected based on the formula (4.36) (in this case, $T_s \leq \frac{5}{12}$). Given a truncation length of T and the desired symbol rate f_I', we can obtain the filter length and the practical sampling rate in the receiver by using the formulae (4.37) and (4.39).

Based on the above 4-PAM signalling system, we examine the impact of discrete-time approximation error that results in the loss of orthogonality (ICI) with the PR transmultiplexer structure. Zero channel noise is assumed. Fig. 4.4 shows the degree of ICI versus the truncation length T. The impact of the sampling rate on the ICI is also shown in Fig. 4.4. The degree of ICI is evaluated by calculating the normalised standard deviation of the filter output with respect to the ideal output without ICI. In contrast to the one-channel case where the degree of ICI simply represents the effect of truncation and sampling and is calculated to be on the order of 10^{-14} or less, Fig. 4.4 indicates significant performance loss for the multichannel case because of the ICI. However, by minimizing the discretisation error, the ICI tends to decrease and approach the PR condition as derived in the continuous-time context.

It is worth noting that the system discretisation has to be considered more carefully for the Doppler compensation system with PSK/QAM signalling where phase information is needed and is affected by the length and symmetry of the wavelet filters. In addition, the use of complex rational orthogonal wavelet (CROW) featuring both amplitude and phase information is required. Further investigation on more power- and frequency-efficient UWA Doppler compensation structures with CROW-based PSK/QAM signalling and the related issues is ongoing and is to be detailed in [89].

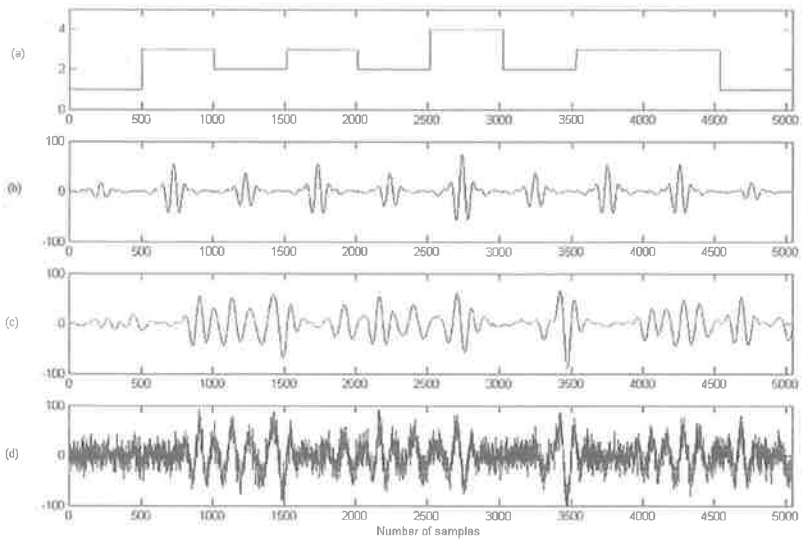

Figure 4.5. Meyer wavelet based modulation (a) Input symbol sequence (b) Source signal with Meyer pulse shaping (c) Synthesised multiscale signal with 3 paths scaled at $(\frac{5}{4})^{-1}$, $(\frac{5}{4})^{-2}$ and $(\frac{5}{4})^{-3}$ (d) Synthesised multiscale signal with 0dB AWGN

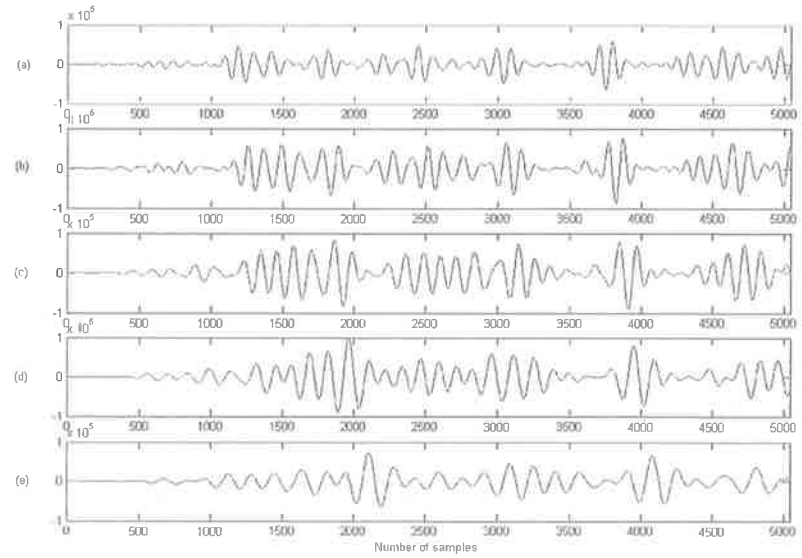

Figure 4.6. Meyer wavelet based demodulation (a)-(e) Outputs of the analysis filters prescaled at $(\frac{5}{4})^{0}$, $(\frac{5}{4})^{-1}$, $(\frac{5}{4})^{-2}$, $(\frac{5}{4})^{-3}$ and $(\frac{5}{4})^{-4}$ respectively

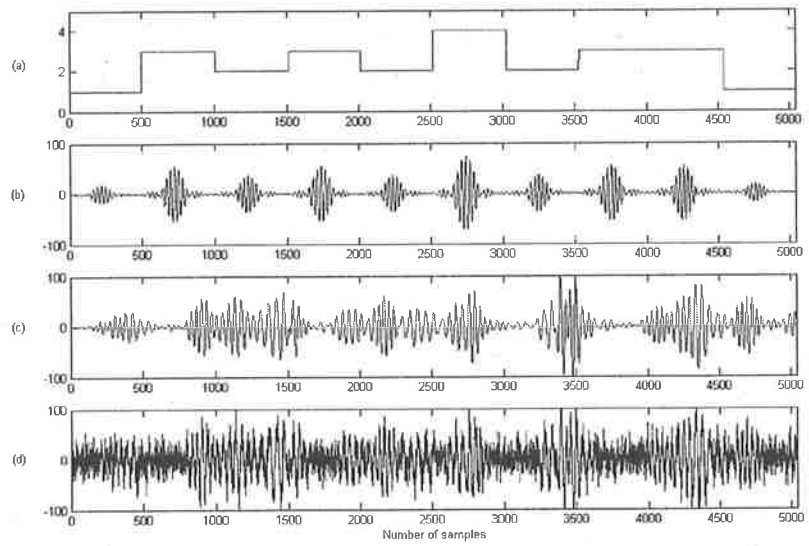

Figure 4.7. Rational $5/4$ wavelet based modulation (a) Input symbol sequence (b) Source signal with rational $\frac{5}{4}$ wavelet pulse shaping (c) Synthesised multiscale signal with 3 paths scaled at $(\frac{5}{4})^{-1}$, $(\frac{5}{4})^{-2}$ and $(\frac{5}{4})^{-3}$ (d) Synthesised multiscale signal with 0dB AWGN

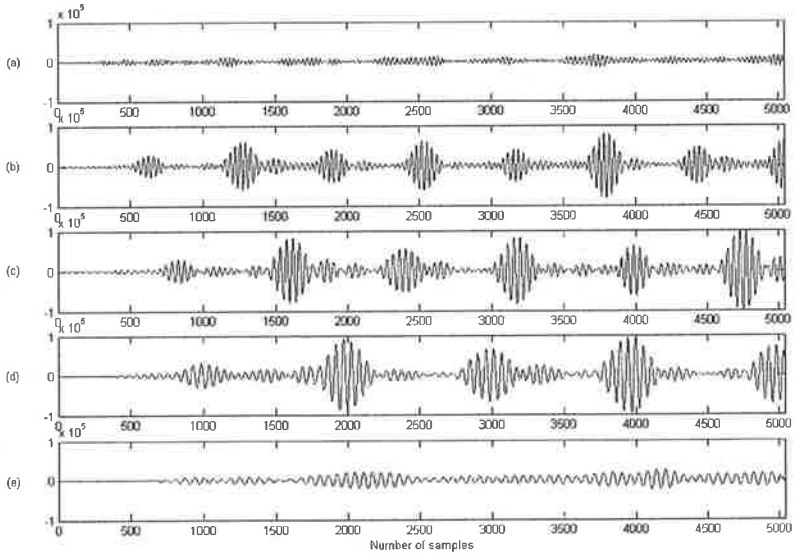

Figure 4.8. Rational $5/4$ wavelet based demodulation (a)-(e) Outputs of the analysis filters prescaled at $(\frac{5}{4})^{0}$, $(\frac{5}{4})^{-1}$, $(\frac{5}{4})^{-2}$, $(\frac{5}{4})^{-3}$ and $(\frac{5}{4})^{-4}$ respectively

4.4.2 Selection of Wavelet Scale Factors

As shown in the formulae of the two decision variables, we demonstrate that the ICI is cancelled due to the orthogonality of the rational wavelet. This is the advantage we obtain by applying the rational orthogonal wavelet as the shaping pulse. This ICI cancellation effect can also be explained from a frequency domain point of view. The signalling with wavelets avoids the relatively large sidelobes which, for example, is a limitation of the DFT-based modulator/demodulator in an OFDM system. The fine scale orthogonality of the rational orthogonal wavelets further ensures the independence of the two signals scaled by close Doppler scales when the spectrum of the two signals is sufficiently apart or orthogonally overlapped.

To illustrate the benefit of using rational orthogonal wavelets instead of a traditional dyadic wavelet as the shaping pulse, we compare the ICI cancellation effect by using dyadic Meyer wavelet signalling and 5/4 rational wavelet signalling respectively. Assuming 3 existing Doppler scales, $(\frac{5}{4})^{-1}$, $(\frac{5}{4})^{-2}$ and $(\frac{5}{4})^{-3}$, the different ICI cancellation performances are illustrated in Fig. 4.5, Fig. 4.6, Fig. 4.7 and Fig. 4.8 by plotting the signal waveforms at different stages of the system. The two simulated systems have the same symbol rate and sample rate. Fig. 4.5 and Fig. 4.7 show the signals at the synthesis part of the transmultiplexer. Fig. 4.6 and Fig. 4.8 show the outputs of the analysis FB before multirate sampling and diversity combination (see Fig. 4.1).

From Fig. 4.8 we see that with 5/4 rational wavelet signalling, the 3 Doppler scales can be explicitly resolved with 0 dB noise as shown in (b),(c) and (d), where the information of the symbol sequence is carried by the magnitude of these output pulse sequences. The ICI has been mitigated as shown in (a) and (e). In contrast, with dyadic Meyer wavelet signalling, the 3 scales can not be effectively resolved because of the poor ICI cancellation as shown in Fig. 4.6. Note that the cancellation of ISI caused by the multipath delay shares the same figure of merit with the ICI cancellation based on the Rake-type receiver structure in both time and scale domain as discussed in section 4.3.2.

Theoretically, with a Doppler scale dilation factor of $\hat{a}$, a rational orthogonal wavelet with dilation factor of $a = \hat{a}$ suffices due to the scale orthogonality property. However, since the rational orthogonal wavelets have infinite support in the time domain, in the practical implementation a discrete-time approximation is applied which causes the loss of orthogonality in certain degrees as shown in Fig. 4.4. The use of a rational orthogonal

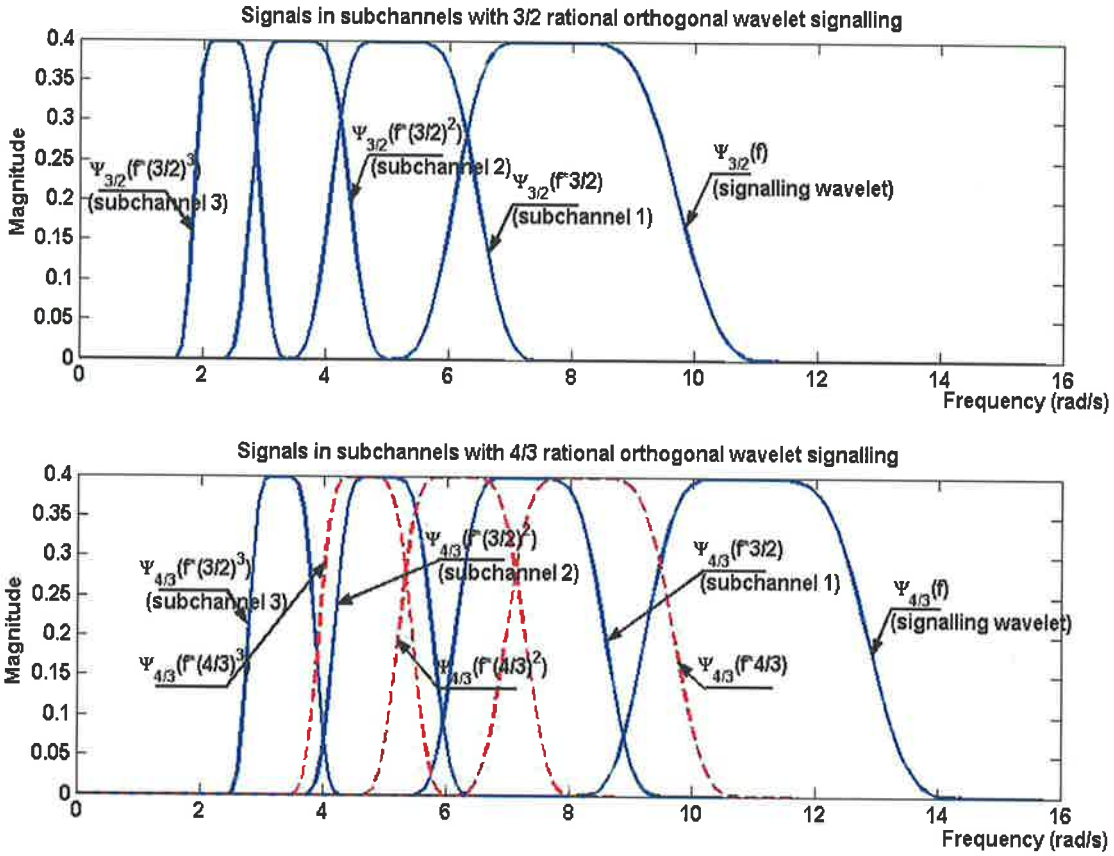

Figure 4.9. Frequency spectrum chracteristics with 3/2 and 4/3 rational orthogonal wavelet signalling. (The dashed lines show the orthogonal 4/3 wavelet functions for a comparison with the signals in the subchannels.)

wavelet with a dilation factor a smaller than $\hat{a}$ creates a sort of redundancy as illustrated in Fig. 4.9 and therefore leads to better ICI cancellation. Fig. 4.9 shows the multipath signal spectrum with 3/2 and 4/3 wavelet signalling respectively when the channel has 3 Doppler scales valued at $(\frac{3}{2})^{-1}$, $(\frac{3}{2})^{-2}$ and $(\frac{3}{2})^{-3}$. Fig. 4.10 gives a comparison of ICI cancellation for this channel with finer signalling wavelets (4/3, 5/4 and 6/5 wavelets) as well as 3/2 wavelet, all with fixed sampling period of 1/6 and therefore with the same filter length for certain truncation length T. We see that the performance of ICI cancellation is improved significantly with finer wavelet scales. The mismatch of the Doppler and wavelet dilation scales, however, may lead to the non-monotonicity of the performance, which indicates that the ICI may not necessarily be mitigated by the small

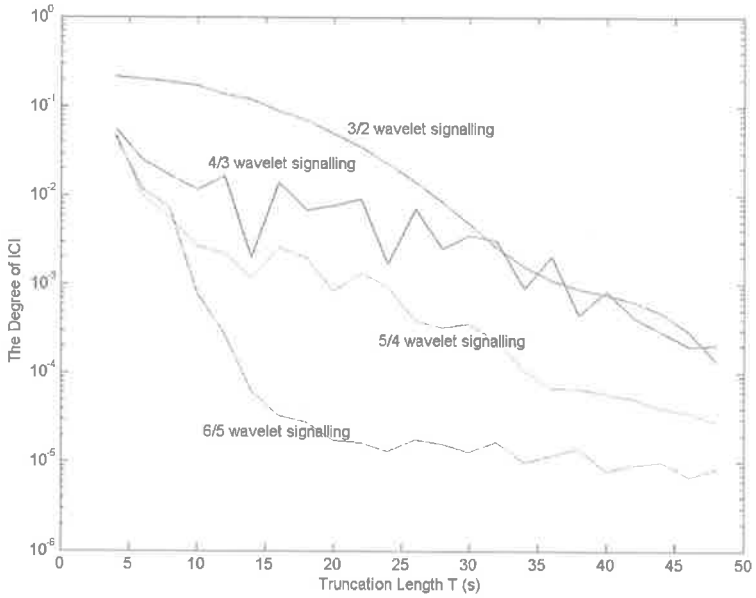

Figure 4.10. The degree of ICI versus truncation length T with wavelet dilation factors valued at 3/2, 4/3, 5/4 and 6/5 respectively.

amount of increase of the truncation length T. Again, there is a tradeoff between the wavelet resolution, the symbol rate, the filter length and the available channel bandwidth which can be formulated as follows.

Assuming a bandlimited channel with the channel bandwidth $BW = [f_{Lo}, f_{Hi}]$ and Doppler scales $\{\hat{a}^{-\alpha_\ell} : -J \leq -\alpha_\ell \leq I, 1 \leq \ell \leq L\}$, we have

$$2\pi f_{Lo} \leq C\hat{a}^{-I}\omega_1 < C\hat{a}^{J}\omega_3 \leq 2\pi f_{Hi}. \tag{4.40}$$

With the relation in (2.13), we see that for the existence of a solution for the proposed wavelet signalling scheme, the channel has to meet the condition that

$$f_{Hi} > \left(\frac{q+1}{q}\right)^2 f_{Lo}\hat{a}^{(I+J)}. \tag{4.41}$$

The formula (4.40) can be further simplified as

$$2\pi f_{Lo}\hat{a}^{I} \leq C\omega_1 \leq 2\pi f_{Hi}a^{-2}\hat{a}^{-J}. \tag{4.42}$$

This constraint on ω_1 indicates that the signalling wavelet has to be carefully chosen not only to achieve a sufficient scale resolution but also to satisfy the channel bandwidth

requirement. Based on a selected signalling wavelet, the maximum symbol rate is derived from (4.42) as

$$f'_{I,max} = \frac{2\pi f_{Hi}}{a^2\omega_1 \hat{a}^J T}, \tag{4.43}$$

which is restricted by the spectrum characteristics of the selected signalling wavelet ($a^2\omega_1$) and the truncation length T.

In general, being aware of the tradeoff between these related system parameters, we have a full control of the system performance by selecting the signalling wavelet (parameter a) and discretization accuracy (parameters T_s and T) to meet specific system requirements.

4.4.3 System Sensitivity to the Time Synchronisation Error

We simulate a 4-PAM signalling system with Doppler scales valued at $(\frac{3}{2})^{-1}$, $(\frac{3}{2})^{-2}$ and $(\frac{3}{2})^{-3}$. The rational orthogonal wavelet with dilation factors of $\frac{4}{3}$ is employed as the signalling pulses in the simulation. The matched FB is constructed by pre-scaling the signalling wavelet according to the estimated Doppler dilation factor which is $\frac{3}{2}$ in the simulation. An extension to Doppler scale dilation factors finer than $\frac{3}{2}$ is straightforward with rational orthogonal signalling wavelets of finer scale dilation factors and longer analysis and synthesis filters. A randomly generated 100,000 symbols are used to test the performance of the proposed receiver structures. Notice that for the limited number of the symbols, the bit error rate (BER) is evaluated to be zero if its value is sufficiently small, which is shown in the subsequent figures on the BER performance.

We compare the sensitivity of the two receivers to the time synchronisation error which is illustrated in Fig. 4.11. Zero channel noise is assumed. The BER is evaluated as a function of synchronisation error. Assuming a coarse synchronisation is conducted at the input of the receiver, we focus on the synchronisation implemented in each subchannel. The synchronisation error is denoted as the percentage of maximum timing jitter error out of the symbol rate in each subchannel and we assume the same error percentage for all subchannels. To exclude the effect of noise on the receiver performance, we set zero AWGN in the analysis. The timing jitter error percentage has a range of 0 to 50% with a step of 0.5%. For certain timing jitter error percentage, e.g., 30%, the timing error for each symbol is uniformly distributed within 30% of the symbol period.

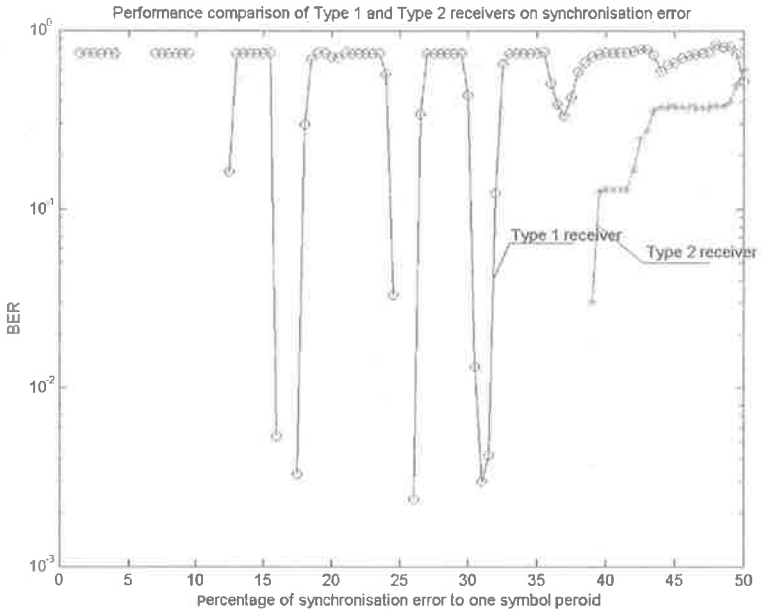

Figure 4.11. Performance of two receivers with different synchronisation errors with 4/3 wavelet signalling.

As shown in Fig. 4.11, the type 1 receiver is very sensitive to the synchronisation error and can only work with a time error less than 1%. Although good BER shows at certain intervals when the time error is larger than 1%, the receiver becomes unstable because of the big fluctuation of the BER performance. A strict time synchronisation process is therefore essential for this type of receiver. In contrast, the type 2 receiver shows good adaptation to the synchronisation error and works with a time error as large as 40%. The complexity of the receiver structure is significantly reduced with a simple synchronisation design (such as the signal energy detection).

4.4.4 BER Performance Versus SNR

The BER performance of the two types of receivers with different SNR is illustrated in Fig. 4.12 and Fig. 4.13. For comparison, the SNR performance with different synchronisation errors with timing error percentages of 0, 10%, 20%, 30% and 40%, is plotted in the same figure. The SNR is shown as the measured received SNR γ_m which has the relation with γ_s (defined in section 4.3.3) as $\gamma_m = \frac{\varepsilon_{av}}{N_0 N_L} = \frac{\gamma_s}{N_L}$. In Fig. 4.12, the type 2 receiver

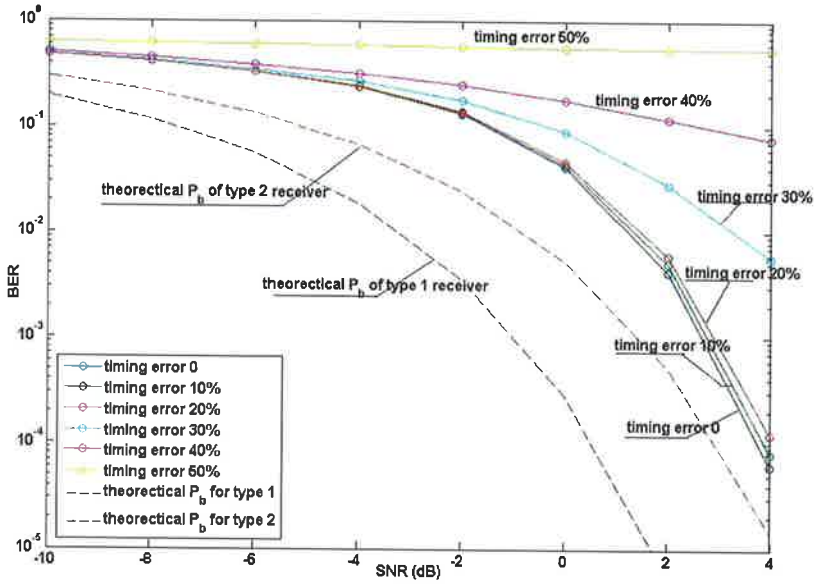

Figure 4.12. Performance of type 2 receiver at different SNRs and synchronisation errors with 4/3 wavelet signalling

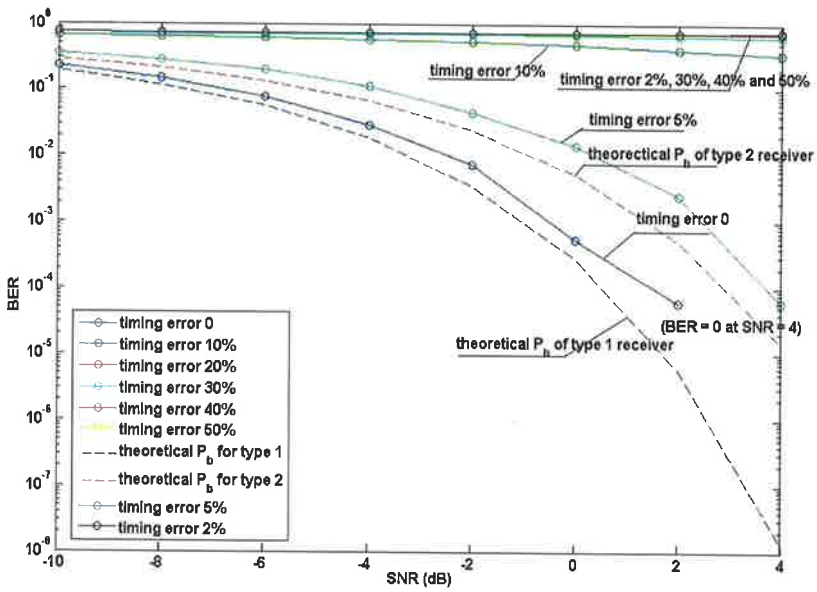

Figure 4.13. Performance of type 1 receiver at different SNRs and synchronisation errors with 4/3 wavelet signalling

shows good anti-noise capability and remains stable when the timing error is less than 40%. Fig. 4.13 shows that for the type 1 receiver the system performance is dominated by the timing error. Moreover, the BER plots with timing error of 2% and 5% indicate the fluctuation of the system performance that is in accordance with the results shown in Fig. 4.11. On the other hand, with a perfect time synchronisation, the BER of the type 2 receiver is higher than that of the type 1 receiver. This fact can be deduced from the computation of the two different decision variables. For the type 2 receiver, the noise item is enhanced comparing to the type 1 receiver since an integration process on $\xi_\ell(t)$ is involved. For both receivers, the simulated system performance is degraded compared with the theoretical derivation. This is because of the loss of orthogonality caused by the discrete-time approximation as shown in section 4.4.1.

4.5 Conclusions

The main contributions of this chapter are summarised in the following together with some remarks.

1) A transmultiplexer system model is proposed based on wavelet pulse signaling in the transmitter to characterise a multipath/Doppler channel and the recovery of Doppler compensated signal based on perfect reconstruction (PR) wavelet filter banks (FBs).

The proposed transmultiplexer structure for broadband Doppler compensation avoids the explicit estimation of accumulated/instant Doppler scale, that is, the averaging process, by capturing the information carried by signals of all (or dominant) existing Doppler scales. The effective implementation of this structure is based on a special class of wavelets, rational orthogonal wavelets with a scale dilation factor of $a^j : j \in \mathbb{Z}, 1 < a < 2$ proposed in chapter 2. Comparing with the existing Doppler compensation methods, the proposed broadband Doppler compensation structure leads to less residual Doppler due to the resolution of the multi-scale nature of the multipath/Doppler channel.

2) It is demonstrated in this chapter that the transmultiplexer structure for

broadband Doppler compensation is equivalent to an L-th order diversity system, which forms the basis of the optimum receiver design.

A further insight of the transmultiplexer system model reveals that the addressed wavelet-based Doppler compensation system is identical to an L-th order tranmission diversity communication system. This equivalence facilitates the optimum receiver design and the performance characterisation which are also identical to those of an L-th order diversity system.

3) Optimum receivers are designed for the proposed system structure based on the maximum likelihood (ML) criterion.

Optimum receivers for wavelet-based PAM signalling are designed under the ML decision criterion for diversity combination and symbol detection. For simplicity, we adopt RROWs as a special case of the CROWs to form the PAM signalling scheme, while the extension to the PSK modulation scheme based on the CROWs is straightforward. Two types of receivers are designed. Compared with the type 1 receiver which is based on the traditional optimal correlation/matched filtering demodulators, the type 2 receiver with modified demodulation structure is superior with its robustness against severe time synchronisation error.

4) Theoretical derivation of the probability of error for the two receivers is given together with supporting Monte Carlo simulations.

Taking advantage of the properties of rational orthogonal wavelets, the two types of receivers designed achieve good system performance in Doppler compensation, ISI and ICI cancellation, and noise mitigation. With a perfect time synchronisation, the BER performance of the type 1 receiver outperforms the one of the type 2 receiver. However, the type 2 receiver outperforms the type 1 receiver in the sense of its unique robustness against time synchronisation errors. The theoretical probability of error for the two receivers is derived followed by supporting Monte Carlo simulation.

5) The tradeoff between system parameters is analysed, and the corresponding evaluation formulas are derived so that we have full control of the system

performance by selecting the parameters to suit specific communication scenarios.

For a discrete-time implementation of the receiver, a discrete-time approximation of the wavelet basis functions is used to form the analysis filters. In addition, since the rational orthogonal wavelets have infinite support in the time domain, the signalling wavelet has to be truncated. There is a tradeoff among the symbol rate, system complexity and approximation error in accordance with the sampling rate and the truncation length. This tradeoff is examined by simulations addressing the issues of system discretisation, the selection of wavelet scale factors, system sensitivity to the time synchronisation error and BER performance versus SNR respectively.

Compared with the existing Doppler compensation methods [93],[63],[17],[70],[42], the proposed broadband Doppler compensation structure leads to less residual Doppler due to the resolution of the multi-scale nature of the multipath/Doppler channel. However, the complexity of the system could increase for communication scenarios with slow moving platforms. The selected wavelet dilation factor has to be very small for small Doppler scales to be resolved which leads to long filters and low symbol rate for a bandlimited channel. Therefore, traditional Doppler compensation schemes are more applicable in this case. The proposed broadband Doppler compensation structure is more suitable for the scenarios when the Doppler scale (defined as the ratio of the speed of the mobile platform to the speed of the transmission carrier), is relatively large. In these cases, the shortage caused by high platform speed for traditional Doppler compensation structures actually becomes an advantage of the proposed system. For the communication between underwater vehicles moving at a speed of more than 45 knots, the magnitude of the Doppler compression or expansion can exceed 1% and the difference of Doppler scales between eigen paths reaches 0.1%. The length of filters has to be sufficiently large for this application, which is acceptable for practical implementation due to the low transmission speed of acoustic signals. For the type 1 receiver, an efficient receiver structure can be implemented via the tree-structured FWT algorithm proposed in chapter 2. However, for the type 2 receiver, the modified receiver structure is based on a parallel filter bank and the advantage it achieves for the synchronisation does not hold with a tree-structured filter bank. More efficient implementation may use FFT-based convolution algorithms and can benefit from advanced DSP techniques on parallel calculations. Furthermore,

the proposed system is also promising for its application to inter-satellite communications and other high-speed aircraft communications.

This page is blank

Chapter 5

CROW's Application to UWB IR Communications

5.1 Introduction

Ultra-wideband (UWB) technology for transmitting information spread over a large bandwidth plays an important role in broadband wireless communications [82], [83]. A UWB system features very short pulses on the order of nanoseconds as the transmission signal and operates at baseband without the involvement of carriers. Based on the Federal Communications Commission (FCC)'s regulation on the UWB spectrum of 3.1 to 10.6 GHz , a UWB pulse has to be carefully designed to conform to the FCC spectrum mask. Variant UWB pulses have been designed, e.g. the 2nd derivative of Gaussian, Rayleigh pulse, orthogonal Hermite pulses [7], [38] and wavelet-based UWB pulses based on B-spline wavelet [56], modulated Gaussian wavelet [61], Haar wavelet [96] and wavelet packets [25]. It is worth noting that all the existing UWB pulses are real pulses.

In this chapter, the design of complex Ultra-wideband (UWB) pulses is presented which enables the phase-shift keying (PSK) modulation for UWB Impulse Radio (IR) Communications. Two classes of complex UWB pulses are proposed based on complex Gaussian wavelets and the complex rational orthogonal wavelets (CROWs) proposed in chapter 2. The designed complex UWB pulses are in accordance with the FCC regulated spectrum for UWB communications. Formulae in closed form are derived for a full control of the time and frequency properties of the designed UWB pulses. The system

characterisation of the complex UWB pulse-based PSK modulation and demodulation is presented. A novel PSK demodulator based on complex wavelet signalling is proposed with unique robustness against timing jitter.

Besides the inherent advantages of PSK modulation which lead to high power efficiency and high data rate, the proposed PSK scheme in the UWB communication context provides a more flexible way to construct new UWB modulation schemes by combining PSK with other basic modulation options such as the pulse amplitude modulation (PAM) and the pulse position modulation (PPM). In addition, based on the derived formulae and the groundwork in chapter 3 on the CROW-based OFDM, the proposed UWB pulse design method also provides a solution to the construction of multiband (MB) UWB OFDM systems.

The chapter is organised as follows. The design of two classes of complex UWB pulses is presented in section 5.2. Section 5.3 presents the signal characterisation of UWB PSK communication based on complex UWB pulses. The corresponding receiver design is given together with some simulation results illustrating the demodulation process. Section 5.4 presents the conclusions of this chapter.

5.2 Complex UWB Pulse Construction

5.2.1 Complex Gaussian Wavelet Based UWB Pulses

We define the complex Gaussian wavelet[6] by

$$p(t) = e^{-j2\pi f_c(\frac{t}{\xi})}\, e^{-(\frac{t}{\xi})^2}, \tag{5.1}$$

where ξ is the time scaling factor and f_c is the basis wavelet center frequency. Although the Gaussian wavelet has infinite support in both the time domain and the frequency domain, it can be derived that p(t) has an effective support of $[-3.5\xi, 3.5\xi]$ (s) in the time domain and an effective support of $[(f_c - 1.5)\xi^{-1}, (f_c + 1.5)\xi^{-1}]$ (Hz) in the frequency domain which contains more than 99.99% of the total energy. Therefore, $p(t)$ has a waveform of

[6]Note that the definition here is different from that of complex Gaussian wavelets in the Matlab wavelet toolbox and is closer to the definition of Gabor wavelets or complex Morlet wavelets. We denote this definition as complex Gaussian wavelet in the sense that it is based on scaled versions of the modulated complex Gaussian function.

length $T = 7\xi$ and the bandwidth of $BW = 3\xi^{-1}$. An example of the complex Gaussian wavelet with $f_c = 1$Hz and $\xi = 1$ is shown in Fig. 5.1.

Two parameters, ξ and f_c, in the definition (5.1) control the time and frequency properties of $p(t)$. To meet the FCC regulation on the UWB spectrum $[3.1, 10.6]$ (GHz), the two parameters have to be selected carefully to conform the FCC spectrum mark. The constraints on these two parameters are derived as follows:

$$(f_c - 1.5)\xi^{-1} \geq 3.1 \text{ (GHz)} \tag{5.2}$$

$$(f_c + 1.5)\xi^{-1} \leq 10.6 \text{ (GHz)} \tag{5.3}$$

$$BW = 3\xi^{-1} < 7.5 \text{ (GHz)} \tag{5.4}$$

$$T = 7\xi = \sigma \text{ (ns)} \tag{5.5}$$

where σ is the desirable pulse length in nanosecond for a specific application.

Equations (5.2) and (5.4) lead to the lower bound on the value of f_c:

$$f_c \geq lb(f_c) = \frac{3.1}{7.5/3} + 1.5 = 2.74 \text{ (Hz)}. \tag{5.6}$$

The upper bound of f_c can be derived from equations (5.3) and (5.5) as

$$f_c \leq ub(f_c) = \frac{10.6\sigma}{7} - 1.5 \text{ (Hz)}. \tag{5.7}$$

From (5.6) and (5.7), we see that for the existence of a solution of f_c, there is $lb(f_c) \leq ub(f_c)$. Therefore σ has to satisfy

$$\sigma \geq (2.74 + 1.5)7/10.6 = 2.8 \text{ (ns)}. \tag{5.8}$$

Based on a designed UWB pulse length of σ, $\sigma > 2.8$ns, the 2 parameters for the pulse definition can be determined by

$$\begin{aligned} &\xi = \sigma/7 \ (\times 10^{-9}), \\ &2.74 = lb(f_c) < f_c < ub(f_c) = \frac{10.6\sigma}{7} - 1.5 \text{ (Hz)} \end{aligned} \tag{5.9}$$

Notice that f_c can be selected from a range of values, therefore the designed UWB pulses are not unique. If the length of the UWB pulse is allowed to be relatively long so that the bandwidth of the pulse is relatively narrow comparing to the FCC regulated 7.5

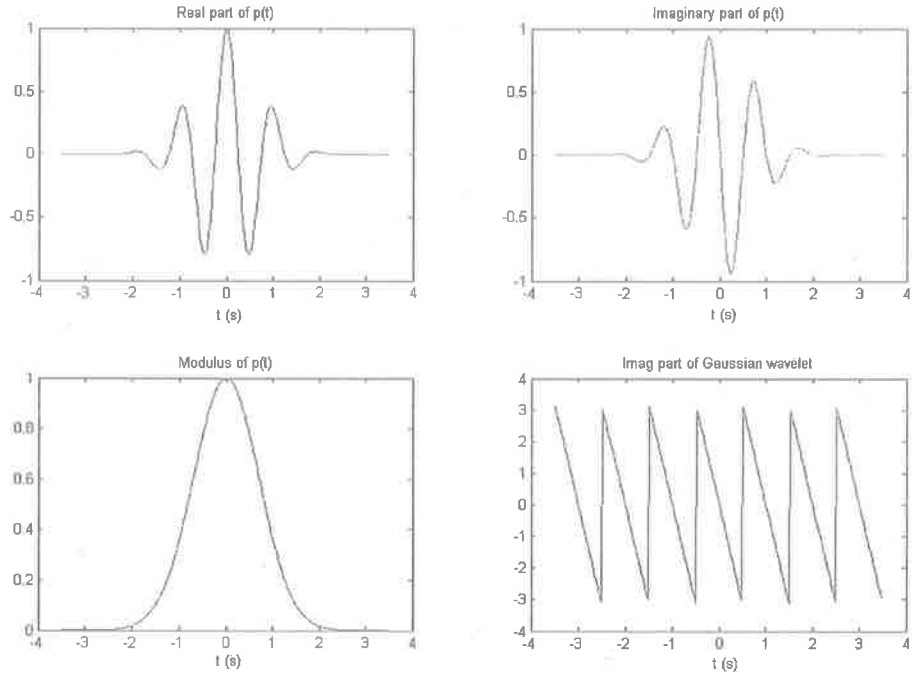

Figure 5.1. Complex Gaussian wavelet with $f_c = 1$ and $\xi = 1$.

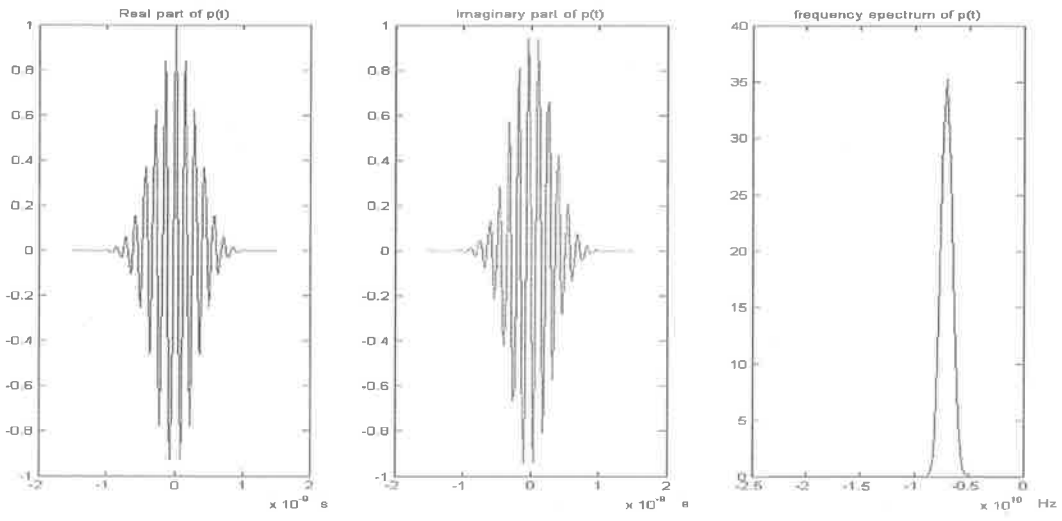

Figure 5.2. A complex Gaussian wavelet-based UWB pulse and its frequency spectrum

GHz UWB bandwidth, multiple f_c values can be selected to construct multiple orthogonal UWB pulses which meet the FCC mask. In this case, the interval between the selected f_c has to satisfy

$$\Delta f_c = f_c^{(i+1)} - f_c^{(i)} > 3 \text{ (Hz)}, i = 1, \cdots, N, \tag{5.10}$$

where the number of available orthogonal pulses N is determined by

$$\begin{aligned} N &= \left\lfloor \frac{ub(f_c) - lb(f_c)}{\Delta f_c} + 1 \right\rfloor \\ &\approx \lfloor 0.5\sigma - 0.413 \rfloor, \end{aligned} \tag{5.11}$$

where the operation $\lfloor \cdot \rfloor$ rounds the amount to the nearest integer less than or equal to its value.

As an example, Fig. 5.2 shows a complex Gaussian wavelet-based UWB pulse and its frequency spectrum with $\sigma = 3$ ns. ξ is around 0.429×10^{-9}. f_c is selected to be 3 Hz from the range of $2.74 < f_c < 3.043$ Hz.

5.2.2 Complex Rational Orthogonal Wavelet Based UWB Pulses

In a similar manner, another class of complex wavelets, the complex rational orthogonal wavelets (CROWs) proposed in chapter 2, can be designed as UWB pulses in accordance with the FCC regulation for UWB communications.

Defining the UWB pulse as

$$p(t) = \psi_+(t/\xi), \tag{5.12}$$

where ξ is the time scaling factor, and denoting the bandwidth and pulse length as BW and T respectively, we have the constraints on the pulse design as

$$\omega_1 \xi^{-1} \geq 3.1 \text{ (GHz)} \tag{5.13}$$

$$\omega_3 \xi^{-1} \leq 10.6 \text{ (GHz)} \tag{5.14}$$

$$BW = \xi^{-1} < 7.5 \text{ (GHz)} \tag{5.15}$$

$$T = 16\xi = \sigma \text{ (ns)}. \tag{5.16}$$

By substituting (2.13) into the equations of constraints, the two parameters, q and ξ, can be selected by these constraints. From equations (5.13) and (5.15), we have

$$\frac{1}{2}(q - \frac{q}{2q+1}) \geq 3.1/7.5, \; q \in \mathbb{Z}^+, \tag{5.17}$$

which leads to the lower bound of q as

$$q \geq lb(q) = 2, \; q \in \mathbb{Z}^+. \tag{5.18}$$

From equations (5.14) and (5.16), we have

$$\begin{aligned} & \frac{(q+1)^2}{2q+1} < 10.6\sigma/16 \\ \Rightarrow \quad & q < \frac{2(0.6625\sigma - 1) + \sqrt{(2(0.6625\sigma) - 1)^2 - 1}}{2} \\ & < \frac{2(0.6625\sigma - 1) + 2(0.6625\sigma) - 1}{2} \\ \Rightarrow \quad & q < ub(q) = \frac{2.65\sigma - 3}{2}, \; q \in \mathbb{Z}^+. \end{aligned} \tag{5.19}$$

For the existence of a solution of q, there is $lb(q) \leq ub(q)$. Therefore σ has to satisfy

$$\begin{aligned} & \frac{2.65\sigma - 3}{2} \geq 2 \\ \Rightarrow \quad & \sigma \geq 7/2.65 \approx 2.64 \text{ (ns)}. \end{aligned} \tag{5.20}$$

Based on a designed UWB pulse length of σ, $\sigma \geq 2.64\ ns$, the 2 parameters for the pulse definition can be determined by

$$\begin{aligned} & \xi = \sigma/16 \ (\times 10^{-9}), \\ & 2 = lb(q) \leq q < ub(q) = \frac{2.65\sigma - 3}{2}, \; q \in \mathbb{Z}^+. \end{aligned} \tag{5.21}$$

Notice that q can be selected from a set of integers, therefore the designed UWB pulses are not unique. If the length of the UWB pulse σ is allowed to be relatively long, multiple q values can be selected from the range of $[2, \; 2 + (M - 1)]$, where M is the number of available q and is determined by

$$\begin{aligned} M &= \lfloor ub(q) - lb(q) \rfloor \\ &\approx \lfloor 1.325\sigma - 2.5 \rfloor . \end{aligned} \tag{5.22}$$

For a selected q, multiple orthogonal UWB pulses are available with overlapped frequency spectrum and a dilation factor of $a = \frac{q+1}{q}$. The number of available orthogonal UWB

pulses N can be calculated by

$$\begin{aligned} N &= \left\lfloor \log_a \frac{\omega_1 \xi^{-1}}{3.1} + 1 \right\rfloor \\ &\approx \left\lfloor \frac{\ln \frac{5.161q^2}{\sigma(2q+1)}}{\ln \frac{q+1}{q}} + 1 \right\rfloor . \end{aligned} \tag{5.23}$$

The maximum number of orthogonal pulses N_{max} is reached with the maximum q value, $q = M+1$, where M is calculated by (5.22). To form a multiple pulse division multiplexing scheme, there is an additional constraint on the minimum q value for a selected number of pulses N derived by

$$\begin{aligned} &\omega_1 \xi^{-1} \geq 3.1 \text{ (GHz)} \\ &\omega_1 \xi^{-1} (\frac{q+1}{q})^{N+1} \leq 10.6 \text{(GHz)} \\ &\Rightarrow q \geq \left\lceil ((\frac{10.6}{3.1})^{\frac{1}{N+1}} - 1)^{-1} \right\rceil , \end{aligned} \tag{5.24}$$

where the operation $\lceil \cdot \rceil$ rounds to the nearest integer larger than or equal to its element.

An example of the CROW with $q = 1$ and $\xi = 1$ is shown in Fig. 5.3. Fig. 5.4 shows a CROW-based UWB pulse and its frequency spectrum with $\sigma = 3$ ns, ξ is valued at 0.1875×10^{-9}, and q is selected to be 2.

For longer pulse lengths, a comparison of the number of available multiple overlapped orthogonal pulses based on Gaussian and CROW pulses, N_{max} versus the desirable UWB pulse length σ is shown in Fig. 5.5 based on the formulae in (5.11) and (5.23). It indicates that with the same pulse length σ, the number of available orthogonal pulses based on the CROW is larger than that based on complex Gaussian wavelet. It demonstrates that CROW-based schemes could achieve better spectrum efficiency over complex Gaussian wavelet-based schemes. Moreover, the advantage gets more significant if longer pulse length is allowed.

5.3 CROW-Based PSK Modulation for UWB IR

In this section, we present the system characterisation of UWB PSK communication based on complex UWB pulses. Complex wavelet-based PSK modulation has been presented in [91]. Follow the derivation in [91], the modulated UWB signal and its properties were

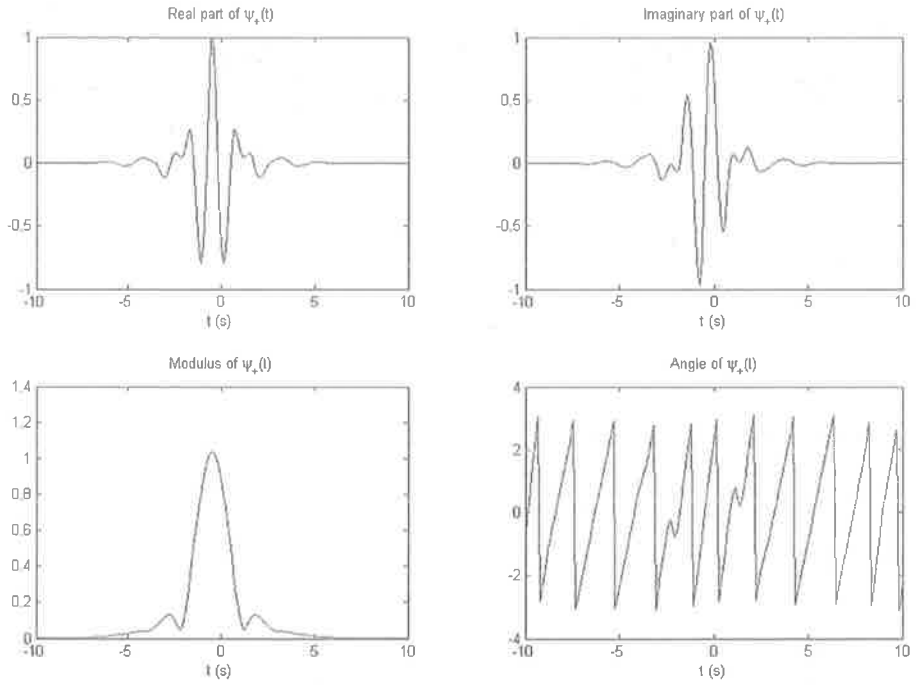

Figure 5.3. Complex rational orthogonal wavelet with $q = 1$ and $\xi = 1$.

studied. The novel demodulation method presented in [91] is introduced here. This demodulation method leads to a receiver structure with unique robustness against timing jitter which is a highly desired property for UWB communication systems.

5.3.1 M-ary PSK Modulation with Complex UWB Pulses

The transmitted PSK signals are represented as

$$\begin{aligned} s_m(t) &= \Re[e^{j\theta_m}\, p(t)],\ m = 1, 2, \cdots, M, \\ &= \cos\theta_m\, p_r(t) - \sin\theta_m\, p_i(t), \end{aligned} \tag{5.25}$$

where $\Re[.]$ returns the real part of a complex signal, $\theta_m = \frac{2\pi}{M}(m-1) + \theta_0$ and θ_0 is the initial phase coefficient, $p_r(t)$ and $p_i(t)$ are the real and imaginary parts of the complex UWB pulse $p(t)$ respectively. The data sequence is mapped to the phase of the pulse sequence as θ_m. Comparing with the conventional PSK modulation [62], we see that the sinusoidal carrier signal with pulse shaping is replaced by the complex pulse. The

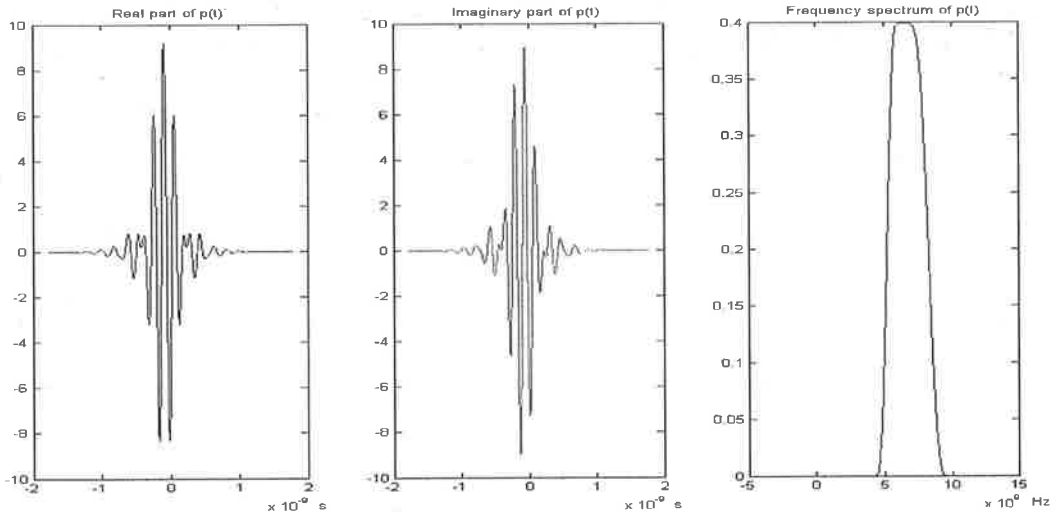

Figure 5.4. A CROW-based UWB pulse and its frequency spectrum

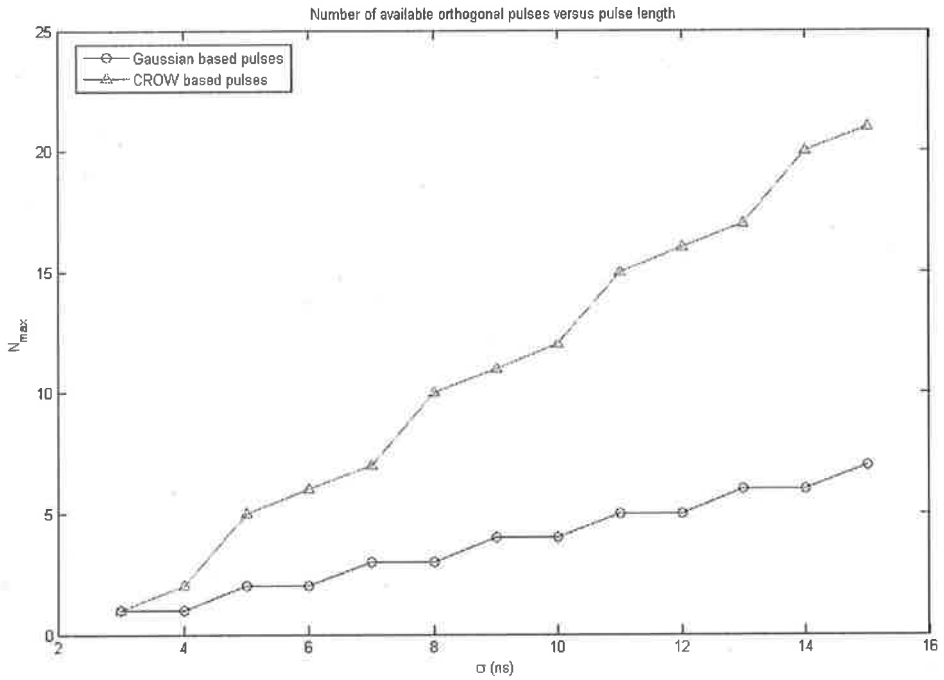

Figure 5.5. Number of available orthogonal pulses versus the pulse length

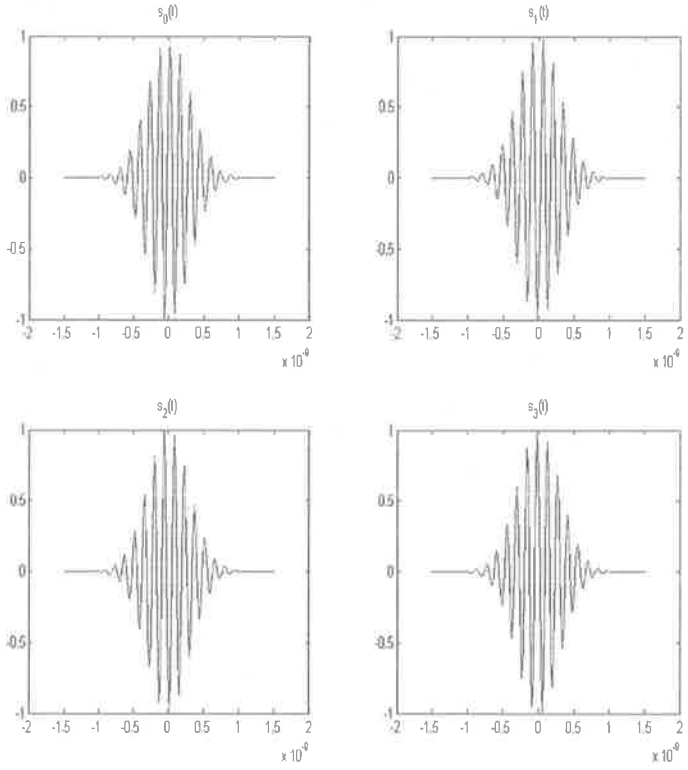

Figure 5.6. Transmitted 4-PSK signal waveforms based on complex Gaussian UWB pulse shown in Fig. 5.2

transmitted signal is a linear combination of two orthogonal wavelets $p_r(t)$ and $p_i(t)$ in contrast to the conventional orthogonal sine and cosine carriers.

Using the UWB pulse shown in Fig. 5.2, the signal waveforms of a 4-PSK modulation are shown in Fig. 5.6. The initial phase θ_0 is $\frac{\pi}{4}$.

5.3.2 UWB Receiver Design

As proposed in [91], a novel receiver structure is applicable based on the complex wavelet signalling, in this case, the complex wavelet pulse UWB signalling. The receiver structure is shown in Fig. 5.7 and Fig. 5.8 with complex signal and real signal flow respectively.

The real and imaginary outputs of the demodulator before sampling, $r_c(t)$ and $r_s(t)$, can be expressed as

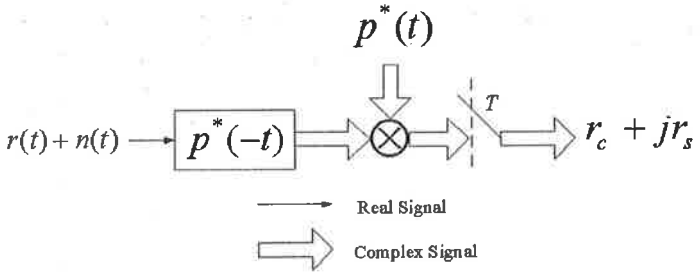

Figure 5.7. PSK demodulation with complex signal flow

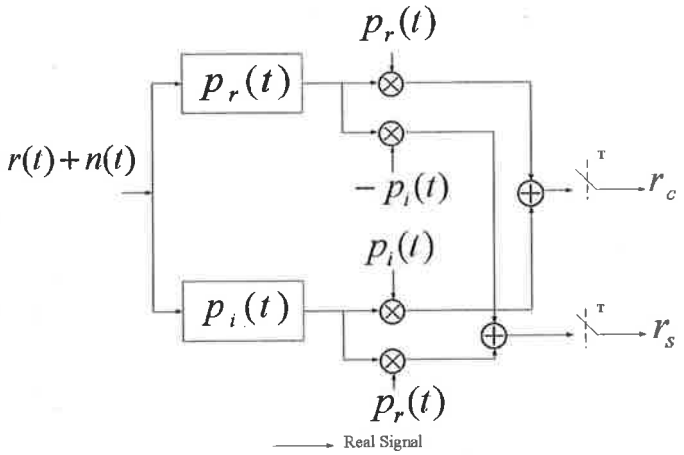

Figure 5.8. PSK demodulation with equivalent real signal flow

$$
\begin{aligned}
r_c(t) &= (A_{mc}\psi(t) - A_{ms}\hat{\psi}(t)) * \psi(t) \cdot \psi(t) \\
&+ (A_{mc}\psi(t) - A_{ms}\hat{\psi}(t)) * \hat{\psi}(t) \cdot \hat{\psi}(t) \\
&+ n_c(t) \qquad (5.26) \\
r_s(t) &= (A_{mc}\psi(t) - A_{ms}\hat{\psi}(t)) * \psi(t) \cdot (-\hat{\psi}(t)) \\
&+ (A_{mc}\psi(t) - A_{ms}\hat{\psi}(t)) * \hat{\psi}(t) \cdot \psi(t) \\
&+ n_s(t) \qquad (5.27)
\end{aligned}
$$

where

$$
\begin{aligned}
n_c(t) &= n(t) * \psi(t) \cdot \psi(t) + n(t) * \hat{\psi}(t) \cdot \hat{\psi}(t) \\
n_s(t) &= n(t) * \psi(t) \cdot (-\hat{\psi}(t)) + n(t) * \hat{\psi}(t) \cdot \psi(t), \qquad (5.28)
\end{aligned}
$$

and $n(t)$ is the AWGN noise. Notice that $\psi(t) * \psi(t) = \phi_{\psi\psi}(t)$ is the autocorrelation function of $\psi(t)$. For abbreviation we denote this autocorrelation function as the function $v(t)$ and the following equations can be easily derived that

$$\begin{aligned} \hat{\psi}(t) * \psi(t) &= \hat{v}(t), \\ \hat{\psi}(t) * \hat{\psi}(t) &= -v(t). \end{aligned} \tag{5.29}$$

Then the real part of the output signal $r_c(t)$ (equation 5.27) can be rewritten as

$$\begin{aligned} r_c(t) &= A_{mc}(v(t) \cdot \psi(t) + v(t) \cdot \hat{\psi}(t)) \\ &+ A_{ms}(v(t) \cdot \hat{\psi}(t) - \hat{v}(t) \cdot \psi(t)) \\ &+ n_c(t), \end{aligned} \tag{5.30}$$

We see that $v(t)$ is related with $\psi(t)$ by $V(\omega) = \Psi(\omega)^2$, where $V(\omega)$ and $\Psi(\omega)$ are the frequency spectrum of $v(t)$ and $\psi(t)$ respectively. Define $u(t) = v_+(t) \cdot \psi_+^*(t)$, where $v_+(t)$ is the analytic form of $v(t)$ and $\psi_+^*(t)$ is the conjugate analytic form of $\psi(t)$. It can be further proved that

$$\begin{aligned} v(t) \cdot \psi(t) + v(t) \cdot \hat{\psi}(t) &= u(t), \\ v(t) \cdot \hat{\psi}(t) - \hat{v}(t) \cdot \psi(t) &= \lambda(t) \approx 0, \end{aligned} \tag{5.31}$$

where $\lambda(t)$ has the spectrum $\Lambda(\omega)$ that

$$\begin{aligned} \Lambda(\omega) &= H(-\omega)(U(\omega) - U(-\omega)) - H(\omega)(U(\omega) - U(-\omega)), \\ &= 2H(\omega)(U(\omega) - U(-\omega)), \end{aligned} \tag{5.32}$$

where $U(\omega)$ is the frequency spectrum of $u(t)$. $u(t)$ is a lowpass signal and $U(\omega) - U(-\omega) \approx 0$ because of the nearly symmetric spectrum of $U(\omega)$.

Therefore, $r_c(t)$ in equation 5.27 can be simplified as

$$r_c(t) = A_{mc}u(t) + n_c(t). \tag{5.33}$$

Following a similar derivation, the imaginary part of the output signal $r_s(t)$ can be expressed as

$$r_s(t) = A_{ms}u(t) + n_s(t) \tag{5.34}$$

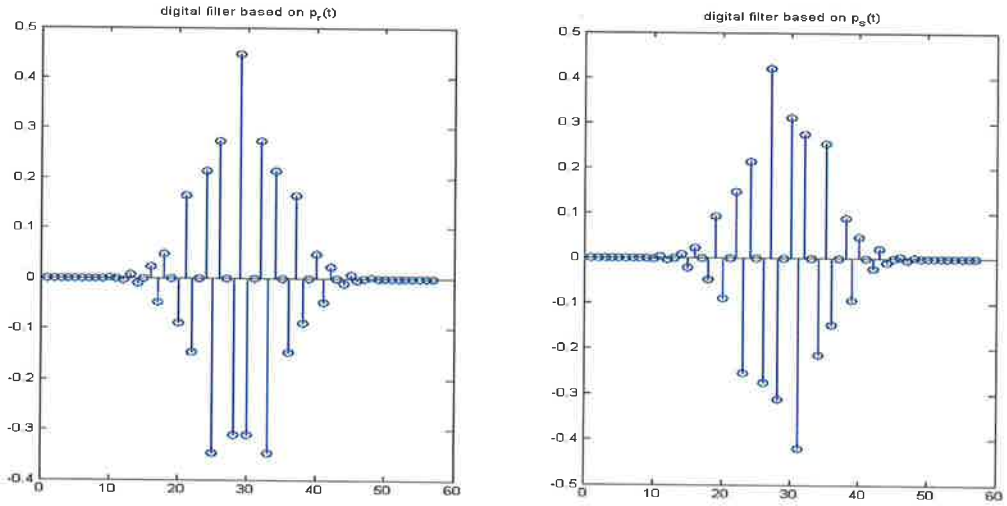

Figure 5.9. Two filters at the receiver for PSK modulation

The output decision variables after the periodic sampling are

$$\begin{aligned} r_c &= A_{mc}u(T-T_0)+n_c(T-T_0), \\ r_s &= A_{ms}u(T-T_0)+n_s(T-T_0), \end{aligned} \tag{5.35}$$

where T is the symbol period and T_0 is a fixed initial time shift for the periodic sampling which can be selected according to the waveforms of $r_c(t)$ and $r_s(t)$. The periodic sampling process can be replaced by integration and then periodic sampling in the receiver design. The output decision variable is based on the sampling of the lowpass signal $u(t)$, which results in the improved robustness against the timing error.

Based on the transmitted signals shown in Fig. 5.6, the two filters as shown in the receiver structure can be constructed by discretising the continuous waveform of $p(t)$ at the Nyquist rate and are shown in Fig. 5.9. Both of them have the filter length of 57.

Fig. 5.10(a) shows the scatterplot of the output signal before sampling with perfect time synchronisation. The corresponding waveforms of $r_c(t)$ and $r_s(t)$ are shown in Fig. 5.11. As shown in [91], this demodulation structure has the robustness against the timing error as large as 30% of the pulse period comparing to the traditional correlation based demodulator which only works with a timing error less than 1%. For UWB systems, the benefit of this demodulation structure is even more significant because of the relatively long intervals between the pulses. The scatterplot of the output $r_c(t)+jr_s(t)$

with different timing delay errors and an example of the waveforms of $r_c(t)$ and $r_s(t)$ are shown in Fig. 5.10(b)(c)(d) and Fig. 5.12. Similar performance is achieved for negative timing delay errors. As shown in Fig. 5.10(b) and Fig. 5.12, with a timing delay valued at 80% of the pulse period, the demodulated 4 signal waveforms remain orthogonal but with much smaller amplitudes which makes it very sensitive to noise. In this case, the demodulation performance relies on the signal-to-noise ratio (SNR) of the system which also shows good noise mitigation performance with relatively small but still significant timing error resistance as shown in Fig. 5.10(d).

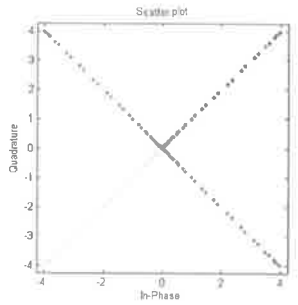

(a) Perfect timing, without noise

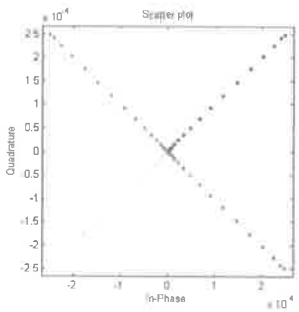

(b) timing error 80%, without noise

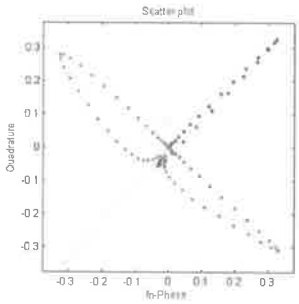

(c) timing error 40%, measured 20dB noise

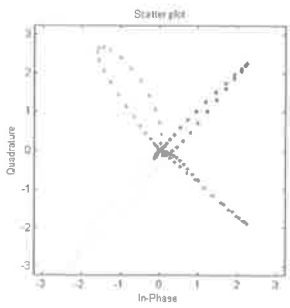

(d) timing error 20%, measured 0dB noise

Figure 5.10. Scatterplot of the output demodulated signal before sampling

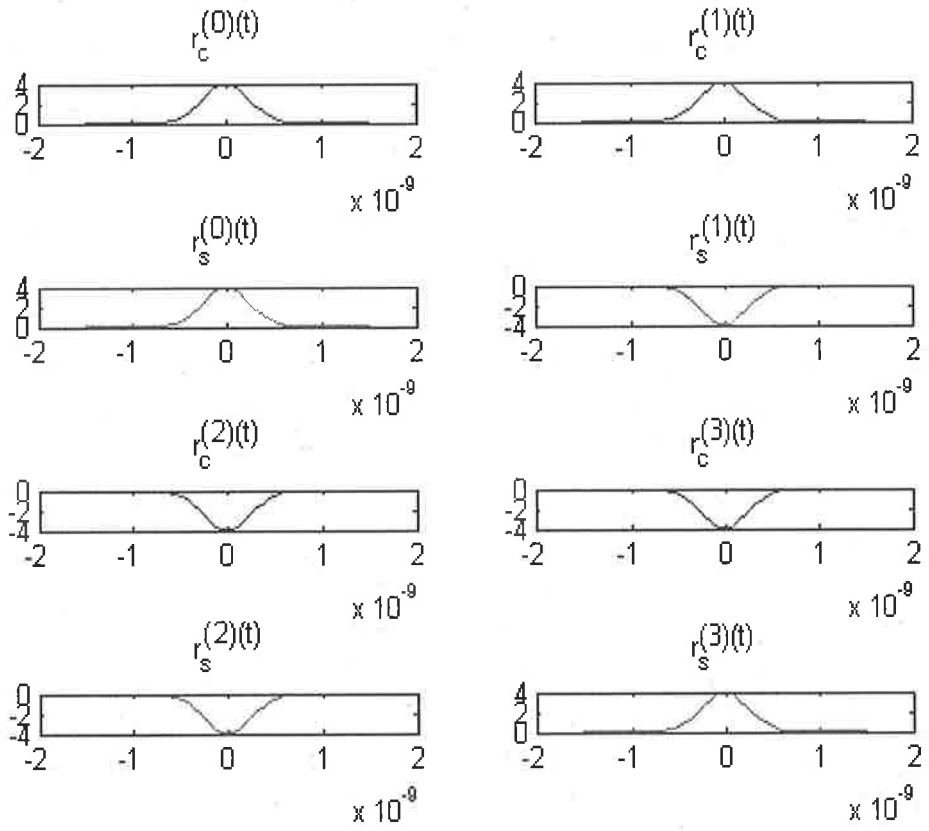

Figure 5.11. Signal waveforms of $r_c(t)$ and $r_s(t)$ for 4-PSK signalling (perfect synchronisation)

5.4 Conclusions

The main contributions of this chapter are summarised in the following together with some remarks.

1) The PSK modulation is proposed for UWB IR communications based on complex UWB pulses.

Based on real UWB pulses, various modulation methods have been proposed for UWB systems, including the conventional binary and M-ary PAM and PPM, BPSK, OOK [34], as well as many modified modulation methods based on the conventional ones, such as the combined M-ary PAM and PPM [95], combined BPSK and M-ary PPM [94],

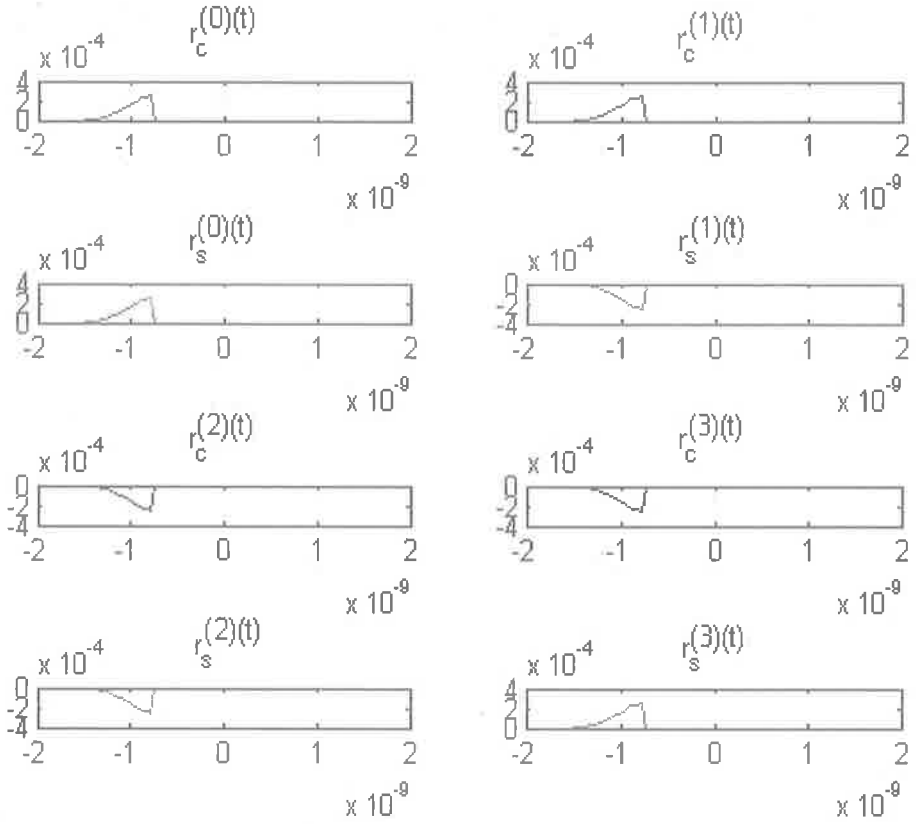

Figure 5.12. Signal waveforms of $r_c(t)$ and $r_s(t)$ for 4-PSK signalling (timing error 80% of the pulse length)

and M-ary PPM with multiple orthogonal UWB pulses [45]. To address the issues of channel estimation, multiple-access, transmit-reference (TR)-based modulation [74] and time-hopping (TH)/direct sequence (DS) spread spectrum PPM schemes [94] are also proposed for UWB systems.

This chapter demonstrates that the PSK modulation is possible for UWB IR communications based on complex UWB pulses. Compared with other basic modulation schemes, e.g., PAM and PPM, based on real UWB pulses, PSK modulation has the inherent advantages of high power efficiency and high data rate under the circumstance of a sufficient SNR level and similar system configurations. More specifically, it provides a more flexible way to construct new modulation schemes, such as combined PSK and

PPM modulation and combined PSK, PAM and PPM modulation, which are able to take advantage of the benefits of different modulation schemes and achieve an optimal tradeoff to suit a specific application.

2) Two classes of complex UWB pulses are proposed based on complex Gaussian wavelets and the CROWs respectively.

Formulae in closed form (5.9), (5.21) are derived for a full control of the time and frequency properties of the designed UWB pulses. The proposed UWB pulse design method also provides a solution to the construction of MB UWB systems by using relatively long complex UWB pulses (large values of σ). Explicit formulae (5.11), (5.23), (5.22) are derived that indicate the number of subbands available within the FCC mask and the waveforms of the orthogonal subband UWB pulses. Another important fact revealed by this thesis is that the CROW-based UWB orthogonal pulses have overlapped spectra and therefore have better spectrum efficiency than the complex Gaussian wavelet-based UWB pulses. An indication is that with the same pulse length σ, the number of available orthogonal pulses based on CROW is larger than that based on complex Gaussian wavelet as derived in (5.11) and (5.23) and illustrated in Fig. 5.5.

It is worth noting that the CROW-based OFDM proposed in chapter 3 also provides the groundwork for the construction of MB UWB OFDM systems from a different angle. The extension to the CROW-based Multiband UWB OFDM systems with improved spectrum efficiency and robustness through time-frequency dispersive channels is straightforward.

3) A novel PSK demodulator is proposed based on complex wavelet signalling which has unique robustness against timing jitter.

A novel PSK demodulator based on complex wavelet signalling is developed and achieves unique robustness against timing errors. As shown in section 5.3.2, this demodulation structure has the robustness against a timing error as large as 30% of the pulse period. (Note that the traditional correlation based demodulator requires a timing error less than 1%.) For UWB systems, the benefit of this demodulation structure is even more significant because of the relatively long intervals between the pulses.

This page is blank

Chapter 6

CROW's Application to Radio Vehicular Communications

6.1 Introduction

In this chapter, signal format design is addressed for OFDM-based transmission schemes that are able to cope with the Doppler dispersion due to terminal motions [36] in radio vehicular communications. As a special case of the radio vehicular communication systems, we target the OFDM design for mobile wireless local area networks (WLANs).

More than a complement of the cellular communications networks, the WLANs provide flexible high bit rate data services at hot spots [36] and will play an important role in future 4th generation (4G) broadband ubiquitous communication infrastructure. In current IEEE 802.11 standards [5], WLAN can provide up to 54 Mbps data transmission rate, and the services are intended for stationary or low mobility users. However, communications between WLAN devices can occur in high velocity mobile environments, and mobile WLAN devices would be expected to transfer data between vehicles at speeds up to 120km/h [53]. As mentioned in [36], if a future WLAN standard can cope with high mobility of users with a bit higher transmission rate, we will be able to call it a 4G system.

A major issue towards this 4G WLAN is the physical layer transmission techniques with high mobility support. Based on the groundwork in chapter 3, where a new OFDM

scheme based on complex rational orthogonal wavelets (CROW-OFDM) was proposed, this chapter develops a multi-band (MB) CROW-OFDM scheme particularly for WLAN applications. The system performance in multipath/mobile environments is analysed by simulations using Jakes' channel model [40].

The chapter is organised as follows. The construction of MB-CROW-OFDM for WLAN applications is presented in section 6.2. The system performance analysis is detailed in section 6.3 addressing stationary multipath channels and Doppler dispersive channels respectively. Section 6.4 presents the conclusions of this chapter.

6.2 MB-CROW-OFDM Scheme

Due to the good time-frequency localisation property of CROW wavelets, the CROW-OFDM proposed in chapter 3 provides an alternative solution opposite to the FFT/IFFT based DFT-OFDM in high-mobility vehicular communication scenarios. In this section, we present the MB-CROW-OFDM scheme particularly for high mobility WLAN applications.

As a wavelet-based OFDM scheme, CROW-OFDM has an important feature which is the non-uniform bandwidth of the subchannels. This feature facilitates the implementation of multi-rate transmission for multiple services with different data rate requirements. However, the non-uniform bandwidth would lead to variant transmission properties of the subchannels in frequency selective channels. With N subchannels, the bandwidth difference of the first and the N-th channel reaches $a^{(N-1)}$ times. It might lead to a huge difference of the symbol rates and the transmission properties which depend on the value of a and N. For a dyadic wavelet ($a = 2$) and 64 subchannels, the difference reaches 2^{64} times. Moreover, the bandwidth of each subchannel should be limited as well so that each subchannel could be regarded as a flat fading channel in order to combat the multipath. Therefore, instead of using one tree for all the subchannels, a combined parallel multi-tree structure, e.g. for 64-subchannel OFDM, 16 trees, each of which has 4 subchannels, could be applied so that the propagation properties of the subchannels would not vary too much because of the non-uniform partition of the spectrum. This scheme is termed as the MB-CROW-OFDM scheme.

Referring to the IEEE 802.11a/g standards [1], a typical specification of DFT-OFDM for WLAN applications is given as follows. For a 20 MHz channel spacing, a 64-point FFT is used for 52 subchannels (48 data subcarriers and 4 pilot subcarriers) with a subcarrier spacing of $\Delta_F = 20\text{MHz} / 64 = 0.3125\,\text{MHz}$. The FFT symbol period is $T_{FFT} = 1/\Delta_F = 3.2\,\mu\text{s}$. With a CP of length $T_{GI} = 0.8\,\mu\text{s}$, the transmitted symbol period is $T_{SYM} = T_{FFT} + T_{GI} = 4\,\mu\text{s}$ which leads to the bit rate of 24 Mbps with QPSK modulation or 12 Mbps with 1/2 coding rate.

With MB-CROW-OFDM, we divide the 20 MHz channel spacing into 16 subbands, each of which has a bandwidth of 1.25 MHz and is further divided into 4 subchannels by implementing 4-channel CROW-OFDM. Fig. 6.1 (a) shows the separate spectra of the CROW-OFDM signal in 4 subchannels within one subband with $a = 3/2$. Fig. 6.1 (b) shows the combined spectrum of the 4-channel CROW-OFDM signal. The spectrum of transmitted signal with 64 subchannels and 16 subbands has a form of combined and shifted 4-channel basedband CROW-OFDM spectrum without overlapping as shown in Fig. 6.1 (c). For comparison, the spectra of the MB-CROW-OFDM signal with $q = 8$ and thus $a = 9/8$ are shown in Fig 6.2 which illustrates evener subchannel frequency division with a smaller a value within one subband.

To form the bandwidth of the 4-channel baseband signal to be $BW = 1.25\,\text{MHz}$, the output of the 4-channel synthesis FB must be scaled by a factor of ξ. Numbering the 4 channels from the lower frequency band by $1, \cdots, 4$, and assuming that the signalling pulse in channel-4 (the highest frequency band) is the wavelet basis function $\psi_+(t)$, the scaling factor ξ can be expressed as

$$\xi = \frac{BW_0}{a^2\omega_1(1 - a^{-(N+1)})}, \tag{6.1}$$

where $BW_0 = 1.25\,\text{MHz}$ and $N = 4$. To move the 16 baseband signals to certain frequency band in order to conform to the WLAN signal spectrum, e.g. the frequency bandwidth, $BW = 20\,\text{MHz}$, from $f_L = 5.17\,\text{GHz}$ to $f_H = 5.19\,\text{GHz}$, the baseband signal must be further modulated by sinusoidal carriers, $f_c^{(i)}, i = 1, \cdots, 16$, calculated by

$$f_c^{(i)} = f_L^{(i)} - \omega_1 a^{-N} \xi, \tag{6.2}$$

where $f_L^{(i)} = f_L + (i-1)BW_0$.

The available symbol rate with NOL signalling can be calculated by

$$R^{NOL} = \frac{M\xi}{T_\psi}(1 + a^{-1} + \cdots + a^{1-N}), \tag{6.3}$$

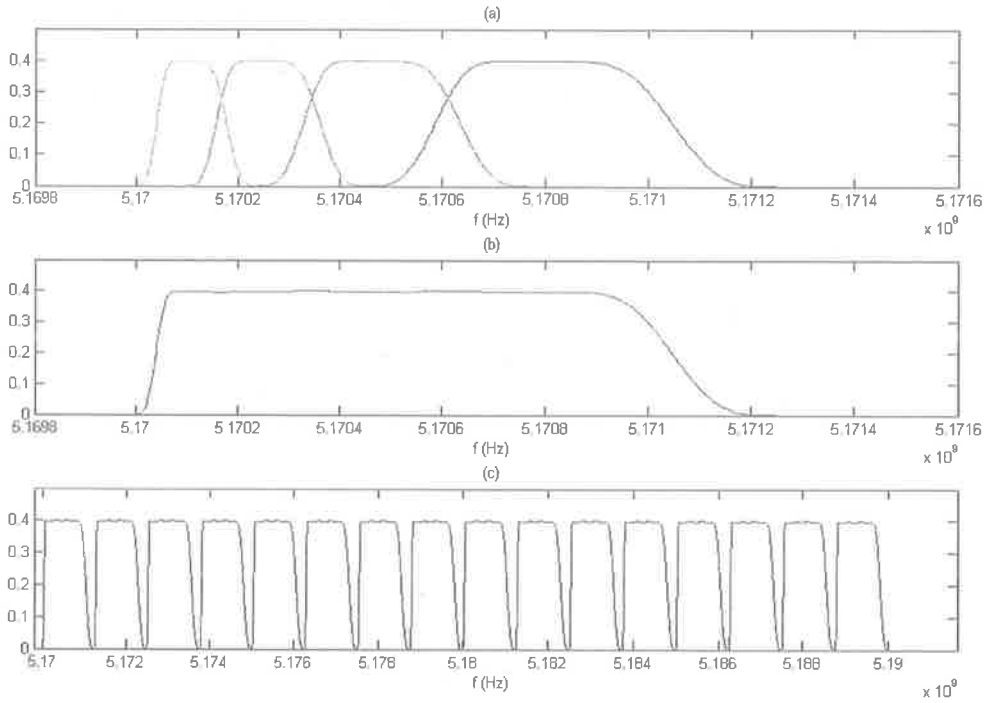

Figure 6.1. Spectrum of MB-CROW-OFDM signal with $q = 2$. (a) spectra of 4 subchannels in one subband, (b) spectrum of one subband, (c) spectrum of 16 subbands.

where M is the number of parallel trees and $M = 16$, T_ψ is the truncation length of the wavelet basis function $\psi_+(t)$. The symbol rate with OL signalling is given as

$$R^{OL} = R^{NOL}\frac{T_\psi}{q}. \tag{6.4}$$

As an example, the design parameters for MB-CROW-OFDM with different q values are shown in Table 6.1. T_ψ is set to be an integer number of 10. The formulae to calculate the bandwidth efficiency of non-overlapped (NOL) and overlapped (OL) CROW-OFDM, ρ^{NOL} and ρ^{OL} were presented in chapter 3, section 3.5. As mentioned therein, the OL CROW-OFDM utilises the shift orthogonal property of the CROW wavelet and has the advantage of improved bandwidth efficiency over the NOL scheme if q is smaller than T_ψ. If the q value is equal to or larger than T_ψ, the NOL and OL schemes are equivalent as shown in Table 6.1 for $q = 10$. Notice that the calculated symbol rates are slightly lower than the rates calculated by the multiplication of the bandwidth efficiency and the

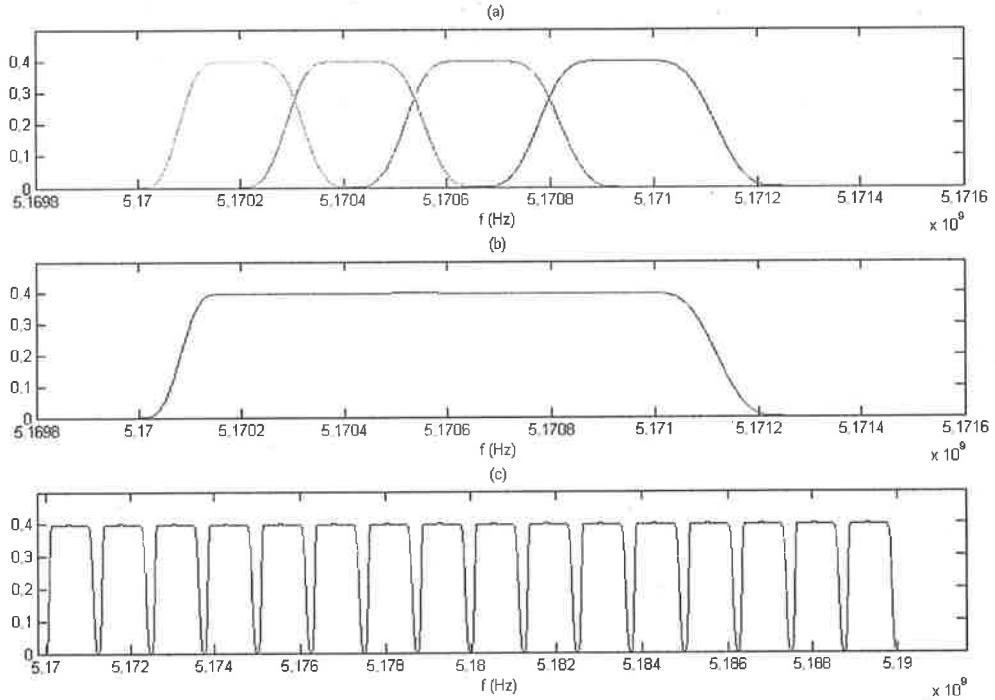

Figure 6.2. Spectrum of MB-CROW-OFDM signal with $q = 8$. (a) spectra of 4 subchannels in one subband, (b) spectrum of one subband, (c) spectrum of 16 subbands.

20 MHz bandwidth, because the theoretical bandwidth efficiency is based on a partition of the frequency axis with an infinite number of subcarriers.

6.3 Analysis of System Performance

In this section, we examine the multipath robustness, sensitivity to Doppler dispersion and noise mitigation performance of the proposed MB-CROW-OFDM. The simulations are carried out and analysed for both stationary multipath and mobile Doppler dispersive channels using Jakes' model. Its performance is compared with that of the DFT-OFDM specified in IEEE 802.11a/g standards.

Table 6.1. Bandwidth Efficiency and Symbol Rate of MB-CROW-OFDM

q	ξ	$f_c^{(1)}(Hz)$	$R^{NOL}(sym/sec)$	$R^{OL}(sym/sec)$	ρ^{NOL}	ρ^{OL}
1	9.6774e+005	5.1700e+009	2.9032e+006	2.9032e+007	0.1500	1.5000
2	7.9976e+005	5.1699e+009	3.0806e+006	1.5403e+007	0.1667	0.8333
3	7.1703e+005	5.1697e+009	3.1370e+006	1.0457e+007	0.1750	0.5833
4	6.6932e+005	5.1695e+009	3.1614e+006	7.9034e+006	0.1800	0.4500
6	6.1718e+005	5.1691e+009	3.1813e+006	5.3021e+006	0.1857	0.3095
8	5.8945e+005	5.1686e+009	3.1890e+006	3.9862e+006	0.1889	0.2361
10	5.7229e+005	5.1681e+009	3.1928e+006	3.1928e+006	0.1909	0.1909

6.3.1 Typical Channel Impulse Responses (CIR) for Simulations

Based on the Jakes' model, the impulse responses of 8 typical channels used in the simulations are calculated and notated as follows:

- CIR–1 - Stationary multipath channel ($Path_N = 3$, $v = 0$)
- CIR–2 - Stationary multipath channel ($Path_N = 16$, $v = 0$)
- CIR–3 - Doppler dispersive channel ($Path_N = 3$, $v = 20$ km/h, $f_c = 10$ MHz)
- CIR–4 - Doppler dispersive channel ($Path_N = 16$, $v = 20$ km/h, $f_c = 10$ MHz)
- CIR–5 - Doppler dispersive channel ($Path_N = 3$, $v = 60$ km/h, $f_c = 10$ MHz)
- CIR–6 - Doppler dispersive channel ($Path_N = 16$, $v = 60$ km/h, $f_c = 10$ MHz)
- CIR–7 - Doppler dispersive channel ($Path_N = 3$, $v = 120$ km/h, $f_c = 10$ MHz)
- CIR–8 - Doppler dispersive channel ($Path_N = 16$, $v = 120$ km/h, $f_c = 10$ MHz)

The corresponding amplitude and phase of the CIR, $h_n(t), n = 1, \cdots, 8$, are shown in Fig. 6.3. Note that the resolution of the path interval is the sampling period of the transmitted signal. In the following simulations, the path interval is set to be 50ns.

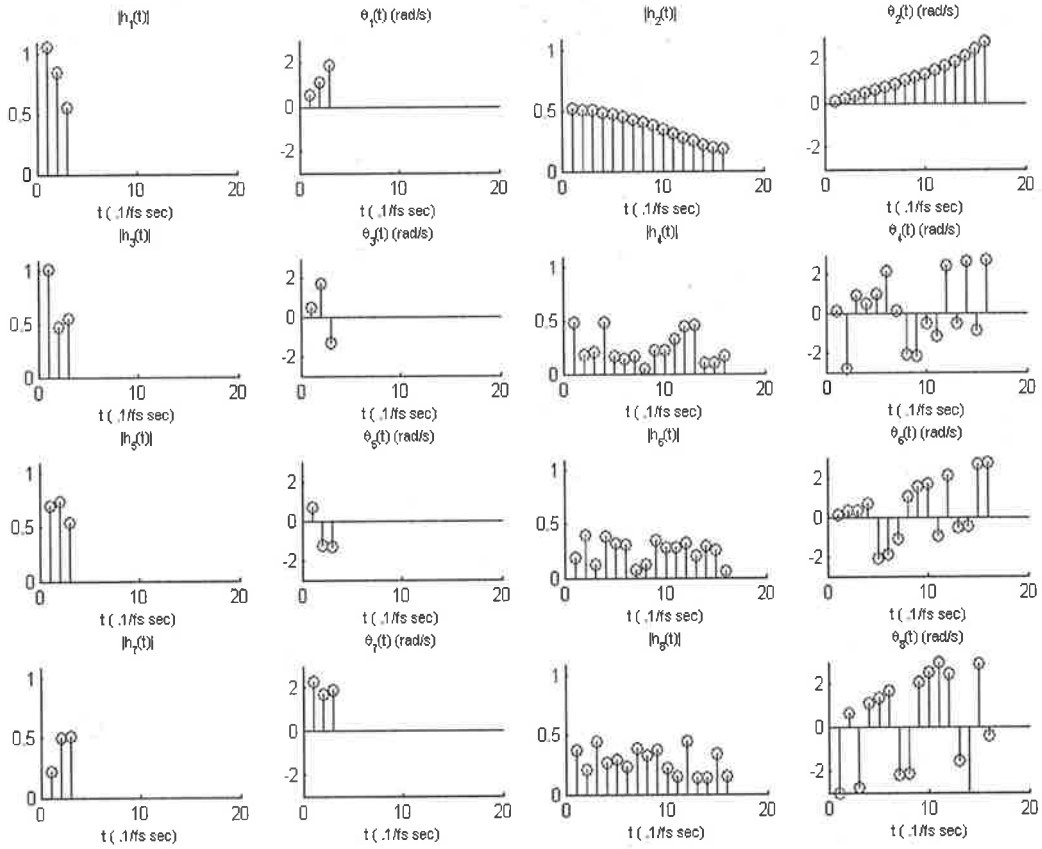

Figure 6.3. Impulse response of the 8 channels

6.3.2 BER Performance in Stationary Multipath Channels

We evaluate the BER performance of the DFT-OFDM and MB-CROW-OFDM in stationary multipath channels, CIR–1 and CIR–2. The BER performances of the two schemes in the AWGN channel are also evaluated for comparison purpose.

- **Case 1:** *DFT-OFDM with CP and without coding*

  The BER performance of DFT-OFDM is shown in Fig. 6.4.

  The CIR–1 and CIR–2 channels shown in Fig. 6.3 have the delay spread of 50 ns × 2 = 100 ns and 50 ns × 15 = 750 ns. Fig. 6.4 shows that as the delay spread approaches the length of CP (800 ns) that is 20% of the symbol length, the DFT-OFDM scheme suffers from severe performance degradation. Notice that 64-point

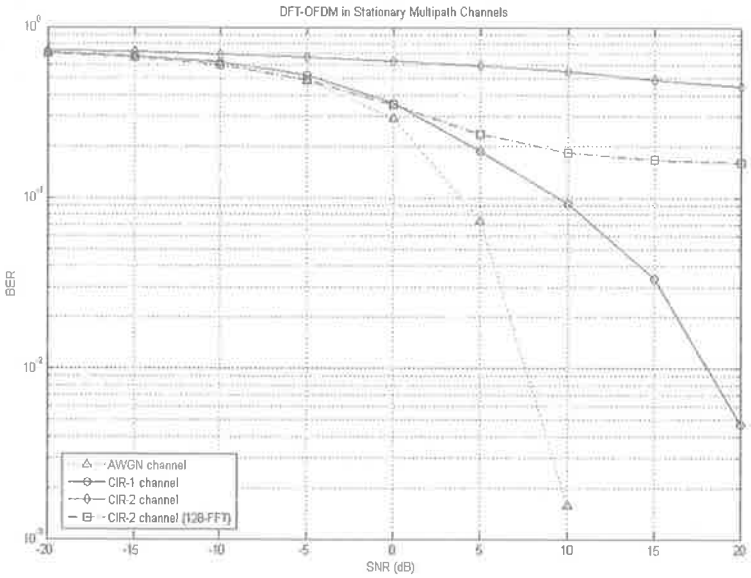

Figure 6.4. BER performance of DFT-OFDM scheme in multipath stationary channels (CIR–1 and CIR–2)

FFT is used in the simulation as specified in the standards. Theoretically, the DFT-OFDM could combat the multipath delay spread of the length of CP, however, the performance is affected by the resolution or the length of the FFT. At the cost of computational complexity, an FFT of 128-point or more will lead to better performance with the same length of CP because of its better resolution. For comparison, the BER of DFT-OFDM with 128-point FFT in the CIR–2 channel is also plotted in Fig. 6.4.

- **Case 2:** *MB-CROW-OFDM scheme, $q = 1$, 2-PAM/OOK*

  As illustrated in Fig. 6.1 and Fig. 6.2 in section 6.2, the MB-CROW-OFDM has nonuniform spectrum. For the MB-CROW-OFDM scheme with $q = 1$, the bandwidth difference is even greater than that of the MB-CROW-OFDM scheme with $q = 3$ as shown in Fig. 6.1. To illustrate the different transmission properties of the subchannels due to the nonuniform bandwidths, we plot the BER performance of the 4 subchannels comprising one subband, through an AWGN channel, in Fig. 6.5. It is apparent that the subchannel with narrower bandwidth has better BER performance due to its greater noise mitigation. For simplicity, we count the sum of

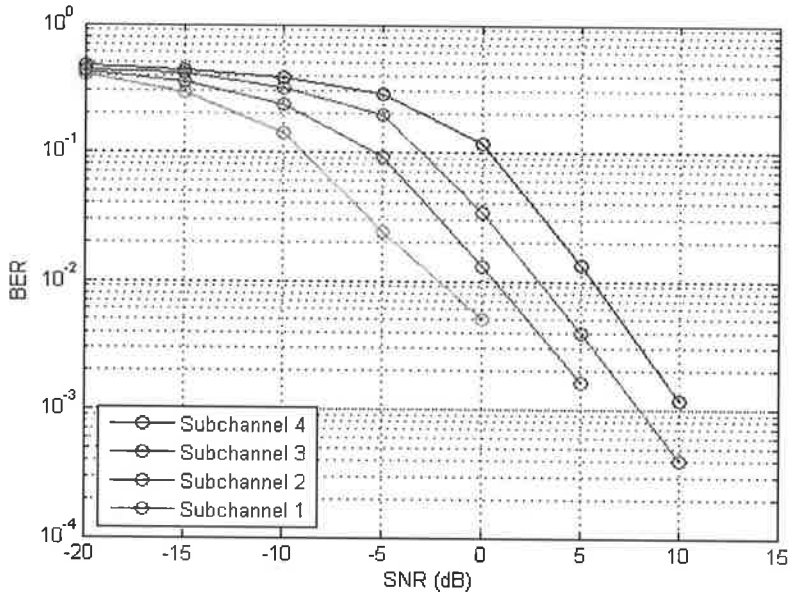

Figure 6.5. BER performance of MB-CROW-OFDM (q=1) in AWGN channel

symbols transmitted in all subchannels and only plot an average BER performance in the following simulations.

The BER performance of the MB-CROW-OFDM through the specified stationary channels is plotted in Fig. 6.6 that shows improved robustness against multipath compared to that of the DFT-OFDM as shown in Fig. 6.4. In addition, the SNR is 10 dB lower for the same BER because of its better noise mitigation performance based on good time-frequency localisation and orthogonality of the CROWs.

- **Case 3:** *MB-CROW-OFDM scheme, $q = 2$, QPSK*

The BER performance of the MB-CROW-OFDM through the specified stationary channels is plotted in Fig. 6.7.

It shows that the MB-CROW-OFDM with $q = 2$ has similar robustness against multipath as the MB-CROW-OFDM with $q = 1$. With good time-frequency localisation property, it has even better noise mitigation performance with about 15 dB improvement over the DFT-OFDM in case 1 and 5 dB improvement over the MB-CROW-OFDM in case 2 on the overall BER performance.

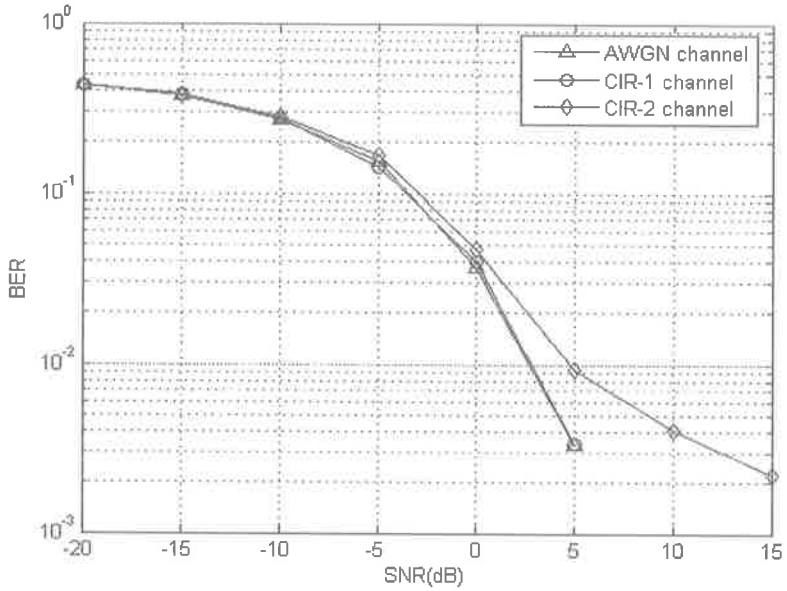

Figure 6.6. BER performance of MB-CROW-OFDM (q=1) in multipath stationary channels (CIR–1 and CIR–2)

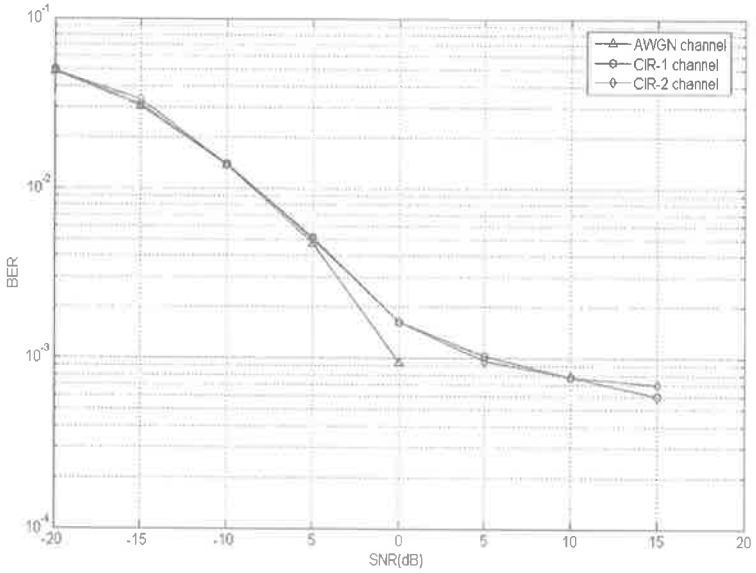

Figure 6.7. BER performance of MB-CROW-OFDM (q=2) in multipath stationary channels (CIR–1 and CIR–2)

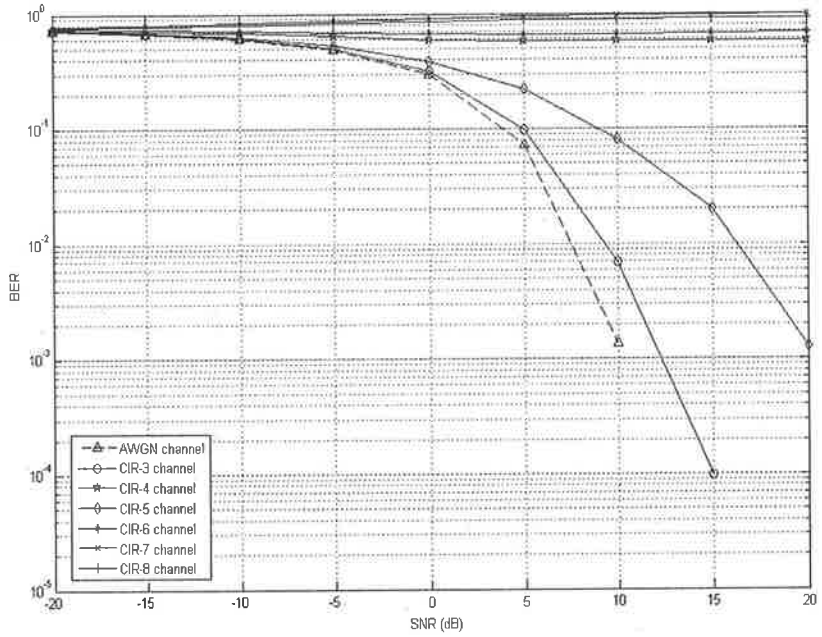

Figure 6.8. BER performance of DFT-OFDM (q=1) in Doppler dispersive channels (CIR–3 to CIR–8)

6.3.3 BER Performance in Doppler Dispersive Channels

We evaluate the BER performance of the DFT-OFDM and MB-CROW-OFDM in Doppler Dispersive Channels, denoted by CIR–3, $\cdots$, 8. Define the Doppler scale ratio by $\eta = v/c$, where v is the speed specified in section 6.3.1, and c is the speed of light. The calculated η is 1.85×10^{-8} for CIR–3 and CIR–4, 5.56×10^{-8} for CIR–5 and CIR–6, and 1.11×10^{-7} for CIR–7 and CIR–8.

- **Case 1:** *DFT-OFDM scheme with CP and without coding*

  The BER performance of DFT-OFDM through the 6 Doppler dispersive channels is shown in Fig. 6.8. For comparison, the BER performance in AWGN channel is also plotted in the same figure. The plot indicates that DFT-OFDM is very sensitive to Doppler and could only cope with the low speed of 20 km/h.

- **Case 2:** *MB-CROW-OFDM scheme, $q = 1$, 2-PAM/OOK*

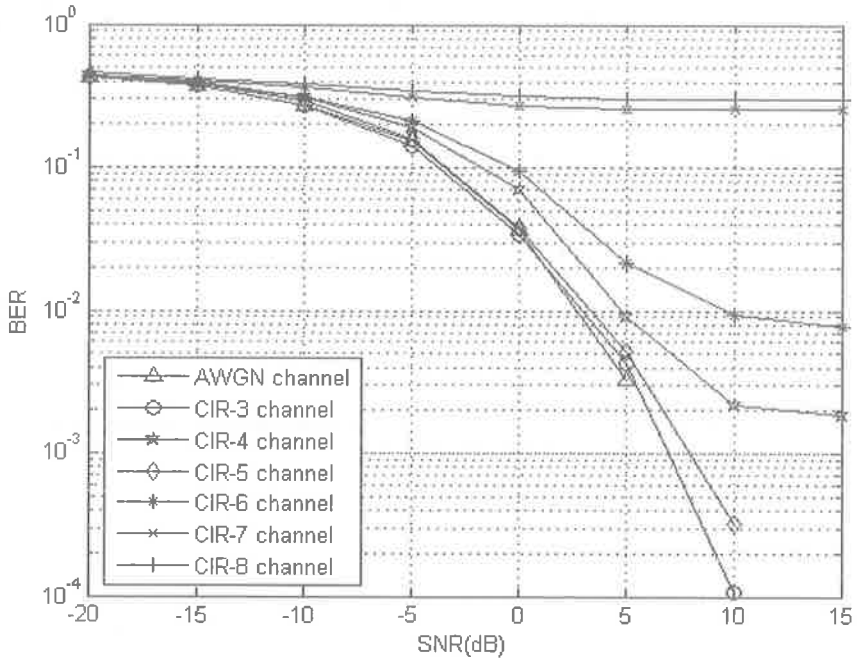

Figure 6.9. BER performance of MB-CROW-OFDM (q=1) in Doppler dispersive channels (CIR–3 to CIR–8)

The BER performance of the MB-CROW-OFDM through the 6 Doppler dispersive channels is plotted in Fig. 6.9. For comparison, the BER performance in AWGN channel is also plotted in the same figure.

Fig. 6.9 shows that the MB-CROW-OFDM scheme with $q = 1$ has much better Doppler robustness than the DFT-OFDM scheme. However, it can not cope with the vehicle speed of 120 km/h in CIR–7 and CIR–8 channels. To obtain more details, a plot of the BER performance of the 4 OFDM subchannels with different bandwidths in CIR–7 and CIR–8 channels is shown in Fig. 6.10 and Fig. 6.11. It indicates that for both channels, the subchannel with the narrowest bandwidth is still robust, however, the other 3 subchannels do not work because the Doppler dispersion has greater effect on the subcarrier waveforms because of its larger bandwidth. Combined with frequency selective fading, the CIR–8 with larger number of paths suffers from more ISI and has more degraded performance than CIR–7.

- **Case 3:** *MB-CROW-OFDM scheme, $q = 2$, QPSK*

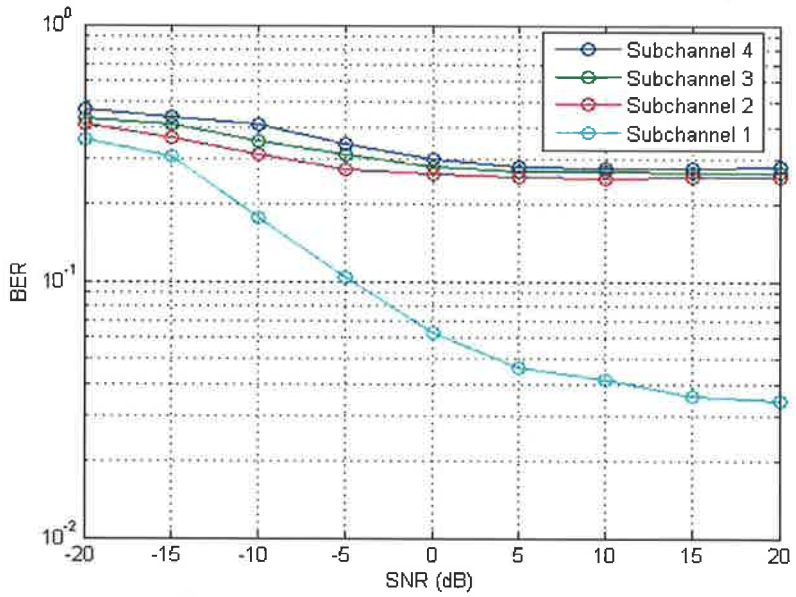

Figure 6.10. BER performance of 4 subchannels (q=1) in CIR7 channel

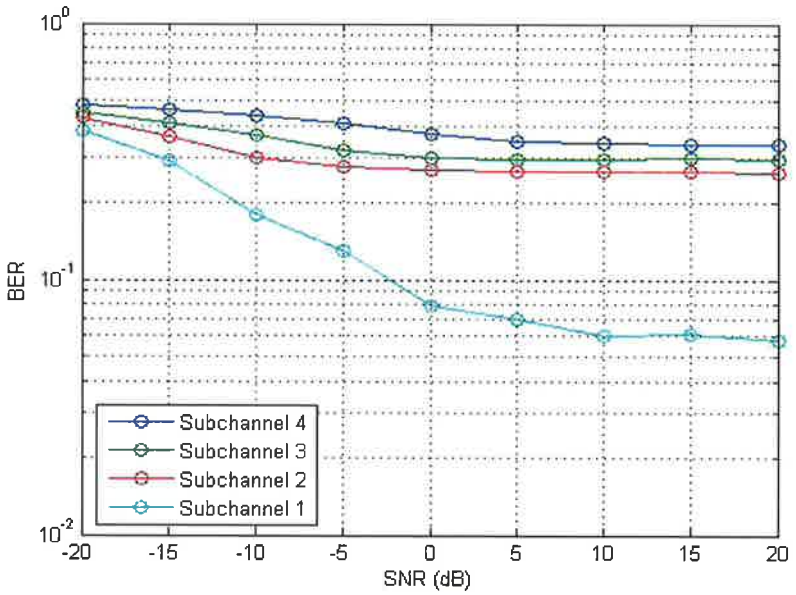

Figure 6.11. BER performance of subchannels (q=1) in CIR8 channel

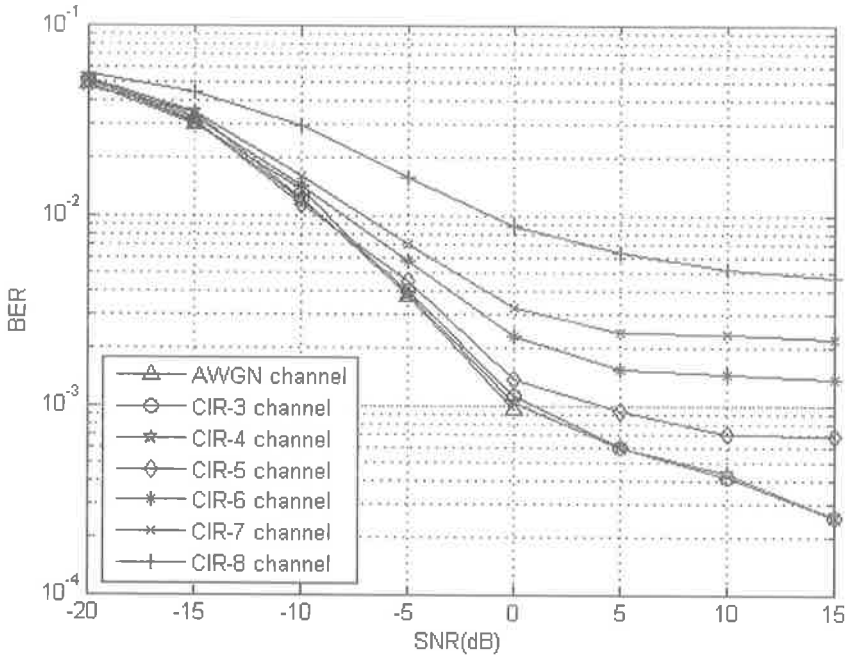

Figure 6.12. BER performance of MB-CROW-OFDM (q=2) in Doppler dispersive channels (CIR–3 to CIR–8)

The BER performance of MB-CROW-OFDM for channel CIR–3 to CIR–8 is shown in Fig. 6.12. The BER performance in AWGN channel is plotted for comparison.

As shown in Fig. 6.12, MB-CROW-OFDM with $q = 2$ has even better Doppler robustness than the MB-CROW-OFDM with $q = 1$ and work in the channels with significant Doppler scale ratio as in CIR–7 and CIR–8. This improvement is due to more uniform bandwidths of subchannels with a scale factor of 3/2 instead of 2. The difference between the bandwidths is less significant than in case 2, therefore the subchannel with the greatest bandwidth could still cope with the Doppler dispersion in CIR–7 and CIR–8.

6.4 Conclusions

The main contributions of this chapter are summarised in the following together with some remarks.

1) An MB-CROW-OFDM scheme is designed which is able to cope with the Doppler dispersion due to terminal motions particularly for mobile WLANs.

Current OFDM-based WLAN standards, e.g. IEEE 802.11.a/g, feature discrete Fourier transform (DFT)-based OFDM that provides high bandwidth efficiency but is very sensitive to Doppler dispersion. In comparison, the MB-CROW-OFDM scheme provides a solution of designing WLAN terminals that are more robust to multipath and Doppler dispersion. It could provide high bit rate that is comparable or higher than that in current standards, and can be utilised in a fully mobile outdoor environment as well as the stationary indoor environments. Based on the good time-frequency localisation and orthogonality of the CROWs that form the subcarriers of the CROW-OFDM scheme, significant noise mitigation performance is also achieved.

2) Explicit formulae are derived for the baseband MB-CROW-OFDM signal construction, and the calculation of the available symbol rate.

The design parameters for the MB-CROW-OFDM signal construction can be calculated based on the design formulae (6.1), (6.2), (6.3), (6.4) for both overlapped and non-overlapped signalling. A few design examples are given for the MB-CROW-OFDM with different q values. It is worth noting that for the CROW-OFDM scheme with $q > 2$, the shift-2 orthogonality of the CROWs (as demonstrated in section 2.4) can be utilised, which further increases the available symbol rates.

3) The BER performance of the MB-CROW-OFDM is analysed and compared with the DFT-OFDM specified in standards, for both stationary multipath and Doppler dispersive channels, using Jakes' Model.

For a comparison with the schemes in current WLAN standards, the simulation is set at the 5 GHz band with signal bandwidth of 20 MHz. However, the system analysis is based on baseband signal processing. Therefore, the extension is straightforward to the possible 5.9 GHz band specified in IEEE 802.11p standard. This standard is under development specifically for the communication between high-speed vehicles and between vehicles and the roadside infrastructure.

It is worth noting that for the MB-CROW-OFDM with higher q values, the bandwidths of subchannels become more uniform as shown in Fig. 6.2. Combined with good time-frequency localisation and orthogonality properties, it leads to the robustness of the scheme in time and frequency dispersive channels as shown in section 6.3.3. In addition, the MB-CROW-OFDM scheme can be simplified to the single band CROW-OFDM with one tree structured synthesis FB in the transmitter and analysis FB in the receiver. However, higher q values lead to longer synthesis/analysis filter lengths in the FB branches, and thus increase the computational complexity.

We summarise the specifications of simulated DFT-OFDM and MB-CROW-OFDM in the following table.

Table 6.2. Comparison of specifications for DFT-OFDM and MB-CROW-OFDM

Scheme	DFT-OFDM with GI	MB-CROW-OFDM
BW (MHz)	20	20
Number of Subcarriers	52 (48 data, 4 pilot subcarriers)	64
Modulation	M-PSK	M-PAM(q=1); M-PSK(q>1)
Symbol Rate (Msps)	12	NOL: 2.90 (q=1); 3.08 (q=2) OL: 29.04 (q=1); 15.41 (q=2)
Bandwidth Efficiency	0.6	NOL: 0.15 (q=1); 0.15 (q=2) OL: 1.54 (q=1); 0.77 (q=2)
Computational Complexity	$O(N \log N)$ (FFT)	$O(N)$ (FWT)
Uniform Bandwidth	Yes	No
Synchronisation Requirement	High	Low
Sensitivity to Analog Carrier Offset	Yes	Yes
Multipath Robustness	Good (Delay Spread < GI)	Good
Doppler Robustness	Poor	Good

Chapter 7

Conclusions

7.1 Summary of Main Contributions

The main contributions of the thesis are summarised as follows.

Chapter 2: Real and Complex Rational Orthogonal Wavelets

- Explicit formulae (2.11), (2.12) were derived for a special class of RROWs with rational dilation factor of $a = \frac{q+1}{q}$, which has good time-frequency localisation property desirable for communication applications.
- The time-frequency localisation property of the RROWs was analysed.
- A theoretical proof was given for the argument that the Hilbert transform of one wavelet forms another wavelet from the MRA point of view.
- A generalised method was proposed to construct complex wavelets under the framework of rational MRA(M), where M is a rational number.
- A new family of complex wavelets - CROWs was proposed which form a complex MRA approximately.
- Time-domain FWT algorithms were derived for RROWs and CROWs.
- A generalised solution was proposed for the design of rational sampling FB with good PR and SI properties based on the tree-structured FWT FB.

Chapter 3: CROW-based Orthogonal Frequency Division Multiplexing

- A new OFDM scheme was proposed based on the CROWs proposed in chapter 2.
- The PSD and bandwidth efficiency of the CROW-OFDM scheme were analysed, which revealed that a special case of CROW-OFDM with $q = 1$, achieves significant improvement on bandwidth efficiency that reaches 1.5 times the 'maximum' value 1 symbol/Hz/s achieved by discrete Fourier transform (DFT) based OFDM without cyclic prefix (CP).
- The CROW-OFDM transceiver was designed based on the FWT FB proposed in chapter 2.

Chapter 4: CROW's Application to Underwater Acoustic Communications

- A transmultiplexer system model was proposed based on wavelet pulse signaling in the transmitter to characterize a multipath/Doppler channel and the recovery of Doppler compensated signal based on perfect reconstruction (PR) wavelet filter banks (FBs).
- It was demonstrated in this chapter that the transmultiplexer structure for broadband Doppler compensation is equivalent to an L-th order diversity system, which forms the basis of the optimum receiver design.
- Optimum receivers were designed for the proposed system structure based on the maximum likelihood (ML) criterion. Two types of receivers were designed. Compared with the type 1 receiver which is based on the traditional optimal correlation/matched filtering demodulators, the type 2 receiver with modified demodulation structure is superior with its robustness against severe time synchronisation error.
- Theoretical derivation of the probability of error for the two receivers was given together with supporting Monte Carlo simulations.
- The tradeoff between system parameters was discussed, and the corresponding evaluation formulae were derived so that we have full control of the system performance by selecting the parameters to suit specific communication scenarios.

Chapter 5: CROW's Application to UWB IR Communications

- The PSK modulation was proposed for UWB IR communications based on complex UWB pulses.
- Two classes of complex UWB pulses were proposed based on complex Gaussian wavelets and the CROWs respectively. Formulae in closed form (5.9), (5.21) were derived for a full control of the time and frequency properties of the designed UWB pulses.
- A novel PSK demodulator was proposed based on complex wavelet signalling which has unique robustness against timing jitter.

Chapter 6: CROW's Application to Radio Vehicular Communications

- An MB-CROW-OFDM scheme was designed which is able to cope with the Doppler dispersion due to terminal motions particularly for mobile WLANs [36].
- Explicit formulae (6.1), (6.2), (6.3), (6.4) were derived for the baseband MB-CROW-OFDM signal construction, and the calculation of the available symbol rate.
- The BER performance of the MB-CROW-OFDM was analysed and compared with the DFT-OFDM specified in standards, for both stationary multipath and Doppler dispersive channels using Jakes' Model.

7.2 Reflections on Future Work

The work in this thesis leads to the extension to the following topics that are left for the future work.

1) Construction of Complex Wavelets Under the Framework of Rational MRA and Rational Wavelet FBs

In chapter 2, we proposed a generalised method to construct complex wavelets whose real and imaginary parts form a Hilbert transform pair. An orthogonal condition on the spectrum of the real part of the wavelet was derived. The proposed CROWs satisfy the

condition not exactly but with high fidelity and form an approximate complex MRA. One of the wavelets that form the exact complex MRA is the Littlewood-Parley wavelet [16], while finding other appropriate wavelets under the exact orthogonal condition is still an open problem. In addition, finding the equivalent orthogonality condition under the framework of rational wavelet FBs is also an interesting issue and requires more investigation.

2) Broadband UWA Doppler Compensation and Multichannel Equalisation Design Based on a Physical Raytracing Model

In chapter 4, the proposed Doppler compensation scheme is based on a theoretical multipath/Doppler channel model. Notice that to focus on the resolution of the multi-scale nature of multipath/Doppler channels, we assume a slow fading frequency-selective multipath/Doppler channel which can be resolved into multiple nearly ideal flat fading subchannels, that is, the attenuation and delay coefficients for each multipath are constant for certain subchannels as shown in equation

$$h(\tau) = \sum_{\ell=1}^{L} \rho_\ell \delta(\tau - \tau_\ell). \tag{7.1}$$

The designed receiver structure can also be extended to suit more general fast fading/time-variant channel conditions where the channel impulse response can be expressed as

$$h(t, \tau) = \sum_{\ell=1}^{L} \rho_\ell(t) \delta(\tau - \tau_\ell(t)). \tag{7.2}$$

A multiple-equaliser structure with each equaliser adaptive to the impulse response of each subchannel that has been resolved by the designed receiver structure, can be implemented straightforwardly to address the frequency selective slow/fast fading of the subchannels. It has been demonstrated by existing researches [73] that the multiple subchannel equalisers outperform the single channel equaliser in many aspects.

More detailed analysis of the proposed Doppler compensation scheme based on the physical UWA channel and taking account of the time-variance of the channel and multichannel equalisation design in the receiver is worth more research effort.

3) Peak-to-Average-Power-Ratio (PAPR) Reduction of the CROW-OFDM signal

A common problem in multicarrier modulation systems is the possibility of high peaks in transmitted signals, known as the high PAPR. As reported in [26], wavelet based orthogonal frequency division modulation or OWDM, has the PAPR that is equal to that of DFT-based OFDM system. There are many existing techniques to reduce the PAPR of a multicarrier modulation system, e.g. the clipping/filtering methods [28], [29], [11], coding based techniques [10], [33], [41], [85], [43], phase rotation based techniques including the partial transmit sequences (PTS) based techniques [58], [24], [37], [50] and selected mapping (SLM) [87], [15], as well as combined coding, clipping and/or phase rotation methods [20], [9]. Generally, these techniques are applicable directly to improve the PAPR of the proposed CROW-OFDM scheme in the thesis, however, a detailed examination of this issue for a specific CROW-OFDM system would be worthwhile.

4) Combined PSK and PPM Modulation Schemes Based on Complex UWB Pulses

Besides the inherent advantages of PSK modulation which lead to high power efficiency and high data rate, the proposed PSK scheme in the UWB communication context provides a more flexible way to construct new modulation schemes, such as combined PSK and PPM modulation and combined PSK, PAM and PPM modulation, which are able to take advantage of the benefits of different modulation schemes and achieve an optimal tradeoff to suit a specific application.

The detailed comparison with other modulation options and new combined modulation schemes is worth investigation addressing the analysis on BER performance versus timing jitter and SNR, signal bandwidth efficiency, power efficiency and tradeoffs of the system performance.

5) CROW-based Multiband (MB) UWB OFDM Systems with Doppler Robustness

Multiband (MB) UWB OFDM systems play an important role in UWB communications [32], [57], [72], [71]. In chapter 5, we discussed the construction of MB UWB based on the combination of complex UWB pulses relatively longer than the conventional pulse length. Notice that it is a direct extension of the UWB IR scheme based on non-modulated baseband design. The groundwork in chapter 3 on the CROW-based OFDM provides a

more flexible solution to construct MB UWB OFDM systems based on modulated CROW wavelet pulses.

The performance analysis of the CROW-based MB UWB OFDM scheme based on the UWB channel models worths more efforts.

6) Optimal Resource Allocation for CROW-OFDM Based Mobile WLANs

As a wavelet-based OFDM scheme, CROW-OFDM has an important feature that is the non-uniform bandwidths of the subchannels. This feature facilitates the implementation of multi-rate transmission for multiple services with different data rate requirements. Compared with the uniform bandwidth structure of the DFT-OFDM scheme in the current standards, it generates new design of resource allocation techniques based on the non-uniform subchannel bandwidths. More investigation on the optimal resource allocation algorithm and the possible cross layer design solutions for the CROW-OFDM mobile WLANs would be required.

7) Double Single-Sidebanded CROW-OFDM Modulation

Notice that the proposed CROW-OFDM scheme is based on the complex wavelet baseband subcarriers and combined with sinusoidal modulation to move the baseband spectrum to the required bandwidth. The information of the transmitted symbols is carried by the phase of the CROW-based subcarriers. By utilising the sinusoidal carriers as well to carry phase information as in the conventional OFDM scheme, it leads to another dimension of freedom in orthogonal division multiplexing and achieves higher data rates. It could be termed as a Double Single-Sidebanded CROW-OFDM scheme in light of its spectrum features. A systematic analysis of this scheme under various channel conditions would be interesting.

Appendix A

Appendices for Chapter 2

A.1 Proof of Theorem 2

The proof of Theorem 2 proposed in section 2.4 is given as follows.

Proof: The proof of the theorem is equivalent to the verification of the two claims in section 2.4 in regard to the conditions in Definition 1. The proof of (iv) in Definition 1 for claim 1) is independent of the choice of a and reduces to the following identity

$$\sum_{k\in\mathbb{Z}} |\hat{\Phi}(\omega + 2k\pi)|^2 = 1, \ \omega \in \mathbb{R}. \tag{A.1}$$

Since we have $|\hat{\Phi}(\omega)| = |\Phi(\omega)|$ and $\sum_{k\in\mathbb{Z}} |\Phi(\omega+2k\pi)|^2 = 1$, the verification is immediate. The proof of (i) in definition 1 is as follows: Since $V_j \subset V_{j+1}$, we have

$$\phi_{j,n}(t) = \sum_{k\in\mathbb{Z}} b_{n,k}\phi_{j+1,k}(t), \ n = 0, 1, \cdots, q-1, \tag{A.2}$$

as shown in [16], which is equivalent to

$$\Phi(a^{-j}\omega) = a^{-\frac{1}{2}} \sum_{k\in\mathbb{Z}} b_{n,k} e^{-ika^{-(j+1)}\omega} e^{-ina^{-j}\omega} \Phi(a^{-(j+1)}\omega) \tag{A.3}$$

for some $\{b_{n,k}\} \in \ell_2$. From the definition of Hilbert transform, we have $\hat{\Phi}(\omega) = -j\text{sgn}(\omega)\Phi(\omega)$, where the Sgn function sgn(.) returns the sign of number ω. Therefore we have the relation

that

$$\begin{aligned}\hat{\Phi}(a^{-j}\omega) &= a^{-\frac{1}{2}}\sum_{k\in\mathbb{Z}} b_{n,k}e^{-ika^{-(j+1)}\omega}e^{-ina^{-j}\omega}(-i)\mathrm{sgn}(\omega)\Phi(a^{-(j+1)}\omega) \\ &= a^{-\frac{1}{2}}\sum_{k\in\mathbb{Z}} b_{n,k}e^{-ika^{-(j+1)}\omega}e^{-ina^{-j}\omega}\hat{\Phi}(a^{-(j+1)}\omega). \qquad \text{(A.4)}\end{aligned}$$

This proves $\hat{V}_j \subset \hat{V}_{j+1}$. The verification of ii) and iii) is immediate with the proof of i) and iv).

The proof of claim 2) consists of 3 points:

1. the orthonormality of $\hat{\psi}(t)$ that the set $\{\hat{\psi}(t-kq),\ k\in\mathbb{Z}\}$ forms an orthonormal basis for $\hat{W}_0$.
2. $\hat{W}_j \subset \hat{V}_{j+1},\ j\in\mathbb{Z}$.
3. $\hat{W}_j \perp \hat{V}_j,\ j\in\mathbb{Z}$.

Firstly, since we have the orthonormality of $\psi(t)$ that $\sum_k |\Psi(\omega+2kq\pi)|^2 = 1$ and there is $|\hat{\Psi}(\omega)| = |\Psi(\omega)|$, it follows that $\sum_k |\hat{\Psi}(\omega+2kq\pi)|^2 = 1$ which proves the first point. For the proof of the second point, it is similar to the proof of $\hat{V}_j \subset \hat{V}_{j+1}$. Since we have $W_j \subset V_{j+1}$ which gives us the relation $\Psi(a^{-j}\omega) = \sum_{k\in\mathbb{Z}} d_k e^{-ik\omega}\Phi(a^{-(j+1)}\omega)$, the Hilbert transform of $\Psi(a^{-j}\omega)$ can be expressed as

$$\hat{\Psi}(a^{-j}\omega) = \sum_{k\in\mathbb{Z}} d_k e^{-ik\omega}\hat{\Phi}(a^{-(j+1)}\omega). \qquad \text{(A.5)}$$

This proves $\hat{W}_j \subset \hat{V}_{j+1}$. For the third point, by the Parseval formula, the orthogonality of $\hat{W}_j$ to $\hat{V}_j$ is equivalent to requiring that

$$\hat{I}_\ell = \int_{\mathbb{R}} \hat{\Psi}(\omega)\hat{\Phi}^*(\omega)e^{-i\ell\omega}d\omega = 0. \qquad \text{(A.6)}$$

(A.6) can be derived directly from the condition that $W_j \perp V_j$ which has the relation

$$I_\ell = \int_{\mathbb{R}} \Psi(\omega)\Phi^*(\omega)e^{-i\ell\omega}d\omega = 0, \qquad \text{(A.7)}$$

and therefore

$$\begin{aligned}\hat{I}_\ell &= \int_{\mathbb{R}} (-i)\,\mathrm{sgn}(\omega)\Psi(\omega)i\,\mathrm{sgn}(\omega)\Phi^*(\omega)e^{-i\ell\omega}d\omega \\ &= I_\ell \\ &= 0. \qquad \text{(A.8)}\end{aligned}$$

A.2 Definitions of R-function, Riesz Basis, R-wavelets and Frames

A brief review of the definitions of R-function, Riesz Basis, R-wavelets and Frames are given in the following. Readers are referred to Chui's [22] for more details.

R-function: A function $\psi \in L^2(\mathbb{R})$ is called an R-function if $\psi_{j,k}$ defined by $\psi_{j,k} := 2^{j/2}\psi(2^j x - k),\ j,k \in \mathbb{Z}$, is a Riesz basis of $L^2(\mathbb{R})$.

Riesz basis: A set of functions $\{\psi_{j,k},\ j,k \in \mathbb{Z}\}$ is a Riesz basis of $L^2(\mathbb{R})$ if the linear span of $\psi_{j,k},\ j,k \in \mathbb{Z}$ is dense in $L^2(\mathbb{R})$ and the positive constants A and B exist, with $0 < A \leq B < \infty$, such that

$$A\|\{C_{j,k}\}\|_{l^2}^2 \leq \| \sum_{j=-\infty}^{\infty} \sum_{k=-\infty}^{\infty} C_{j,k}\psi_{j,k}\|_{l^2}^2 \leq B\|\{C_{j,k}\}\|_{l^2}^2, \tag{A.9}$$

for all doubly bi-infinite square-summable sequences $\{C_{j,k}\}$ that is

$$\|\{C_{j,k}\}\|_{l^2}^2 := \sum_{j=-\infty}^{\infty} \sum_{k=-\infty}^{\infty} |C_{j,k}|^2 < \infty. \tag{A.10}$$

R-wavelet: An R-function $\psi \in L^2(\mathbb{R})$ is called an R-wavelet (or wavelet) if there exists a function $\tilde{\psi} \in L^2(\mathbb{R})$, such that $\{\psi_{j,k}\}$ and $\{\tilde{\psi}_{j,k}\}$ are a dual basis of $L^2(\mathbb{R})$ in the sense that

$$< \psi_{j,k}, \tilde{\psi}_{l,m} > = \delta_{j-l}\delta_{k-m},\ j,k,l,m \in \mathbb{Z}, \tag{A.11}$$

where the inner product $< \cdot, \cdot >$ is defined by

$$< f, g >:= \int_{-\infty}^{\infty} f(x)\overline{g(x)}dx, \tag{A.12}$$

$\overline{g(x)}$ is the complex conjugate of $g(x)$, and $\delta_n,\ n \in \mathbb{Z}$ is the Kronecker Delta function defined by

$$\delta_n := \begin{cases} 0, & n \neq 0 \\ 1, & n = 0. \end{cases} \tag{A.13}$$

Frames: A function $\psi \in L^2(\mathbb{R})$ is said to generate a frame $\psi_{b_0;j,k}$ of $L^2(\mathbb{R})$, if the condition holds that,

$$A\|f\|_2^2 \leq \sum_{j,k\in\mathbb{Z}} |< f, \psi_{b_0;j,k} >|^2 \leq B\|f\|_2^2, \ f \in L^2(\mathbb{R}), \tag{A.14}$$

where

$$\psi_{b_0;j,k} := 2^{j/2}\psi(2^j t - kb_0), \tag{A.15}$$

and b_0 is a fixed constant called "sampling rate". The norm $\|f\|_2$ is defined by

$$\|f\|_2 := \left\{ \int_{-\infty}^{\infty} |f(x)|^2 \, dx \right\}^{\frac{1}{2}}. \tag{A.16}$$

A, B are called the frame bounds. If $A = B$, the frame is called a tight frame.

A.3 Derivation of Shift-2 Orthogonality of CROWs

Following the orthogonality condition of the CROWs in section 2.4 and the derivation of the constraint on the spectrum of $\psi(t)$ as

$$R_1 = \Im\left[\int_0^{\infty} \Psi(a^k\omega)\Psi^*(\omega) e^{-i\omega q(a^k n - m)} d\omega \right] = 0, \ k, n, m \in \mathbb{Z}, \tag{A.17}$$

the shift-2 orthogonality leads to the condition formulated by

$$R_2 = \Im\left[\int_0^{\infty} \Psi(a^k\omega)\Psi^*(\omega) e^{-2i\omega(a^k n - m)} d\omega \right] = 0, \ k, n, m \in \mathbb{Z}, \tag{A.18}$$

where $\Im[\cdot]$ returns the imaginary part of a complex signal. The condition (A.18) is equivalent to the condition (A.17) and holds exactly when $|k| \geq 2$ due to the compact support and non-overlapped spectra of the CROW wavelet basis functions in subspaces W_j and $\{W_{j+k}, \ |k| \geq 2\}$.

In the case when $k = \pm 1$, the term $\Psi(a\omega)\Psi^*(\omega)$ forms the overlapped spectrum of the two wavelet basis functions in two neighboring subspaces. It has a very small value in the frequency domain and leads to small values of R_1 and R_2 after multiplying with any sinusoidal signals ($e^{-i\omega q(a^k n - m)}$ for R_1 and $e^{-2i\omega(a^k n - m)}$ for R_2).

In the case when $k = 0$, there are

$$R_1 = \Im\left[\int_{\omega_1}^{\omega_1 + 2\pi} |\Psi(\omega)|^2 e^{-i\omega q n} d\omega \right], \ n \in \mathbb{Z}, \tag{A.19}$$

and

$$R_2 = \Im\left[\int_{\omega_1}^{\omega_1+2\pi} |\Psi(\omega)|^2 e^{-2i\omega n} d\omega\right], \; n \in \mathbb{Z}, \tag{A.20}$$

where ω_1 is defined in (2.13). For Littlewood Paley wavelet [16], there is $|\Psi(\omega)| = 1$, $\omega_1 \leq |\omega| \leq \omega_1 + 2\pi$. Therefore,

$$R_1 = \Im\left[\int_{\omega_1}^{\omega_1+2\pi} e^{-i\omega q n} d\omega\right] = 0, \; n \in \mathbb{Z}. \tag{A.21}$$

For the CROWs defined in 2.12, when q gets larger, the spectrum of $\Psi(\omega)$ gets more symmetric and leads to a very small integral R_1 when $|\Psi(\omega)|^2$ is multiplied by the sinusoidal signal $e^{-i\omega qn}$, $q \geq 2$, which is related to the shift-q orthogonality of the CROWs. Moreover, for all q values, very small integrals R_2 defined in (A.20) are achieved when $|\Psi(\omega)|^2$ is multiplied by sinusoidal signals $e^{-i\omega rn}$, $r \geq 2$, which leads to the shift-2 orthogonality with $r = 2$.

An analytic evaluation of R_1 by calculating

$$R_{k,n} =< \psi(a^k t), \hat{\psi}(t - nq) > \tag{A.22}$$

is shown in Fig. 2.10, which illustrates good approximation of the orthogonality condition for the CROWs. Similarly, an evaluation of

$$R_{k,n} =< \psi(a^k t), \hat{\psi}(t - 2n) > \tag{A.23}$$

shown in Fig. A.1 illustrates that the shift-2 orthogonality holds with high fidelity.

A.4 Derivation of Simplified RROW Analysis FB

We start from the direct rational sampling FB design method in [47]. The filters in the equivalent q-channel analysis FB are defined by

$$H_i'(z) = z^{d_i} H_{t_i}^{(v)}(z), \tag{A.24}$$

where $d_i = \lfloor p \cdot i/q \rfloor$ ($\lfloor x \rfloor$ denotes the largest integer not greater than x), $t_i = p \cdot i \bmod q$ and $H_0^{(v)}$, ..., $H_{q-1}^{(v)}$ are the polyphase components of H with respect to q. Considering the special case of $p = q + 1$, the definition is equivalent to

$$H_i'(z) = z^i H_i^{(v)}(z), \tag{A.25}$$

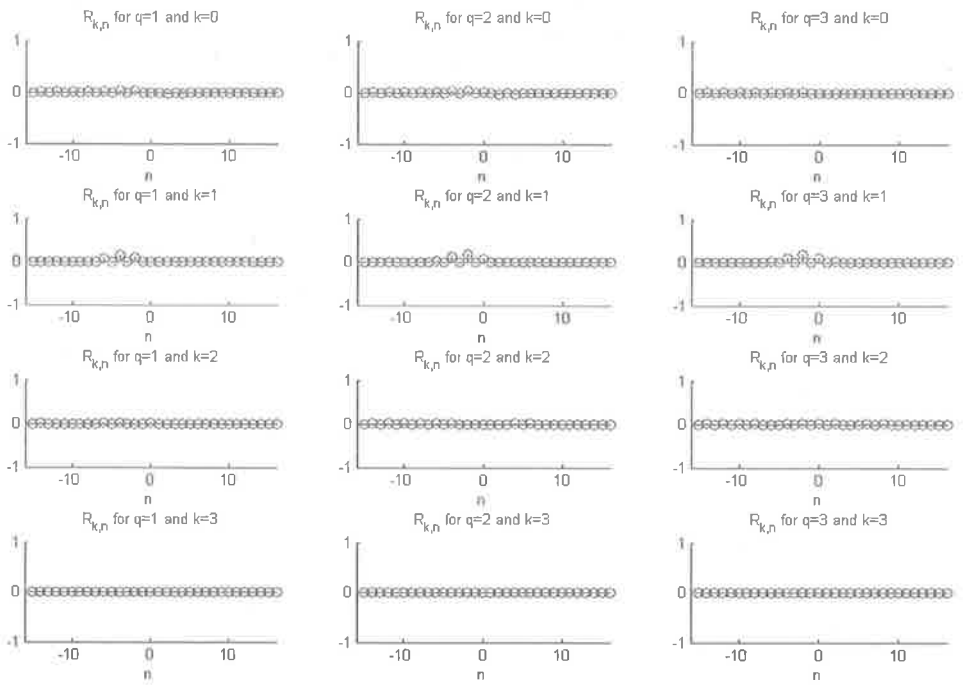

Figure A.1. Cross correlation of the scaled and shifted wavelet basis functions by integer 2.

where $i = 0, \cdots, q-1$. The polyphase expression of the equivalent filter H in the single branch is

$$H(z) = H_0^{(v)}(z^q) + z^{-1}H_1^{(v)}(z^q) + \cdots + z^{q-1}H_{q-1}^{(v)}(z^q). \tag{A.26}$$

The resemblance of the FBs in Fig. 2.11 and Fig. 2.15 infers the relation that

$$\tilde{H}_i(z) = z^i \tilde{H}_i^{(v)}(z), \tag{A.27}$$

where $\tilde{H}_i(z), i = 0, \cdots, q-1$ are the filters in the rational orthogonal analysis FB in Fig. 2.11. $\tilde{H}_i^{(v)}(z), i = 0, \cdots, q-1$ are the polyphase components of $\tilde{H}$ with respect to q. $\tilde{H}$ is the equivalent single branch filter we seek, and can be expressed by

$$\tilde{H}(z) = \tilde{H}_0^{(v)}(z^q) + z^{-1}\tilde{H}_1^{(v)}(z^q) + \cdots + z^{q-1}\tilde{H}_{q-1}^{(v)}(z^q). \tag{A.28}$$

Based on the definition of $\tilde{H}_i(z)$ in equation 2.21, we have

$$\tilde{H}_i(z) = z^{-ai}\tilde{H}_0(z), \ i = 0, \cdots, q-1. \tag{A.29}$$

Substituting (A.29) and (A.28) into (A.28), we have

$$\tilde{H}(z) = \tilde{H}_0(z^q) + z^{-(1+p+q)}\tilde{H}_0(z^q) + \cdots + z^{-(q-1)(1+p+q)}\tilde{H}_0(z^q). \tag{A.30}$$

Defining $A(z) = 1 + z^{-1} + z^{-2} + \cdots + z^{-(q-1)}$, the equivalent filter $\tilde{H}$ is expressed as

$$\tilde{H}(z) = A(z^{(1+p+q)})\tilde{H}_0(z^q). \tag{A.31}$$

This page is blank

Appendix B

Appendices for Chapter 4

B.1 Derivation of Probability of Error P_M for the Type-1 Receiver

The output noise variable is a Gaussian random variable with zero mean and variance

$$\sigma^2 = \frac{1}{2} N_0 \sum_{\ell=1}^{L} a^{-\alpha_\ell}. \tag{B.1}$$

Assume that all amplitude levels are equally likely *a priori.* the average probability of a symbol error is the probability that the noise variable exceeds in magnitude one-half of the distance between the received signal levels which is valued at

$$d^{(\frac{1}{2}e)} = d\sqrt{\varepsilon_g} \sum_{\ell=1}^{L} \rho_\ell. \tag{B.2}$$

Taking account of the fact that when either one of the two outside levels is transmitted, an error can occur in one direction only, and so we have

$$P_M = \frac{M-1}{M} \frac{2}{\sqrt{2\pi}\sigma} \int_{d\sqrt{\varepsilon_g}\sum_{\ell=1}^{L}\rho_\ell}^{\infty} e^{-\frac{x^2}{2\sigma^2}} dx. \tag{B.3}$$

By substituting (B.1) into equation (B.3), we have

$$\begin{aligned} P_M &= \frac{M-1}{M} \frac{2}{\sqrt{2\pi}} \int_{\frac{d\sqrt{\varepsilon_g}\sum_{\ell=1}^{L}\rho_\ell}{\sqrt{\frac{1}{2}N_0\sum_{\ell=1}^{L}a^{-\alpha_\ell}}}}^{\infty} e^{-x^2/2} dx \\ &= \frac{2(M-1)}{M} Q\left(\sqrt{\frac{2d^2\varepsilon_g(\sum_{\ell=1}^{L}\rho_\ell)^2}{N_0\sum_{\ell=1}^{L}a^{-\alpha_\ell}}}\right). \end{aligned} \tag{B.4}$$

B.2 Derivation of Probability of Error P_M for the Type-2 Receiver

The output noise random variable for the subchannel with Doppler scale of a^{α_ℓ} can be expressed as

$$Y = \sum_{i=1}^{N_\ell} |X_i|, \tag{B.5}$$

where N_ℓ is the filter length and X_i is a generalised Rayleigh distributed random variable with 1 degree of freedom whose probability density function (PDF) is

$$P(x) = \frac{2}{\sqrt{2\pi}\sigma} e^{-x^2/2\sigma^2}, x \geq 0 \tag{B.6}$$

The output noise variable Y can be rewritten as $Y = |X'|$ where X' is a Gaussian random variable with zero mean and variance $N_\ell\sigma^2$. Notice that to calculate the tail probability for the type 2 receiver, although the cumulative distribution function (CDF) is single-sided, the PDF of noise is two times the PDF of noise for the type 1 receiver on the positive side. Therefore for the same noise threshold, the CDFs are equivalent. The probability of error for the type 2 receiver follows the same derivation for the type 1 receiver by substituting the output noise component and signal component of the type 2 receiver.

The output noise variable is equivalent to a Gaussian random variable with zero mean and variance

$$\sigma^2 = \frac{1}{2} N_0 \sum_{\ell=1}^{L} a^{-3\alpha_\ell} N_\ell. \tag{B.7}$$

The one-half of the distance between the signal levels is given by

$$d^{(\frac{1}{2}e)} = d\sqrt{\varepsilon_g} \sum_{\ell=1}^{L} |\rho_\ell| \mu_0. \tag{B.8}$$

Analogously to the derivation of (B.4) from (B.2), we have the probability of error P_M given from (B.8) as

$$P_M = \frac{2(M-1)}{M} Q\left(\sqrt{\frac{2d^2\varepsilon_g (\sum_{\ell=1}^{L} |\rho_\ell|)^2 \mu_0^2}{N_0 \sum_{\ell=1}^{L} a^{-3\alpha_\ell} N_\ell}} \right). \tag{B.9}$$

Bibliography

[1] IEEE 802.11a-1999(r2003), part 11: Wireless LAN medium access control (MAC) and physical layer (PHY) specifications: High-speed physical layer in the 5 GHz band. *http://standards.ieee.org/getieee802/download/802.11a-1999.pdf*, Jun 2003.

[2] Complex Gaussian wavelets. *http://www.mathworks.co.kr/access/helpdesk/help/toolbox/wavelet/ch06_a40.html*, Aug 2006.

[3] Introduction to IEEE 802.20. *http://en.wikipedia.org/wiki/IEEE_802.20*, Aug 2006.

[4] Status of project IEEE 802.11p. *http://grouper.ieee.org/groups/802/11/Reports/tgp_update.htm*, Aug 2006.

[5] IEEE 802.11 WLAN standards. *http://grouper.ieee.org/groups/802/11/*, Aug 2006.

[6] IEEE 802.16 broadband wireless access standards. *http://www.ieee802.org/16/*, Aug 2006.

[7] M. Abdel-Hafez, F. Alaguz, M. Hamalainen, and M. Latva-Aho. On UWB capacity with respect to different pulse waveforms. In *Proc. 2nd IEEE/IFIP Intl. Conf. Wireless and Optical Communications Networks (WOCN'05)*, pages 107 – 111, 2005.

[8] J. Agbinya and H. D. Truong. UWB signal bandwidth expansion and synthesis using prolate and wavelet functions. In *Proc. 4th Intl. Conf. Mobile Business (ICMB'05)*, pages 686 – 689, 2005.

[9] A. Alavi, C. Tellambura, and I. Fair. PAPR reduction of OFDM signals using partial transmit sequence: an optimal approach using sphere decoding. *IEEE Communications Letters*, 9:982 – 984, Nov 2005.

[10] K. Anwar, A. U. Priantoro, M. Saito, T. Hara, M. Okada, and H. Yamamoto. On the PAPR reduction for wavelet based transmultiplexer. In *Proc. International Symposium on Communications and Information Technologies (ISCW'2004)*, pages 812 – 815, Oct 2004.

[11] J. Armstrong. Peak-to-average power reduction for OFDM by repeated clipping and frequency domain filtering. *Electronics Letters*, 38:246 – 247, Feb 2002.

[12] L. Atzori, D. D. Giusto, and M. Murroni. A new PTS OFDM scheme with low complexity for PAPR reduction. *IEEE Transactions on Broadcasting*, 48:103 – 110, Jun 2002.

[13] L. Atzori, D. D. Giusto, and M. Murroni. Performance analysis of fractal modulation transmission over fast-fading wireless channels. *IEEE Trans. Broadcasting*, 48:103 – 110, 2002.

[14] P. Auscher. Wavelet bases for L2(R) with rational dilation factor. *Wavelets and their applications, Boston Jones and Barlett*, pages 439 – 451, 1992.

[15] R. W. Bauml, R. F. H. Fisher, and J. B. Huber. Reducing the peak-to-average power ratio of multicarrier modulation by selected mapping. *Electronics Letters*, 32:2056 – 2057, 1996.

[16] A. Baussard, F. Nicolier, and F. Trucheter. Rational multiresolution analysis and fast wavelet transform: application to wavelet shrinkage denoising. *Signal Processing 84, ELSEVIER*, pages 1735 – 1747, 2004.

[17] A. Benson, J. Proakis, and M. Stojanovic. Towards robust adaptive acoustic communications. In *Proc. MTS/IEEE OCEANS'00*, volume 2, pages 1243 – 1249, Sep 2000.

[18] C. Bhattacharya and G. Patel. A fast implementation of correlation of long data sequences for coherent receivers. *IEEE Trans. Circuits and Systems II: Analog and Digital Signal Processing*, 49:430 – 433, Jun 2000.

[19] H. Bolcskei, P. Duhamel, and R. Hleiss. Design of pulse shaping OFDM/OQAM systems for high data-rate transmission over wireless channels. In *Proc. IEEE Intl. Conf. Comms. (ICC'09)*, volume 1, pages 559 – 564, Jun 1999.

[20] N. Carson and T.A. Gulliver. PAPR reduction of OFDM using selected mapping, modified RA codes and clipping. In *Proc. IEEE 56th Vehicular Technology Conference (VTC 2002-Fall)*, volume 2, pages 1070 – 1073, 2002.

[21] J. S. Chow, J. C. Tu, and J. M. Cioffi. A discrete multitone transceiver system for HDSL applications. *IEEE J. Sel. Comm.*, 9:895 – 908, Aug 1991.

[22] C. K. Chui. An introduction to wavelets. *Academic Press, New York*, 1992.

[23] L. J. Cimini. Analysis and simulation of a digital mobile channel using orthogonal frequency division multipexing. *IEEE Trans. Communications*, 33:665 – 675, Jul 1985.

[24] L. J. Jr. Cimini and N. R. Sollenberger. PAPR reduction of OFDM signals using partial transmit sequence: an optimal approach using sphere decoding. *IEEE Communications Letters*, 4:86 – 88, Mar 2000.

[25] S. Ciolino, M. Ghavami, and A. H. Aghvami. An ultra-wideband pulse shape modulation system based on wavelet packets. In *Proc. IEE Seminar on Ultra Wideband Communications Technologies and System Design*, pages 99 – 102, Jun 2004.

[26] R. V. Dalal. Orthogonal wavelet division multiplexing (OWDM) for broadband wireless communication. *Master of Engineering Science Thesis, University of South Florida*, Aug 1999.

[27] I. Daubechies. Ten lectures on wavelets. *Capital City Press*, 1992.

[28] S. Deng and M. Lin. OFDM PAPR reduction using clipping with distortion control. In *Proc. IEEE International Conference on Communications*, volume 4, pages 2563 – 2567, May 2005.

[29] M. Deumal, C. Vilella, J.L. Pijoan, and P. Bergada. Partially clipping (PC) method for the peak-to-average power ratio (PAPR) reduction in OFDM. In *Proc. IEEE Intcrnational Symposium on Personal, Indoor and Mobile Radio Communications*, volume 1, pages 464 – 468, Sep 2004.

[30] D. E. Driscoll and S. D. Howard. The detection of radar pulse sequences by means of a continuous wavelet transform. In *Proc. IEEE Acoust., Speech, Signal Processing Conf. (ICASSP'99)*, volume 3, pages 1389 – 1392, Mar 1999.

[31] X. Gao, H. Zhang, and D. Yuan. Bit-interleaved coded modulation for OFDM with different orthogonal bases. In *Proc. Joint Conf. of 10th Asia-Pacific Conf. on Comms. and the 5th Intl. Symp. Multi-Dimensional Mobile Comms. (APCC/MDMC'04)*, volume 2, pages 947 – 949, 2004.

[32] S. A. Ghorashi, B. Allen, M. Ghavami, and A. H. Aghvami. An overview of MB-UWB OFDM. In *Proc. IEE Seminar on Ultra Wideband Communications Technologies and System Design*, pages 107 – 110, 2004.

[33] T. Ginige, N. Rajatheva, and K. M. Ahmed. Dynamic spreading code selection method for PAPR reduction in OFDM-CDMA systems with 4-QAM modulation. *IEEE Communications Letters*, 5:408 – 410, Oct 2001.

[34] I. Guvenc and H. Arslan. On the modulation options for UWB systems. In *Proc. Military Communications Conference (MILCOM'03)*, volume 2, pages 892 – 897, 2005.

[35] R. Haas and J. C. Belfiore. A time-frequency well-localized pulse for multiple carrier transmission. *Wireless Personal Communications*, 5:1 – 18, 1997.

[36] S. Hara and R. Prasad. Multicarrier techniques for 4G mobile communications. *Artech House*, 2003.

[37] N. T. Hieu, S. Kiom, and H. Ryu. PAPR reduction of the low complexity phase weighting method in OFDM communication system. *IEEE Transactions on Consumer Electronics*, 51:776 – 782, Aug 2005.

[38] W. Hu and G. Zheng. Orthogonal Hermite pulses used for UWB M-ary communication. In *Proc. Intl. Conf. Information Technology (ITCC'05)*, volume 1, pages 97 – 101, 2005.

[39] E. Jaffrot. Wavelet based channel model for OFDM systems. In *Proc. 15th IEEE International Symposium on Personal, Indoor and Mobile Radio Communications*, volume 1, pages 704 – 708, 2004.

[40] W. C. Jakes. Microwave mobile communications. *New York: Jone Wiley*, 1974.

[41] T. Jiang and G. Zhu. Complement block coding for reduction in peak-to-average power ratio of OFDM signals. *IEEE Communications Magazine*, 43:S17 – S22, Sep 2005.

[42] M. Johnson, L. Freitag, and M. Stojanovic. Improved doppler tracking and correction for underwater acoustic communications. In *Proc. IEEE Acoust., Speech, Signal Processing Conf. (ICASSP'97)*, volume 1, pages 575 – 578, 1997.

[43] A. E. Jones, T. A. Wilkinson, and S. K. Barton. Block coding scheme for reduction of peak to mean envelope power ratio of multicarrier transmission schemes. *Electronics Letters*, 30:2098 – 2099, 1994.

[44] W. W. Jones. Multi-scale wavelet modulation. In *Proc. the 26th Southeastern Symposium on System Theory*, pages 576 – 580, 1994.

[45] Y. Kim, B. Jang, C. Shin, and B. F. Womark. Orthogonal pulses for high data rate communications in indoor UWB systems. *IEEE Comms. Letts.*, 9(5):405 – 407, 2005.

[46] N. Kingsbury. Complex wavelets for shift invariant analysis and filtering of signals. *J. Appl. Comp. Harm. Anal.*, 10(3):234 – 253, 2001.

[47] J. Kovacevic and M. Vetterli. Perfect reconstruction filter banks with rational sampling factors. *IEEE Trans. Sig. Proc.*, 41(6):2047 – 2066, Jun 1993.

[48] W. Lawton. Applications of complex valued wavelet transforms to subband decomposition. *IEEE Trans. Sig. Proc.*, 41:3566 – 3568, 1993.

[49] W. Li, R. Wang, Y. Zhao, and W. Wu. Bi-orthogonal wavelet packet based multicarrier modulation. In *Proc. International Conferences on Info-tech and Info-net (ICII'2001)*, volume 2, pages 464 – 467, 2001.

[50] D. Lim, S. Heo, J. No, and H. Chung. A new PTS OFDM scheme with low complexity for PAPR reduction. *IEEE Transactions on Broadcasting*, 52:77 – 82, Mar 2006.

[51] A. R. Lindsey. Wavelet packet modulation for orthogonally multiplexed communication. *IEEE Trans. Sig. Proc.*, 45:1336 – 1339, May 1997.

[52] H. Liu, T. Zhang, Z. Chen, and F. Liu. Channel estimation for OFDM systems based on wavelets network interpolation algorithm. In *Proc. 3rd international conference on Machine Learning and Cybernetics*, pages 3120 – 3123, Aug 2004.

[53] J. Liu, J. McNew, and R. Trerotola. Wireless LAN extensions for vehicular environments and the control channel capacity. In *Proc. IEEE 60th Vehicular Technology Conference (VTC2004-Fall)*, pages 3210 – 3213, 2004.

[54] M. Luise, M. Marselli, and R. Reggiannini. Low-complexity blind carrier frequency recovery for OFDM signals over frequency-selective radio channels. *IEEE Trans. Communications*, 50:1182 – 1188, Jul 2002.

[55] S. G. Mallat. Multiresolution approximation and wavelets. *Trans. Amer. Math. Soc.*, pages 315:69 – 88, 1989.

[56] M. Matsuo, M. Kammada, and H. Habuchi. Design of UWB pulses based on B-splines. In *Proc. Intl. Symp. Circuits and Systems (ISCAS'05)*, pages 5425 – 5428, 2005.

[57] C. Mishra, A. Valdes-Garcia, F. Bahmani, A. Batra, E. Sanchez-Sinencio, and J. Silva-Martinez. Frequency planning and synthesizer architectures for multiband OFDM UWB radios. *IEEE Transactions on Microwave Theory and Techniques*, 53:3744 – 3756, 2005.

[58] S. H. Muller and J. B. Huber. OFDM with reduced peak-to-average power ratio by optimum combination of partial transmit sequences. *Electronics Letters*, 33:368 – 369, 1997.

[59] C. Muschallik. Improving an OFDM reception using an adaptive Nyquist windowing. *IEEE Trans. Consumer Electronics*, 42:259 – 269, Aug 1996.

[60] B. G. Negash and H. Nikookar. Wavelet based OFDM for wireless channels. In *Proc. IEEE Vehicular Technology Conference (VTC'01)*, pages 688 – 691, 2001.

[61] T. Pongpisut, M. Chamchoy, and S. Promwong. A simple method of synthesis design for generating UWB pulse based on wavelet. In *Proc. Intl. Symp. Communications and Information Technology (ISCIT'2005)*, pages 1076 – 1079, 2005.

[62] J. G. Proakis. Digital communications. *McGraw-Hill, 5th edition*, 2001.

[63] J. G. Proakis, M. Stojanovic, and J. A. Catipovic. Adaptive equalization algorithms for high rate underwater acoustic communications. In *Proc. of the 1994 Symposium on Underwater Vehicle Technol. (AUV'94)*, pages 157 – 164, 1994.

[64] T. S. Rappaport. Wireless communications: principles and practise. *Prentice Hall, 2nd edition*, 2002.

[65] O. Rioul and P. Duhamel. Fast algorithms for discrete and continous wavelet transforms. *IEEE Trans. Information Theory.*

[66] K. Sathananathan and C. Tellambura. Forward error correction codes to reduce intercarrier interference in OFDM. *IEEE Trans. Communications*, 4:566 – 569, May 2001.

[67] I. W. Selesnick. Hilbert transform pairs of wavelet bases. *IEEE Sig. Proc. Letters*, 8(6):170 – 173, Jun 2001.

[68] I. W. Selesnick. The design of approximate hilbert transform pairs of wavelet bases. *IEEE Trans. Signal Processing*, 50(5):1144 – 1152, 2002.

[69] A. Seyedi and G. J. Saulnier. General ICI self-cancellation scheme for OFDM systems. *IEEE Trans. Vehicular Technology*, 54(1):198 – 210, Jan 2005.

[70] B. S. Sharif, J. Neasham, O. R. Hinton, and A. E. Adams. A computationally efficient doppler compensation system for underwater acoustic communications. *IEEE J. Oceanic Eng.*, 25:52 – 61, Jan 2001.

[71] W. P. Siriwongpairat, W. Su, M. Olfat, and K. J. R. Liu. Multiband-OFDM MIMO coding framework for UWB communication systems. *IEEE Transactions on Signal Processing*, 54:214 – 224, Jan 2006.

[72] C. Snow, L. Lampe, and R. Schober. Performance analysis of multiband OFDM for UWB communication. In *Proc. IEEE International Conference on Communications (ICC'2005)*, volume 1, pages 426 – 431, Mar 2005.

[73] S. Srinidhi, J. G. Proakis, and M. Stojanovic. Wavelet based modulation for frequency hopped spread spectrum communications. In *Proc. 49th IEEE Vehicular Technology Conference (VTC'99)*, volume 2, pages 904 – 908, 1999.

[74] J. Sumethnapis and K. Araki. High performance transmission using differential multi-pulse modulation in transmit-reference ultra-wideband (TR-UWB) communications. In *Proc. Fourth Annual Wireless Telecommunication Symposium (WTS'05)*, pages 141 – 144, 2005.

[75] D. B. H. Tay and M. Palaniswami. Design of approximate Hilbert transform pair of wavelts with exact symmetry. In *Proc. IEEE Acoust., Speech, Signal Processing Conf. (ICASSP'04)*, volume 2, pages 921 – 924, 2004.

[76] A. Teolis. *Computational signal processing with wavelets.* Birkhauser, 1998.

[77] U. Tureli, D. Kivanc, and Hui Liu. Experimental and analytical studies on a high-resolution OFDM carrier frequency offset estimator. *IEEE Trans. Vehicular Technology*, 50:629 – 643, Mar 2001.

[78] A. Vahlin and N. Holte. Optimal finite duration pulses for OFDM. *IEEE Trans. Sig. Proc.*, 44(1):10 – 14, Jan 1996.

[79] P. P. Vaidyanathan. Multirate systems and filter banks. *Prentice Hall*, 1993.

[80] M. Vetterli and T.A. Tony Verma. Filterbank implementation of Meyer's wavelet. *http://www.stanford.edu/~dattorro/Wavelet.pdf*, Aug 2006.

[81] S. Weinstein and P. Ebert. Data transmission by frequency-division multiplexing using the discrete fourier transform. *IEEE Trans. Communications*, 19:628 – 634, Oct 1971.

[82] M. Z. Win and R. A. Scholtz. Impulse radio: how it works. *IEEE Communications Letters*, 2:36 – 38, Feb 1998.

[83] M. Z. Win and R. A. Scholtz. Ultra-wide bandwidth time-hopping spread-spectrum impulse radio for wireless multiple-access communications. *IEEE Trans. Communications*, 48:679 – 689, Apr 2000.

[84] G. W. Wornell and A. V. Oppenheim. Wavelet-based representations for a class of self-similar signals with application to fractal modulation. *Information Theory, IEEE Transactions on*, 38:785 – 800, 1992.

[85] D. Wulich. Reduction of peak to mean ratio of multicarrier modulation using cyclic coding. *Electronics Letters*, 32:432, 1996.

[86] W. Yang, G. Bi, and T.-S.P. Yum. A multirate wireless transmission system using wavelet packet modulation. In *Proc. IEEE 47th Vehicular Technology Conference*, volume 1, pages 368 – 372, 1997.

[87] S. Yoo, S. Yoon, S. Y. Kim, and I. Song. A novel PAPR reduction scheme for OFDM systems: selective mapping of partial tones (SMOPT). *IEEE Transactions on Consumer Electronics*, 52:40 – 43, Feb 2006.

[88] M. You and J. Ilow. A multi-wavelet packet modulation in wireless communications. In *Proc. Canadian Conf.Electrical and Computer Engineering (CCECE'2004)*, pages 2367 – 2370, May 2004.

[89] L. Yu and L. B. White. Rational orthogonal wavelet-based broadband communications in practical multipath/Doppler channels. *Journal paper in preparation.*

[90] L. Yu and L. B. White. Broadband doppler compensation for rational wavelet-based UWA communication systems. In *Proc. Asia-Pacific Conferences on Communications (APCC'05)*, pages 605 – 609, 2005.

[91] L. Yu and L. B. White. A new complex wavelet and its application in communications. In *Proc. 4th Workshop on the Internet, Telecommunications and Signal Processing (*WITSP *'2005)*, pages 343 – 348, 2005.

[92] L. Yu and L. B. White. Complex rational orthogonal wavelet and its application in communications. *IEEE Sig. Proc. Letters*, 13(8):477 – 480, Aug 2006.

[93] Y. V. Zakharov and V. P. Kodanev. Multipath-doppler diversity of OFDM signals in an underwater acoustic channel. In *Proc. IEEE Acoust., Speech, Signal Processing Conf. (ICASSP'00)*, volume 5, pages 2941 – 2944, Jun 2000.

[94] H. Zhang and T. A. Gulliver. Biorthogonal pulse position modulation for time-hopping multiple access UWB communications. *IEEE Trans. SP.*, 4(3):1154 – 1162, 2005.

[95] H. Zhang, W. Li, and T. A. Gulliver. Pulse position amplitude modulation for time-hopping multiple-access UWB communications. *IEEE Trans. Comms.*, 53(8):1269 – 1273, 2005.

[96] L. Zhang and Z. Zhou. A novel synthesis design and implementation for generating UWB narrow pulse based on wavelet. In *Proc. International Symposium on Communications and Information Technologies (ISCIT'2004)*, pages 1228 – 1231, 2004.

[97] X. Zhang and G. Bi. OFDM scheme based on complex orthogonal wavelet packet. In *Proc. 12th IEEE Intl. Symp. on Personal, Indoor and Mobile Radio Comms.*, volume 2, pages E–99 – E–104, Sep 2001.

[98] Z. Zhang, W. Jiang, H. Zhou, Y. Liu, and J. Gao. High accuracy frequency offset correction with adjustable acquisition range in OFDM systems. *IEEE Trans. Wireless Communications*, 4:228 – 237, Jan 2005.

[99] Y. Zhao, J. D. Leclercq, and S. G. Haggman. Intercarrier interference compression in OFDM communication systems by using correlative coding. *IEEE Communications Letters*, 2:214 – 216, Aug 1998.

[100] Y. Zhao, J. D. Leclercq, and S. G. Haggman. Intercarrier interference self-cancellation scheme for OFDM mobile communication systems. *IEEE Trans. Communications*, 49:1185 – 1191, Aug 2001.